Electrical Characteristics of Erbium-Doped Silicon Diodes for Radiation Detectors

by

Solomon Emmanuel Omogiate

A dissertation submitted in accordance with the requirements of the degree of
Master of Science in Physics at the University of South Africa.

Supervisor   : Prof. S.J. Moloi (University of South Africa)

March, 2020

Declaration

I declare that "Electrical Characteristics of Erbium-Doped Silicon Diodes for Radiation Detectors" is my own work and that all sources that I have used or quoted have been indicated and acknowledged by means of references.

I further declare that none of this material has been submitted for any other degree at University of South Africa (Unisa) for another qualification or at any other higher education institution.

Mr. S.E. Omogiate:

Date:

Abstract

Crystalline silicon was doped with erbium by ion implantation method at room temperature. The implanted silicon was annealed for 30 minutes at 800℃ and 1000℃. Rutherford Backscattering Spectrometry/channelling technique was used to establish the presence of erbium and to investigate the diffusion mechanisms of ion in silicon. A change in silicon crystal structure due to implantation and as a function of annealing temperature was investigated by *XRD* technique. In addition, Schottky diodes were successfully fabricated on unimplanted and erbium-doped silicon. The fabricated diodes were characterized using current-voltage and capacitance-voltage techniques to investigate a change in electrical properties of the diodes due to erbium doping. Effects of erbium doping on electronic parameters were discussed in this work. In general, the results indicate that in silicon erbium is responsible for relaxation behaviour of the material. A material exhibiting relaxation behaviour is resistant to radiation-damage. Thus, erbium is a promising dopant to improve radiation-hardness of silicon to be used for fabrication of radiation detectors to meet the current and future requirements for high energy physics experiments.

Keywords: Semiconductors; Silicon; Erbium doping, Schottky diodes; Current; Capacitance; Radiation detectors; Radiation damage; relaxation material; Radiation-hardness

Acknowledgements

Dedication

I dedicate this work to God almighty

Table of Contents

Chapter 1

Introduction and literature review

1.1 Introduction

Silicon detectors are used in variety of applications such as in high-energy physics experiments to detect charge, in medical imaging to diagnose abnormalities and as solar cells to convert incident light into electrical energy [1-3], to mention the few. These detectors have ability for such applications because of their conductivity that changes as a function of impurities introduced in silicon or operational temperature or incident light intensity in silicon. In addition, silicon is an abundant material and its properties are easily understood for the fabrication of the detectors [4-5].

In this work, crystalline silicon with different types of doping concentration was acquired from the industry and implanted with erbium to fluences of 10^{15} and 10^{16} ion/cm². X-ray diffraction (*XRD*) and Rutherford backscattering spectrometry (*RBS*) material characterization techniques were carried out on the implanted silicon to establish the presence and diffusion mechanisms of erbium in silicon. Schottky diode were fabricated on unimplanted and implanted silicon and characterized with current-voltage and capacitance-voltage techniques to investigate a change in electrical properties of the diodes due to erbium implantation.

1.2 Literature review

Silicon detectors are damaged by the same radiation they intend to detect [1-2]. It has been predicted that high energy-physics experiments would need to be carried out at radiation fluence of 10^{16} n/cm², ten times higher than the current operational fluence in the year 2026 [15]. This will impose serious challenges to current detectors since they will be expected to operate efficiently for a period longer than ten years in this environment. It is, therefore,

important that the effects of radiation on the detectors are understood in order to improve their radiation-hardness.

When operating under medium and high radiation environments, the efficiency of the detector decreases leading to an unreliability and instability of the data acquired by the detector [16]. When used in medical imaging, the image that is produced by these detectors become unclear and the exact dosage to be applied for the treatment cannot be determined when used in radiation dosimetry [3]. These are few among many challenges the current detectors are faced with during their operations.

In trying to understand the damage on the detector, it has been found that radiation imparts high energy and momentum to the host atoms and displaces them from their lattice sites to create vacancies and interstitials, defects, in the material [17-18]. Depending on the energy and the type of the particle, the displaced atoms may interact with other atoms to create more defects in the material [19] as they become to rest. As a result, the crystal structure changes as defects are generated in the material. The generated defects result into levels in the energy gap and are responsible for change in electrical properties of the detectors [6-1; 12-13; 20]. The defect levels generated by radiation are also responsible for degradation of charge collection efficiency (*cce*) of the detectors [15; 21].

A change in electrical properties of the detectors due to damage involves an increase in leakage current and in breakdown voltage due to generation of charge carriers by radiation-induced defects [14; 22]. It has also been observed that the current-voltage (*I-V*) trend changes from exponential to ohmic behaviour after radiation-damage [6-9; 12-13]. The region of ohmic behaviour was found to increase with fluence for 1 MeV neutrons [14]. The result of this ohmic behaviour is not fully understood though the damage has been studied for so long. An explanation of ohmic behaviour has been attempted by relaxation theory that

was introduced in the year 1961 [23]. This theory is different from a conventional textbook lifetime theory and it seems unwelcome in the field of semiconductor for radiation detectors.

Radiation also increases a full depletion voltage of the detectors [14]. This means that for the detector to operate optimally will need to be operated at high reverse bias using sophisticated and expensive equipment. This also imposes serious challenge since the current is not stable at high negative voltage [24]. This high negative voltage would result in instability of the data acquired by the detector.

It has also been found that radiation changes the conductivity-type of the material [25]. A change in conductivity means that the material that was initially n-type would be converted to p-type after irradiation. This change could either be due to donor removal or acceptor introduction. A change in conductivity-type has been observed at radiation fluence of 1.4×10^{13} n/cm^2 for 1 MeV on n-type silicon [25]. A change in conductivity type on p-type silicon has not been reported before. It is with this reason that studies on silicon radiation damage is further carried out in order to address this shortfall. With these on-going studies, contention about whether a change in conductivity-type is due to donor removal or acceptor introduction would be reached.

Device parameters such as a low voltage peak and a negative capacitance [26] on capacitance-voltage trends of irradiated silicon detectors have not been fully understood. These two parameters have been a point of contention in the field of semiconductor research for so long were also observed on the diodes fabricated on gold -doped silicon [27]. According to ref. [28] these factors are due to surface defects generated during the fabrication of the detectors contrary to the data by [29] where the factors are being explained in terms of research equipment. Later, the results presented by Jones *et al*. [30] indicated that the factors are due to defects that are generated in the bulk of the material. It is therefore,

3

important that these parameters are understood in order to establish methods suitable to improve radiation-hardness of silicon for detector fabrication.

To improve radiation-hardness of silicon, defects are deliberately introduced in the material [17]. These defects are introduced in a controllable manner either by a heavy pre-irradiation [31-32] of silicon or addition of impurities in silicon [10-14; 17]. For the material to attain its possible radiation-hardness, it needs to be irradiated for a very long time, at least, three months, with particles that cannot easily be accelerated such as neutrons and protons. [34]. After irradiation, the material (samples) needs to be stored in sub-zero temperature in a fridge for radioactive nuclides to decay to a level where it is safe to characterise the samples [34]. As a result, the effects of radiation on the diodes immediately after irradiation could not be investigated. A study immediately after irradiation process is important since properties of the devices have been found to change with time after irradiation [15; 36]. As a result, attaining radiation hardness of the material using pre-irradiation is impossible and not easily available for research in the country.

Introducing impurities in the material is like irradiation and is a suitable and inexpensive option to improve radiation-hardness of silicon. Initially impurities were introduced in silicon in order to improve switching time of electronic devices [10-11]. It was later found that the impurities can also improve properties of the material for fabrication of radiation detectors [13-14; 17; 33]. Depending on their nature and the amount, impurities may exhibit similar behaviour as that of radiation and render the material useless [27]. Thus, the impurities in silicon should be introduced in a controllable manner to improve desired properties while suppressing (or minimizing) the undesired properties.

Gold is one of the metals that have been used to modify properties of silicon for the fabrication of the detector. Gold (Au) in silicon generates three defect levels, two acceptor

levels at $E_c - 0.34$ eV and at $E_c - 0.55$ eV and a donor level at $E_v + 0.34$eV [10], where E_c and E_v are the energy levels at the bottom of the conduction band and the top of the valence band, respectively. Platinum (Pt) is another heavy metal that has also been used to generate impurities in silicon and it has been found to diffuse in silicon in a similar manner as gold [11] and has a similar effects as those of gold generating three defect levels at $E_c - 0.23$ eV, $E_c - 0.55$ eV and $E_c + 0.36$ eV [11].

Both metals, gold and platinum, generate a midgap defect, a defect level close to the centre of the energy gap (~0.56 eV). The midgap defect is known to be responsible for the relaxation behaviour of silicon material [6-9; 12-14]. Detectors fabricated on relaxation material have been found radiation resistant [7; 14]. This implies that silicon should be made relaxation-like before being used for fabrication of the detector. This conclusion was however, reached on the detectors fabricated on silicon that was doped with gold and platinum. These two metals are, however, relatively expensive for research purposes. More data is needed in addition to that of Ref. [32], on the effect of other metals such erbium impurities on electrical properties of silicon detectors. With enough data available a reasonable comparison between expensive metal dopants (gold and platinum) with other silicon dopants would be reached.

1.4 Aim and objectives

The aim of this work is to establish a simple and cheaper method to improve radiation-hardness of silicon detectors to be used in high-energy physics experiments. The improvement can be achieved by deliberate introduction of defects in material in a controllable manner such that the unfavourable properties are minimised while maximising the favourable properties. The set specific objectives are to:

1. dope crystalline silicon with erbium using ion implantation method

2. anneal the implanted silicon at different temperatures

3. establish the presence of erbium and to study the diffusion mechanism of erbium in silicon using *RBS* and *XRD* techniques

4. fabricate Schottky diodes on undoped and erbium-doped silicon

5. characterise the fabricated diodes using current-voltage and capacitance-voltage techniques at room temperature

6. summarize possible processes involved in achieving radiation-hardness of silicon

7. to infer material from the device behaviour.

1.4 Dissertation outline

Chapter 1 presents introduction, motivation, literature review, aim, and objective of this project. Chapter 2 is about theoretical overview covering the basic properties of semiconductor detectors, with reference to silicon detector. In addition, a review of radiation damage mechanism in semiconductors and the effects of radiation damage on silicon detectors performance are summarized in this chapter. Also, the theoretical aspects of metal semiconductor contacts are presented in Chapter 2. Chapter 3 summarises Ion implantation doping method. Chapter 4 provides an overview on the material and device characterisation techniques used in this work. Chapter 5 outlines experimental details that were applied in this work. The instrumentation used is also described in the chapter. Chapter 6 presents experimental characterization techniques results. Chapter 7 outlines general conclusions and suggestions for future work.

References

[1]   Martini M and McMath T A, 1970 *Nucl. Instruments Meth.* **79** 259.

[2]   Van Lint V A T, 1987 *Nucl. Instruments Meth. A* **253** 453.

[3]   Rosenfeld A B, 2006 " *Semiconductor Detectors in Radiation Medicine: Radiotherpy and Related Applications*" , *Proc. on Radiation Detecors Medical Applications Radiation Detectors for Medical Applications, Crimea, Unkraine, September, 2005.*

[4]   Benton J L *et al.,* 1991 *J. Appl. Phys.* **70** 2667.

[5]   Coffa S *et al.,* 1988 *J. Appl. Phys.* **64** 6291.

[6]   Jones B K, Santana J and McPherson M, 1997 *Nucl. Instr. Meth. A* **395** 81.

[7]   McPherson M, Jones B K and Sloan T, 1997 *Semicond. Sci. Technol.* **12** 1187.

[8]   Jones B K, Santana J and McPherson M, 1998 *Solid State Commun.* **105** 547.

[9]   Jones B K and McPherson M, 1999 *Semicond. Sci. Technol.* **14** 667.

[10]   Watanbe and Munakata Watanabe K and Munakata C, 1993 *Semicond. Sci. Technol.* **8** 230.

[11]   Kwon Y K, Ishikawa T and Kuwano H, 1987 *J. Appl. Phys.* **61** 1055.

[12]   McPherson M, 2004 *Radiation Effects and Defects in Solids* **158** 45.

[13]   McPherson M, Sloan T and Jones B K, 1997 *J. Phys. D: Appl. Phys.* **30** 3028.

[14]   Moloi S J and McPherson M, 2009 *Physica B* **404** 3922.

[15]   Kramberger G, 2019 *Nucl. Instr. Meth. A* **924** 192.

[16]   Fretwurst E *et al.,* 2005 *Nucl. Instr. Meth. A* **552** 124.

[17]   Moll M *et al.,* 2005 *Nucl. Instr. Meth. A* **546** 99.

[18]   Bruzzi M, 2016 *Nucl. Instr. Meth. A* **809** 105.

[19]   Watkins G D, 2000 *Material Sci. Semicond. Processing* **3** 227.

[20]   Garutti E and Musienk Y, 2019 *Nucl. Inst. Meth. A.* **926** 69.

[21]   Donegani EM *et al.,* 2018 *Nucl. Instr. Meth. A* **898** 15.

[22]   Yarita K *et al.,* 2019 *Nucl. Instr. Meth. A* **924** 457.

[23]   Van Roosbroeck W, 1961 *Phys. Rev.* **123** 474.

[24]   Gorine G *et al.*, 2018 *IEEE Trans. Nucl. Sci.* **65** 1583.

[25]   Pitzl D *et al.,* 1992 *Nucl. Instr. Meth. A* **311** 98.

[26]   McPherson M, 2002 *Nucl. Instr. Meth. A* **488** 100.

[27]   Msimanga M and McPherson M, 2006 *Materials Sci. and Engineering* **127** 47.

[28]   Wu X, Yang E S and Evans H L, 1990 *J. Appl. Phys.* **68** 2845.

[29]   Werner J H, 1988 *Appl. Phys. A*. **47** 291.

[30]   Jones B K and McPherson M, 1999 *Semicond. Sci. Technol.* **14** 667.

[31]   Litovchenko P G *et al.* 2006 *Nucl. Instr. Meth. A* **568** 78.

[32]   Moloi S J and McPherson M, 2009 *Physica. B*. **404** 2251.

[33]   Dixon R L and Ekstrand K E, 1986 *Radiat. Prot. Dosimetry* **17** 527.

[34]   Strydom W, 2019 - Private communication.

[35]   Li Z *et al.,* 2013 *Nucl. Instr. Meth. A* **699** 1.

[36]   Moloi S.J and McPherson M, 2019 *Nucl. Instr. Meth. B* **440** 64.

Chapter 2

Theoretical overview

This chapter describes basic semiconductor principles, which will enable an understanding of the work presented in the subsequent chapters. Semiconductor concepts such as crystal structure, energy bands, carrier generation and recombination, carrier trapping, metal-semiconductor contacts, Schottky and Ohmic contacts, are discussed in this chapter. The radiation damage mechanisms in a semiconductor and the effects of radiation damage on semiconductor detector performance are also outlined.

2.1 Semiconductors

Semiconductors are the basic building block of modern electronics, including transistors, solar energy conversion and storage, light-emitting diodes (LEDS), and digital and analog integrated circuits [1]. They are preferred materials for these applications mainly because of the variation of their conductivity.

Semiconductors are divided into two distinct groups, namely elemental and compound semiconductors. Elemental semiconductors are composed of single class of elements found in the group IV of the periodic table, and members of this family include silicon (Si) and germanium (Ge). The crystal structure of elemental semiconductors is tetrahedron bonded, that is each atom is surrounded by four nearest atoms. These tetrahedral bonded semiconductors form the mainstay of the electronics industry and the cornerstone of modern technology [2].

Compound semiconductor is an alloy composed from elements of group III and V column of the periodic table and are created as a result of the chemical reaction between two or more different components, such as from Group IV (Si, Ge, Sn), from Group III and V (Al, Ga or

In, with N, As, or Sb), or from Group II and VI (Zn or Cd, with O, S, Se, or Te). Compound semiconductors formed from elements of the groups III and V of the periodic table (such as GaAs) have properties similar to their group IV counterparts. Three (ternary) or four (quaternary) element compound semiconductors, such as InGaN and GaInNAs, can also be formed and are commonly used in electronic and optoelectronic devices because their band gap and other physical properties (optical, structural, and electronic) that can be adjusted by controlling the alloy composition [3]. Figure 2.1 lists some common elemental and binary compound semiconductor materials.

Figure 2. 1: *Illustration of the relationship of the elemental and compound semiconductors.*

The main distinguishable characteristics between conductors, insulators, and semiconductors can be visualized in terms of their energy gaps in figure 2.2. In metals, at low temperature, the Fermi energy lies within the conduction band, leading to a large concentration of free electrons in the conduction band which result in the conductivity of the material to be high [4].

The Fermi energy of insulator is below the conduction band and the electrons are unable to be excited from the valence band to the conduction band due the large gap between them. Therefore, there are no charge carriers generated making insulator non-conductive at room

10

temperature [5]. Whereas in semiconductor, the Fermi energy is smaller than insulators. Electrons can be excited into the higher energy bands with lower energy. At low temperature, no electron possesses sufficient energy to be excited to the conduction band and thus, no generation of charge, which implies that semiconductors are perfect insulators at 0 K [6]. At a temperature higher than 0 K, the electrons are excited from valence band to conduction band. As they get excited, they leave holes in the valence band. As a result the density of charge carriers increases with temperature resulting in the conductivity of the material be a function of temperature [2; 7].
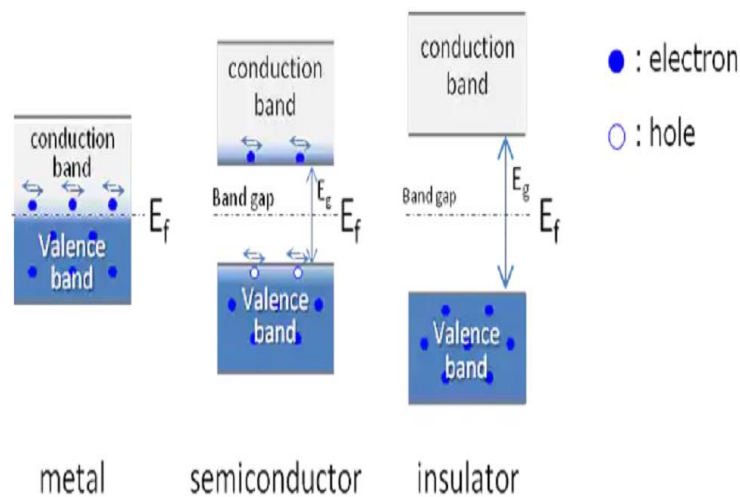
Figure 2. 2: *The key difference between insulator, semiconductor and metal/conductor using the Fermi energies.*

2.1.1 Direct and indirect semiconductors

In a direct semiconductor the minimum energy state of the conduction band is aligned with the maximum energy state of the valence band. As shown in figure 2.3 (a) an electron making a transition from the conduction band to the valence band, can do so without a change in neither wave vector (k) nor momentum ($\hbar k$). This type of semiconductor is called a direct band gap semiconductor and GaAs is one of such examples. Direct gap semiconductors have many unique properties which are advantageous for optical and electronic applications, especially for detectors and emitters of infrared radiation associated with interband optical transitions [6; 8].

11

For indirect energy-gap semiconductors, the conduction band minimum and the valence band maximum energy occur at different momenta. Furthermore, a phonon is required to simultaneously conserve energy and momentum [9]. As shown in figure 2.3 (b), thus, an electron at the minimum of the conduction band does not de-excite directly to the maximum of the valence band. This indirect transition from conduction band to valence band needs a change in energy and momentum. Silicon and germanium are examples of indirect energy gap semiconductors [10].
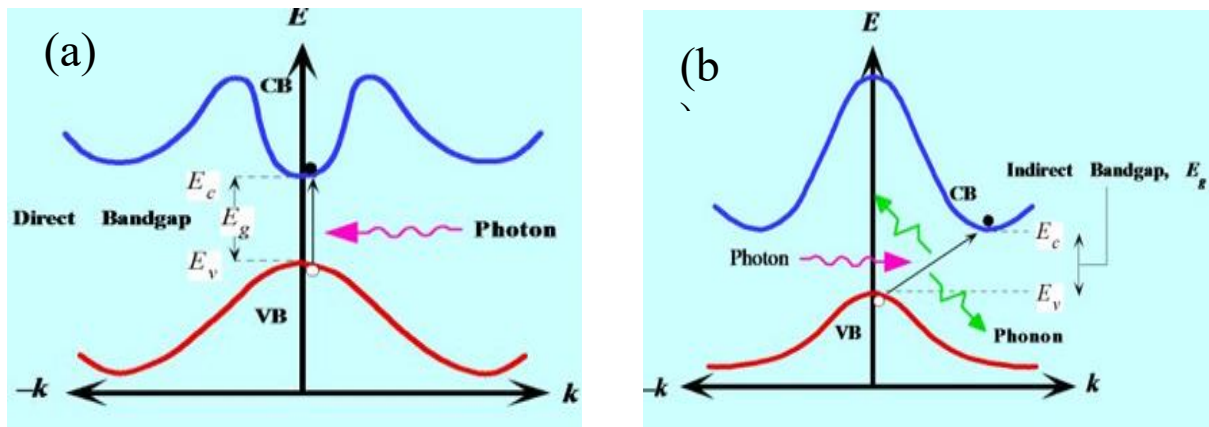
Figure 2. 3: *Electron transition of direct energy gap (a) and indirect energy gap (b) semiconductor.*

2.1.2 Intrinsic semiconductors

In intrinsic or pure semiconductors the density of electrons (n_e) in the conduction band and that of holes (p_h) in the valence band is equal, ($n_e = p_h = n_i$). The Fermi energy for the intrinsic semiconductor lies in the middle of the energy gap [8; 11]. n_i, in this case is an intrinsic carrier concentration. The occupancy probability of one state at the energy and temperature in thermal equilibrium is governed by the Fermi-Dirac statistics [3-4; 6; 9-15] as:

$$f_e(E) = \frac{1}{1 + \exp\left(\frac{E - E_F}{K_b T}\right)} \tag{2.1}$$

where K_b is the Boltzmann constant and T is the system temperature in Kelvin. E_F is the Fermi energy, that is, the energy at which at 0 K all levels with $E < E_F$ are occupied while for $E > E_F$ the value is zero [3; 6; 9]. It can be seen from the equation that at $E = E_F$, $f_e(E)$ = 0.5. In this condition the holes and the electrons concentration will be identical indicating probability of locating electrons in the energy gap is half.

The density of electrons in the conduction band is given [7] as:

$$n_e = N_{cb} \exp\left(-\frac{E_{cb} - E_F}{K_b T}\right) \tag{2.2}$$

where N_{cb} and E_{cb} are the effective density of states in the conduction band and energy of the conduction band edge respectively. N_{cb} is given [3] as:

$$N_{cb} = 2\left(\frac{2\pi m_{cb} K_b T}{h^2}\right)^{\frac{3}{2}} \tag{2.3}$$

where m_{cb} is the effective mass of electrons in the conduction band. Similarly, the density of holes in the valence band is given [3] as:

$$p_h = N_{vb} \, exp\left(-\frac{E_F - E_{vb}}{K_b T}\right) \tag{2.4}$$

where N_{vb} is the effective density of states for holes in the valence band and E_{vb} is the energy of the valence band edge. N_{vb} is given by:

$$N_{vb} = 2\left(\frac{2\pi m_{vb} K_b T}{h^2}\right)^{\frac{3}{2}} \tag{2.5}$$

where m_{vb} is the effective mass of holes in the valence band and h is the Planck constant. In an intrinsic semiconductor, where $n_e = p_h$, it can be shown using equations 2.2 and 2.4 that the position of the Fermi energy in an intrinsic semiconductor is:

$$E_F = \frac{E_{cb} + E_{vb}}{2} + \frac{K_b T}{4} \ln\left(\frac{m_{vb}}{m_{cb}}\right) = E_i \tag{2.6}$$

showing that it is found in the middle of the energy gap. The intrinsic carrier density n_i can also be obtained using equations 2.2 and 2.4 as:

$$n_e p_h = n_i^2 = N_{cb} N_{vb} exp\left(-\frac{E_g}{K_b T}\right) \tag{2.7}$$

with the energy gap $E_g = E_{cb} - E_{vb}$.

2.1.3 Extrinsic semiconductors

The semiconductor in which impurities are added is called extrinsic semiconductor. The process of adding impurities to the semiconductor is called doping. Doping changes the electrical conductivity of semiconductor. In this case, number of free electrons and holes in extrinsic semiconductor are unequal.

The added impurities form the states in the energy gap of semiconductors. An overview of generated states created by impurities in extrinsic semiconductor is shown in figure 2.4. A semiconductor can be doped *n*- or *p*-type.
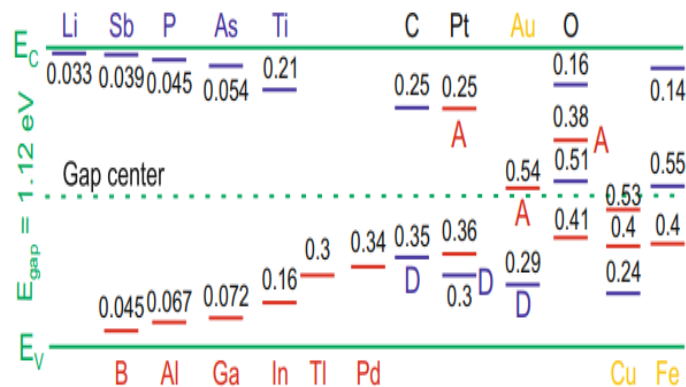
Figure 2. 4: *States in the silicon energy gap created by different dopants. Acceptor states are displayed in red, donor states in blue [1].*

2.1.3.1 *n*-type semiconductor

Pentavalent impurity atoms have 5 valence electrons. The various examples of pentavalent impurity atoms in silicon include Phosphorus (P), Arsenic (As), Antimony (Sb). When pentavalent impurity is added to an intrinsic or pure semiconductor (silicon or germanium) an *n*-type semiconductor is formed. Pentavalent impurity is called donor impurity because it gives electrons to the host lattice. At room temperature, the number of electrons in the

14

conduction band is in excess of the number of holes in the valence band. Figure 2.5 shows that the Fermi energy in the *n*-type semiconductor lies close to the conduction band [7].
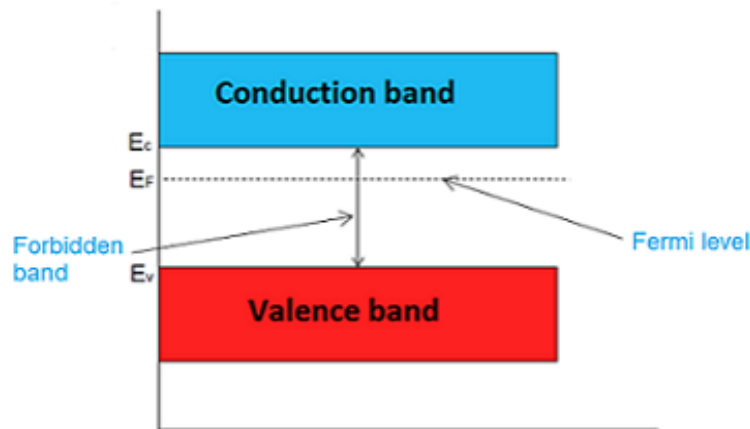
Figure 2. 5: *The energy gap of n-type semiconductor with Fermi energy between intrinsic position and conduction band.*

For a very high temperatures that exceed the ionization temperatures of the added impurities, all donors and acceptors are almost ionized, and the neutrality condition can be approximated [6] as:

$$n_e + N_{ca} = p_h + N_{cd} \tag{2.8}$$

where N_{ca} and N_{cd} are the concentration of acceptors and donors assumed to be ionized. With equations 2.7 and 2.8 combined, the concentration of electrons and holes in *n*-type semiconductor where $N_{cd} \gg N_{ca}$ can be written as:

$$n_e = \frac{N_{cd} - N_{ca}}{2} + \left[\left(\frac{N_{cd} - N_{ca}}{2} \right)^2 + n_i^2 \right]^{\frac{1}{2}} \tag{2.9}$$

Similarly, if the concentration of donors is much larger than the concentration of acceptors ($N_{cd} \gg N_{ca}$), the concentration of free electrons is almost equal to the concentration of donors. The concentration of holes is then given by:

$$p_h = \frac{N_{ca} - N_{cd}}{2} + \left[\left(\frac{N_{ca} - N_{cd}}{2} \right)^2 + n_i^2 \right]^{\frac{1}{2}} \tag{2.10}$$

15

The position of the Fermi energy in an n-type semiconductor can be represented [9] as:

$$E_F = E_{cb} - K_b T \ln \frac{N_{cb}}{N_{cd}}$$

(2.11)

2.1.3.2 *p*-type semiconductor

A *p*-type semiconductor is created by adding trivalent impurity atoms with 3 valence electrons like Boron (B), Indium (In), Gallium (Ga) or Aluminium (Al) to an intrinsic or pure semiconductor. Trivalent impurity creates deficiencies of valence electrons, called "holes" from the host lattice. A hole has a positive electric charge, opposite to the electron charge [7]. At room temperature holes are the majority carriers and electrons are the minority carriers in *p*-type semiconductor. The Fermi level in *p*-type semiconductor lies close to the valence band as shown in figure 2.6 [6].
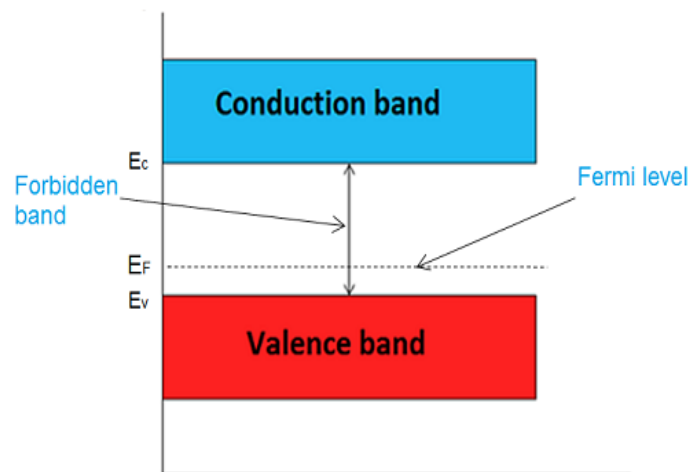
Figure 2.6: *The energy gap of p-type semiconductor with Fermi energy between intrinsic position and valence band.*

The carrier concentration in a *p*-type semiconductor is given by:

$$p_h \approx N_{ca}$$

(2.12)

If the concentration of acceptor is much larger than the concentration of donor ($N_{ca} \gg N_{cd}$), the carrier concentration is then given by:

$$n_e = \frac{n_i^2}{p_h} \approx \frac{n_i^2}{N_{ca}}$$

(2.13)

Then, the position of the Fermi level in a *p*-type semiconductor is written as:

$$E_F = E_{vb} + K_b T \ln \frac{N_{vb}}{N_{ca}}$$ (2.14)

2.2 Silicon

Silicon is an elemental semiconductor with a crystal structure based in two interpenetrating face-centered cubic (fcc) lattices belonging to column IV of the periodic table. This crystal structure form four covalent bonds with neighbouring atoms in order to complete their outer shell. Each atom is therefore, in the centre of a tetrahedron, the corners of which are occupied by other similar atoms [10]. The length of each cube side is called the "lattice parameter" which is equal to 5.43Å in silicon. Figure 2.7 shows the diamond structure of silicon in face centered cubic (fcc) orientation.
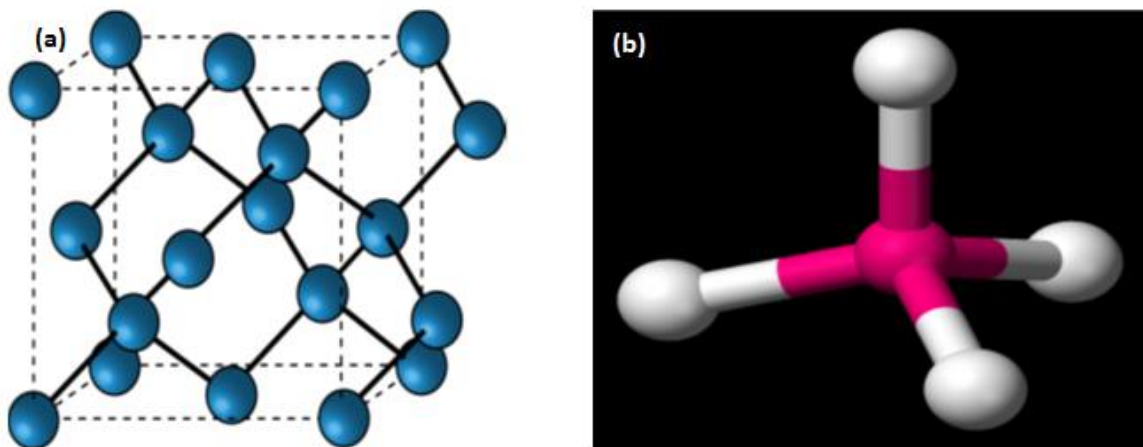
Figure 2.7: D*iamond structure of silicon in face centred cubic (fcc) orientation (a) and (b) tetrahedral structure of silicon atoms with four neighbours sharing covalent bond* [10].

Silicon is a material of choice because the energy gap (1.12 eV at room temperature) is small enough to produce a large number of charge carriers per unit energy loss of the ionizing particles to be detected and the average energy to promote an electron from the valence band to the conduction band in silicon is 3.6 eV [6]. Silicon has some limitations when compared with compound semiconductors. The basic limitation of silicon is that it is an indirect band gap semiconductor. This results in poor light emitters and low light absorption coefficients

[4] making it unsuitable for many optoelectronic applications. Silicon also has a relatively low carrier mobility [10-11] making it unfit for certain high-speed electronic applications.

2.3 Radiation damage in silicon

The study of radiation hardness engages in finding and improving the detector resistance to radiation damage and malfunctions caused by radiation. When radiation strikes semiconductor lead to defects in the material. Two types of damages are bulk and surface damages. The former describes damages to the silicon bulk and is mainly caused by displacements of silicon atoms by energetic particles [16]. The latter is used for radiation-induced damages in the silicon dioxide layer at the $Si\text{-}SiO_2$ interface. Surface damage is primarily caused by ionizing radiation.

2.3.1 Bulk damage

Bulk damage is caused by displacement of a Si atom from its substitution site to an interstitial site to form a Frankel pair. At room temperature, Frenkel pairs have excessive mobility in the bulk. Depending on the energy and the type of the incident particle, the displaced atoms may interact with other atoms to create more defects in the material [17]. As a result, the crystal structure will be changed with defects generated in the material. The generated defects result into levels in the energy gap that are responsible for change in electrical properties of the detectors fabricated on the material [18-19]. In the case of neutron radiation, due to the high Si recoil energy (133 keV), the bulk damage forms electron-hole pairs with a vacancy or create defects with other interstitial atoms or impurities in the silicon bulk [20].

A quantity that describes the rate of energy loss due to atomic displacements as a particle navigates a material is non-ionising energy loss (NIEL) [21-22]. NIEL damage can also be caused by neutral particles like neutrons. The minimum energy required in silicon for having a primary knock on atom (PKA) is 25 keV [23]. Displacement damage is proportional to

non-ionizing energy loss, which is not proportional to the total energy absorbed, but depends on the particle type and energy. An incident particle or photon capable of imparting an energy of about 20 eV to a silicon atom can dislodge it from its lattice site [23].

Displacement damage creates defects clusters. For example, a 1Mev neutron transfers about 60 to 70 keV to the Si recoil atom, which in turn displaces roughly 1000 additional atoms in a region of about 0.1 μm size [24]. X-rays do not cause direct displacement damage, since momentum conservation sets threshold energy of 250 keV for photons. [60]Co gamma-rays cause displacement damage primarily through Compton electrons and are three orders of magnitude less damaging per photon than 1Mev neutron [25]. Table 2.1 gives a rough comparison of displacement damage for protons and electrons.

Table 2. 1: *Relative displacement damage for various particles and energies* [22].

Particle	proton	proton	neutron	electron	electron
Energy	1 GeV	50 MeV	1 MeV	1 MeV	1 GeV
Relative Damage	1	2	2	0.01	0.1

The creation of displacement damage is a result of a PKA, with a specific recoil energy E_{Re}, independent of particle type and interaction process of the imparting particle [24]. The maximum energy imparted to the recoiled silicon atom E_{max} for high energy particles can be determined [23] as:

$$E_{max} = 2 \frac{E_k + 2m_p C^2}{MC^2} E_k \tag{2.15}$$

where E_k is the kinetic energy of the impinging particle, m_p is the rest mass, *M* is the mass of the silicon atom, and *C* is Coulomb interaction. The NIEL can be expressed by the displacement damage cross section or damage function [24] as:

$$D_e(E) := \sum_v \sigma_v(E) \int_{E_d}^{E_{Re}^{max}} F_v(E, E_{Re}) P(E_{Re}) dE_{Re} \tag{2.16}$$

19

where $D_e(E)$ is the displacement damage cross section, σ_v describes the cross section of a possible reaction v. $F_v(E, E_R)$ is the probability for the generation of a PKA due to the reaction v. $F_v(E, E_{Re})$ depends on the recoil energy E_{Re} of a particle with energy E, $P(E_{Re})$ is the Lindhard partition function. Integration limits are the threshold energy for displacements E_d (25 eV for Si) and the maximal recoil energy E_{Re}^{max} [26].

According to the NIEL-hypotheses the damage of any kind of particle with the energy spectrum of $\Phi(E)$ can be related to the damage of 1 MeV neutrons by the hardness factor [27-29] as:

$$k = \frac{\int D_e(E)\Phi(E)dE}{D_e(E = 1MeV)\int \Phi(E)dE} \qquad (2.17)$$

With this factor, it is possible to compare the damage efficiency of different radiation types to that of 1 MeV neutrons. The 1MeV neutron equivalent fluence is given [29] by:

$$\Phi_{eq} = k.\Phi = k \int \Phi(E)dE \qquad (2.18)$$

which can be either measured in 1MeV neutron equivalent particles/cm^2. It should be noted that the NIEL-hypothesis is not valid for all types of particles and energies. Figure 2.8 illustrates the damage created by different types of particles normalized by NIEL to 1MeV neutrons.
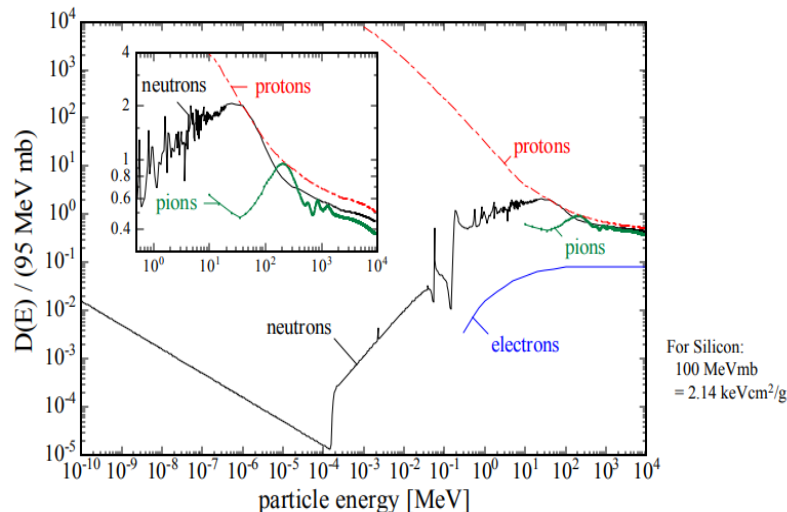
Figure 2. 8: *Displacement damage function D (E) normalized to 95 MeV for neutrons* [29].

20

2.3.2 Surface damage

Surface damage is primarily introduced by ionization of the isolating silicon dioxide (SiO_2) layer by traversing particles due to electron-hole pairs created in the insulating layers SiO_2. The electrons are fast collected in the electrode whereas the holes stay as a positive charge in the oxide because of their lower mobility [30]. This positive charge will induce an accumulation of electrons on the primary silicon bulk which will deteriorate many parameters of the detectors [27].

Figure 2.9 shows the dose dependence of fixed oxide charge concentration for different material, for example, the electrons will create a conductive layer between different readout electrodes, reducing their inter-electrode resistance. Moreover, generating locally high field, breakdown effects will be possible with the generation of avalanches, which will in turn increase the noise. Surface damage cannot be avoided, though some techniques exist to limit its effect [1]. Carriers in the oxide layers however cannot necessarily escape the region and can cause radiation damage in the oxide and in the interface between isolator and silicon bulk [24].
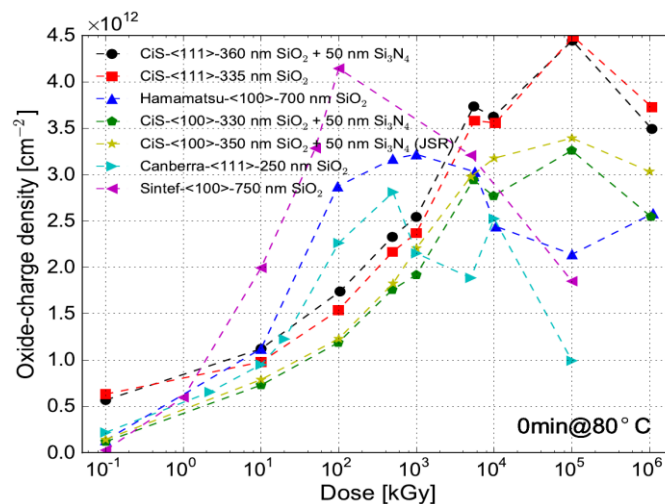
Figure 2. 9: *Dose dependence of the fixed oxide charge concentration for several materials* [30].

2.3.2.1 Effects of radiation damage

The bulk and surface defects create additional levels in the silicon band gap. These levels have three main effects on the performance of silicon detectors. Defects increase the leakage current, change the space charge distribution, influencing the depletion voltage of a sensor, and they can trap charges, which in turn reduces the charge collection efficiency [21-22; 24]. An overview of the effects of radiation damage is given in figure 2.10. The impact of an individual defect depends on the level it creates in the energy gap. Levels towards the centre of the band gap tend to generate leakage current [31]. Acceptor and donor states towards either conduction or valence band can be ionised easily [28; 30]. This generates space charge and has an effect on the effective doping concentration.
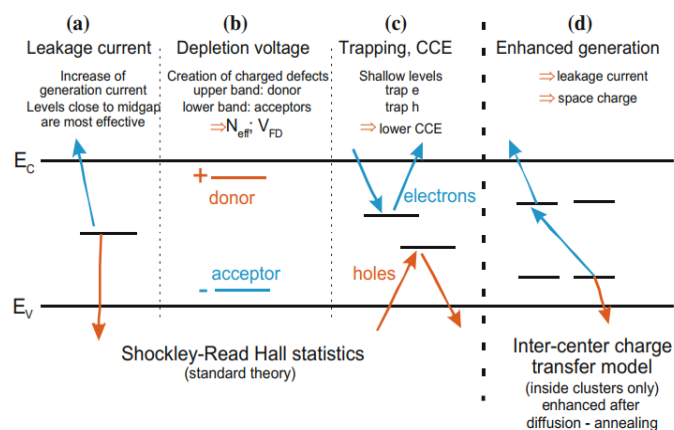
Figure 2. 10: *Locations of different defect level in the silicon band gap and their effects* [32].

A high leakage current is induced by deep level defects that act as generation and recombination centers [31]. These defects are located toward the centre of the intrinsic Fermi energy. It has been established that the leakage current increases linearly with radiation fluence [24; 27; 32] as:

$$\frac{\Delta I}{\text{Volume}} = \alpha \cdot \Phi_{eq} \tag{2.19}$$

where ΔI is the increase in leakage current measured after irradiation of a sensor with the equivalent fluence Φ_{eq}, compared with the current prior to irradiation. As can be seen in

figure 2.11, the increase in current is proportional to the equivalent fluence, resulting in a linear relationship with the slope being the damage constant, α.
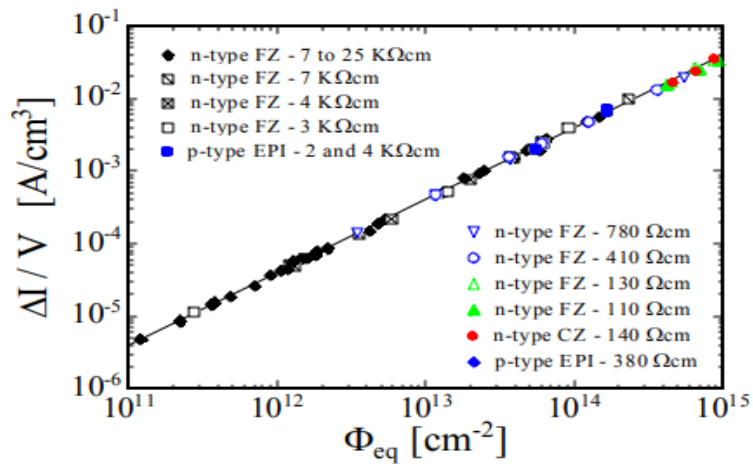
Figure 2. 11: *Scaling of current with fluence.*

A change in space charge is caused by defects located towards the centre of the band gap. As indicated earlier, the space charge in a sensor defines the effective doping concentration and thus the depletion voltage of the device. The depletion voltage (V_{depl}) is proportional to the absolute value of N_{eff} [17; 33] as:

$$V_{depl} = \left(\frac{e}{2\varepsilon\varepsilon_0}\right) |N_{eff}| S_t^2 \tag{2.20}$$

where e the elementary charge, ε_0 is the permittivity of silicon, N_{eff} is effective doping concentration, and S_t is the sensor thickness. Prior to irradiation, the effective doping concentration N_{eff} is given by the different number of donors and acceptors in the silicon bulk [24; 34] as:

$$N_{eff} = N_D - N_A \tag{2.21}$$

Defects created by irradiation resulting in donor states increase the effective doping concentration (N_{eff}) and thus the depletion voltage. Acceptor states on the other hand decrease the effective doping concentration.
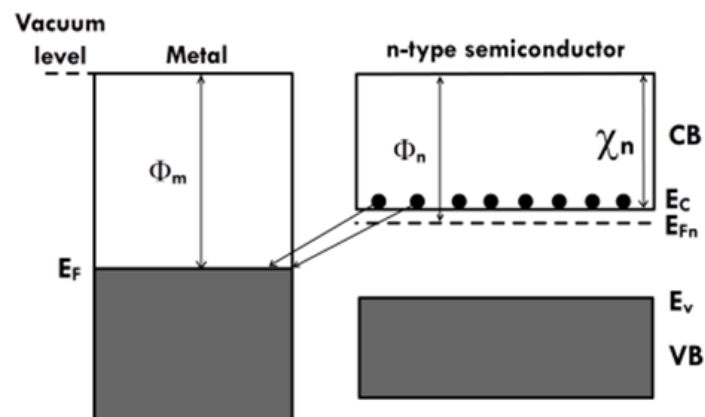
2.4 Metal-semiconductor contacts

Metal semiconductor contacts are categorised based on their rectifying properties into Schottky contacts (rectifying) and Ohmic contacts (non-rectifying properties). Contacts are very important in the field of semiconductor physics as they allow for the fabrication of semiconductor devices and electrical characterization of most semiconductors.

2.4.1 Schottky contact

The rectifying properties of a metal-semiconductor result from the presence of an electrostatic barrier between the metal and the semiconductor. This barrier is as a result of the difference in work functions of the two materials. The work function of the metal is a constant while the semiconductor work function depends on the dopant concentration since it affects the Fermi level position. The work function is not a feature of a bulk material but rather a property of the surface of the material [6]. The work function ,W_{F}, for a given metal surface is defined in terms of Fermi energy (E_F) of the material [6] as:

$$W_{\mathrm{F}} = -e\Phi - E_{\mathrm{F}} \tag{2.22}$$

where Φ is the electrostatic potential in the vacuum nearby the surface. The term $-e\Phi$ is the energy of an electron at rest in the vacuum nearby the surface.


Figure 2. 12: *Schottky junction between metal and n-type semiconductor before contact. The work function of the semiconductor is smaller than that of the metal so that electrons can move from semiconductor to metal, forming a contact potential.*

For *n*-type semiconductor shown in figure 2.12, where the work function of the metal Φ_m surpasses that of the semiconductor Φ_s, thus, electrons flow from the semiconductor into the metal to balance the Fermi levels, leaving behind a depletion region in the semiconductor in which the bands are bent upward leading to rectifying properties [35].

The potential barrier seen by electrons in the metal trying to move into the semiconductor is known as the Schottky barrier height and denoted by Φ_B in figure 2.13 [8]. Schottky barrier height can be defined as the difference between the metal work function and the electron affinity of the semiconductor [35-37] as:

$$\Phi_B = (\Phi_m - \Phi_s) + (E_{cb} - E_F) = \Phi_m - \chi_s \tag{2.23}$$

where Φ_m and Φ_s are the work function for metal and semiconductor, respectively, E_{cb} is the energy of the conduction band, and χ_s is the electron affinity of the semiconductor, i.e. the difference in energy between the vacuum level and the bottom of the conduction band.
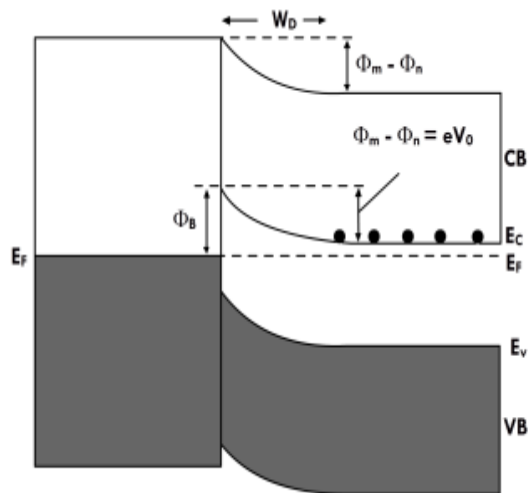
Figure 2. 13: *Schottky junction showing the band bending on the semiconductor side. Semiconductor bands bend up going from the semiconductor (positive) to metal (negative) since this is the same direction as the electric field* [6].

The Fermi energy (E_F) is independent of the metal used and hence the barrier height is independent of the change in external applied voltage but dependent on the interface properties of the metal and semiconductor [37]. The Schottky junction can be biased by

application of an external potential. The current flow depends on the type of bias and the amount of applied external potential [38].

2.4.1.1 Forward bias

In a forward biased Schottky junction, the external potential is applied in a way that it resists the in-built potential. Since the region with the highest resistivity region near the junction is the depletion region, the voltage drop is across the depletion region. Under external bias the Fermi energy no longer align but are shifted with regard to one another and the magnitude of the shift depends on the applied voltage. Energy band diagram of the Schottky junction under forward bias is shown in figure 2.14. In this case, electrons infused from the external circuit into the n-type semiconductor have a lower barrier to overcome before reaching the metal. This leads to a current in the circuit to increase with an increase in external potential [6]. The current in a Schottky diode under forward bias is given [3] as:

$$I = I_0 \left[\exp\left(\frac{e(V_0 - IR_s)}{K_b T} \right) - 1 \right] \tag{2.24}$$

where I_0 is the saturation current. The saturation current (I_0) is normally calculated from the Y-intercept of the linear region of a forward ln (I) versus V_0 plot and it depends on the Schottky barrier (Φ_B) for the system and expresses [39] as:

$$I_0 = A_r A^* T^2 \exp\left(-\frac{e\Phi_B}{K_b T} \right) \tag{2.25}$$

where A_r is the effective area of the diode, A^* is the Richardson constant for thermionic emission and is a material property. Equation 2.24 shows that current in forward bias increases exponentially with applied potential, V.
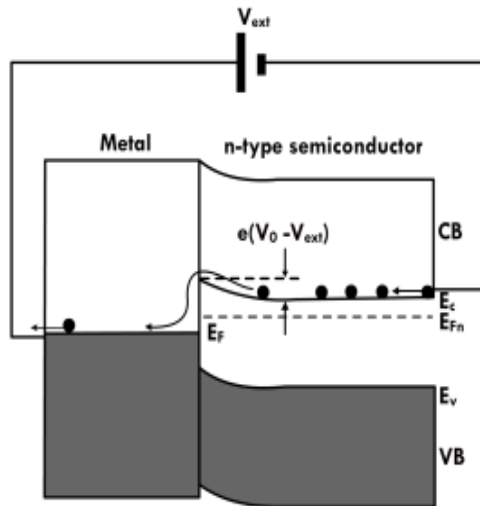
Figure 2. 14: *Schottky junction under forward bias. Adapted from Principles of Electronic Materials [8].*

2.4.1.2 Reverse bias

In reverse bias the external potential is applied in the same direction as the junction potential, as shown in figure 2.15. If a positive voltage is applied to the semiconductor with respect to the metal, the Fermi level is lowered in energy comparative to that of the metal. The depletion width (W_D) is then increased. Electrons overcome a larger potential barrier on the semiconductor side. In this situation, a small reverse current of electrons flowing from the metal to the semiconductor is observed. This condition is known as reversed bias.
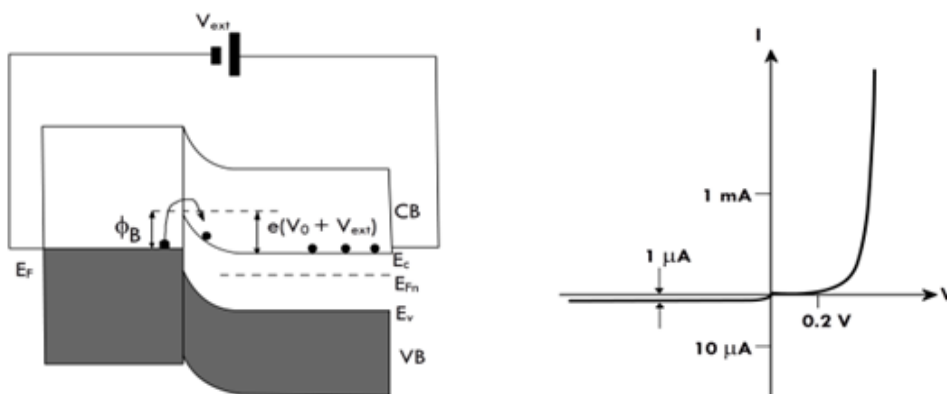
Figure 2. 15: *Schottky junction under reverse bias (left) and I - V characteristics of a Schottky junction showing rectifying properties (right)*

2.4.2 Ohmic contact

Current flowing through an ohmic contact is the linear function of the applied voltage and conduction is possible under both forward and reverse bias. In this case, the *I-V* relation obeys Ohm's law. The resistance for such a contact is negligible in comparison to the bulk one. A good ohmic contact should not significantly degrade device performance and can pass the required current with a voltage drop that is small compared to the drop across the active region of the device. An ohmic contact is formed on an *n*-type semiconductor when the ($\Phi_m < \Phi_s$) [21; 40-42]. And the opposite sign holds for *p*-type semiconductor.

At equilibrium, electrons move from the metal to the empty states in the conduction band so that there is a build-up region near the interface on the side of the semiconductor. The build-up region has a high conductivity than the bulk of the semiconductor as a result of high electrons concentration. Thus, an Ohmic junction behaves as a resistor conducting in both forward and reverse bias. The resistivity is determined by the bulk resistivity of the semiconductor [40].

References

[1] Streetman B G and Banerjee S, 2005 *Solid state electronic devices* (Prentice Hall: New Jersey) 6th ed.

[2] Pierret R F, 1996 *Semiconductor device fundamentals* (McGraw Hill Higher Education: New York) 3rd ed.

[3] Neamen D A, 1997 *Semiconductor physics and devices* (Tom Casson: London) 2nd ed.

[4] Kittel C , 1976 *Introduction to solid state physics* (Wiley: NewYork) 7th ed.

[5] Schroder D K, 2006 *Material and device semiconductor* (Wiley-IEEE: New Jersey) 3rd ed.

[6] Sze S M and Ng K K, 1981 *Physics of semiconductor physics* (John Wiley Sons Inc: New York).

[7] Enderlein R and Horing N J M, 1997 *Fundamentals of semiconductor physics and devices* (World Scientific: Singapore) 1st ed.

[8] Kasap S O, 2006 *Principles of electronic materials and devices* (McGraw-Hill Education: New York) 3rd ed.

[9] Colinge J-P and Colinge C A, 2005 *Physics of Semiconductor Devices* (Springer-Verlag: New York) 1st ed.

[10] Yacobi B G, 2003 *Semiconductor Materials: An Introduction to Basic Principles* (Kluwer Acaemic: London) 1st ed.

[11] Yu P Y and Cardona M, 1999 *Fundamentals of Semiconductors: Physics and Material Properties* (Springer: New Jersey) 3rd ed.

[12] Sharma R K and Rawal D S, 2019 *Physics of Semiconductor Devices* (Springer International:New York) 1st ed.

[13] Plummer *et al.*, 2000 *Silicon VLSl Technology: Fundamentals, Practice and Modeling* (Prentice Hall: New Jersey) 1st ed.

[14] Grove A S, 1967 *Physics and Technology of Semiconductor Devices* (Wiley:New York) 1st ed.

[15] Shur M, 1990 *Physics of Semiconductor Devices* (Prentice Hall:Englewood Cliffs) 1st ed.

[16] Fretwurst E *et al.,* 2003 *Nucl. Instr. Meth. A* **514** 1.

[17] Watkins G D, 2000 *Mater. Sci. Semicond. Process*. **3** 227.

[18] website1://inis.iaea.org/collection/NCLCollectionStore/_Public/04/079/4079741.pdf,

Acccessed-October 2019.

[19] Garutti E and Musienk Y, 2019 *Nucl. Inst. Meth. A.* **926** 69.

[20] Dittongo S *et al.,* 2004 *IEEE Trans. Nucl. Sci.* **51** 5.

[21] Messenger G C, 1992 *IEEE Trans. Nucl. Sci.* **39** 468.

[22] Junkes A, 2011 *Influence of Radiation Induced Defect Clusters on Silicon Particle Detectors* (Universty of Hamburg: PhD Thesis).

[23] Instrume S *et al.,* 1997 *Noise in GaAs detectors after irradiation*, **395** 141.

[24] Moll E, Fretwurst E and Lindstro G, 1999 *Nucl. Instr. Meth. A* **426** 87.

[25] Spieler H, 1997 *AIP Conf. Proc.* **390** 23.

[26] Macevoy B C, 1997 *Nucl. Inst. Meth. A.* **388** 365.

[27] Klanner R *et al.,* 2013 *Nucl. Instr. Meth. A.* **730** 2.

[28] Lazo M S and Woodall D M, 1987 "*Silicon and silicon dioxide neutron damage functions"* (Sandia National Laboratories*)(*Tech. Rep.) vol.1 SAND87.

[29] Pacifico N, 2012 *Radiation Damage Study On Innovative Silicon Sensors For The CMS Tracker Upgrade* CERN-PhD Thesis.

[30] Summers G P *et al.,* 1993 *IEEE Trans. Nucl. Sci.* **40** 1372.

[31] McPherson M, Jones B K and Sloan T, 1997 *Semicond. Sci. Technol.* **12** 1187.

[32] Eichhorn T, 2015 *Development of Silicon Detectors for the High Luminosity LHC* University of Hamburg:PhD Dissertation.

[33] Kraner H W, Li Z and Posnecker K U, 1989 *Nucl. Instr. Meth. A* **279** 266.

[34] Simić, B *et al.,* 2013 *Int. J. Photoenergy* **2013** 1.

[35] Nicollian E H and Brews J R, 1982 *MOS (Metal Oxide Semiconductor) Physics and Technology* (Wiley: Toronto).

[36] Aigrain P, 1958 *J. Phys. Chem. Solids.* **5** 237.

[37] Brutscher N and Hoheisel M, 1988 *Solid. State. Electron.* **31** 87.

[38] Cakar M, Türüt A and Onganer Y, 2004 *J. Mater. Sci. Mater. Electron.* **15** 47.

[39] Averine S *et al.,* 2000 *Appl. Physics Letters* **77** 274.

[40] Moloi S J and McPherson M, 2013 *Radiat. Phys. Chem.* **85** 73.

[41] Jones B K and McPherson M, 1999 *Semicond. Sci. Technol.* **14** 667.

[42] Karataş Ş and Türüt A, 2006 *Nucl. Instr. Meth. A* **566** 584.

Chapter 3

Ion implantation

Impurities are introduced into silicon to modify electrical properties of the material for fabrication of device for various applications including radiation detectors. One of the methods by which impurities are introduced into the material is by ion implantation. The impurities introduced are facilitated by the kinetic energy of the specific ions. As they incident in the bulk, the ions loose energies through elastic and inelastic collision and eventually stopping at a certain depth within the material. An impurity ion is said to have been implanted in the material when all its energy has been lost to the substrate atoms. Hence, the implantation energy of the impurity ions depends on the material and desired depth at which the impurity must be inside the material [1].

3.1 Ion stopping in solid

Loss of energy by ions in a material is the factor which determines the final scattering of ions and defects. The average energy loss per unit length of penetration into homogenous medium by a charged particle or projectile is the quantity referred to as the stopping power, $\frac{dE}{dx}$, of the medium. An energetic ion penetrating a material loses its energy mainly via nuclear energy loss and electronic energy loss processes. Therefore, the sum of nuclear stopping and electronic stopping for an ion coming to rest at a depth x below the target surface can be expressed as the total stopping power [2] as:

$$S = -\frac{dE}{dx} = \left(\frac{dE}{dx}\right)_{nuclear} + \left(\frac{dE}{dx}\right)_{electronic} \tag{3.1}$$

Dividing S by the target density, N, the stopping cross section is derived as:

$$\zeta = -\frac{1}{N}\left(\frac{dE}{dx}\right) = -\frac{1}{N}\left(\frac{dE}{dx}\right)_{n} - \frac{1}{N}\left(\frac{dE}{dx}\right)_{e} = S_n + S_e \tag{3.2}$$

where dE represents the differential energy loss for the particle under deliberation within the material and dx is the elemental distance measured along the direction of the incident ion. S_n and S_e are the nuclear and electronic stopping cross sections, respectively. The independence of nuclear stopping and electronic stopping suggests that the stopping power is dependent on the energy E of the ion, as can be observed in figure 3.1.
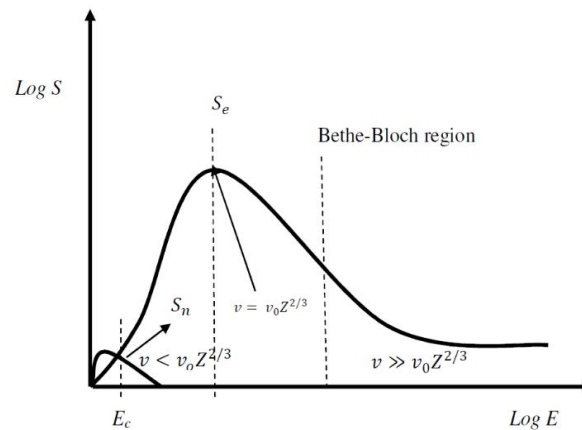
Figure 3.1: *The dependences of electronic stopping S_e and nuclear stopping S_n contributions to the stopping cross section as a function of the ion energy E* [3].

At low energies the nuclear stopping energy loss process is the dominant mechanism while at high energy it decreases and electronic stopping dominates. This shift in the dominant energy loss mechanism is shown in figure 3.1. It can be observed in the figure that electronic stopping begins to dominate above the critical energy ,E_c, that is, where the contributions of nuclear and electronic cross sections are the same then reaches a maximum and then decreased again towards the high energy region described by the Bethe-Bloch equation [3] where the ion has a shorter time to interact with the target atoms at the high ion velocities.

3.1.1 Nuclear stopping

Nuclear stopping (S_n) occurs when implanted ion loses energy due to elastic collision with the nuclei of the target atom. The energy lost by the implanted ion is transferred from its lattice site to the target atom. Nuclear stopping is responsible for the defects introduced into crystals during ion implantation. Nuclear stopping depends on the distance of closest

approach of the ion to target atom as the interaction potentials are strongly dependent on the distance separating the two nuclei. At low energies, nuclear stopping is the dominant mechanism. The velocity of the ion at these low energies is lower than that of the critical velocity (v_c) of the valence electrons [4]. The critical velocity is expressed [4] as:

$$v_c = v_0 Z_1^{\frac{2}{3}}$$

(3.3)

where $v_0 \left(= \frac{e^2}{\hbar}\right)$ is the Bohr velocity and $\hbar$ is the reduced Planck's constant $\frac{h}{2\pi}$.

3.1.2 Electronic stopping

Electronic stopping (S_e) occurs whereby incoming ions interact inelastically with the target electrons and loses its kinetic energy to the target electrons. Processes that facilitate this transfer of kinetic energy from the incident ion to the target electron include electron-electron collisions, excitation or ionization of target atoms and excitation, ionization or electron-capture of the incident ion [5]. A model based on the ion velocity is used to describe the energy loss process. The basis of which arises from comparing the ion's velocity with the Bohr velocity.

The first region of this model deals with the low energy region. In this region the ion velocity is lower than $v_0 Z_1^{2/3}$ [2]. Ion cannot transfer its energy to electrons lower that the Fermi energy to excite them to unoccupied states in this region [6] and therefore, can only transfer its energy to electrons close to the Fermi energy. Since the transferred energy from the projectile to the target electron is proportional to the projectile velocity, the electronic stopping power is proportional to the projectile velocity [7] as:

$$S_e = 19.2 \frac{Z_1^{7/6} Z_2 v_1}{\left(Z_1^{2/3} + Z_2^{2/3}\right) v_0} \left[\frac{\text{eVcm}^2}{10^{15}\text{at}}\right]$$

(3.4)

33

In the second region of which the velocities of the ions are far greater than $v_0 Z_1^{2/3}$. In this region, the ion stripped off all its electrons as shown by Bethe and Bloch in figure 3.1. The electronic stopping in this region is given by the Bethe-Bloch equation [8]:

$$S_e = \frac{4\pi Z_1^2 Z_2 e^4}{m_e v_1^2}\left[\ln\left(\frac{2m_e v_1^2}{I}\right) + \ln\left(\frac{1}{1-\beta^2}\right) - \beta^2 - \frac{S_c}{Z_2}\right] \tag{3.5}$$

where $\beta = \frac{v}{c}$ with c being the speed of light, I is the average ionization potential and is theoretically defined as $\ln I = \sum_n f_n \ln E_n$ and $\frac{S_c}{Z_2}$ is the shell correction, while E_n and f_n are the possible energy transitions and corresponding oscillator strengths for target atoms, respectively [8].

The third region is the intermediate one, i.e. between part 1 and part 2, the region where $v \approx v_0 Z_1^{2/3}$. The ion, to a large extent, becomes ionized and electronic stopping reaches its maximum in this region. In accordance to [9], the average charge state of the projectile is dependent on its energy and target material in this range. From figure 3.1, it can be seen that at the energy above the critical energy (E_c) electronic stopping starts to dominate and after reaching a maximum, it starts to decrease in the high energy region [1].

The term $v_0 Z_1^{2/3}$ was estimated to be 3.67×10^7 m/s for Er. At 60 keV, Erbium ions have an initial velocity of 2.63×10^5 m/s while the initial velocity of the 160 keV Er ions is 4.65×10^5 m/s. Due to these low velocities, the incident Er ions are unable to transfer sufficient energy to electrons lower in the energy level than the Fermi level. Hence, only the electrons in the energy level close to the Fermi level influence electron energy loss.

The important domains for the purposes of this dissertation are the low and intermediate energy regions, since the study reports on the result of erbium ions for 60 keV and 160 keV

that were implanted into Si (a low energy regime) and analysed by Rutherford backscattering Spectrometry (*RBS*) using 2 MeV -particles (an intermediate energy regime).

3.1.3 Energy straggling

Energy is lost by energetic incident particles penetrating a substrate through several interactions with a target's atoms, which often lead to statistical uncertainty in the collision processes. Identical particles initially having the same velocity will not necessarily have the same energy after traversing the same thickness in homogenous material. The resulting statistical uncertainty in the energy of particles penetrating a solid, leads to a statistical distribution in both the number and size of events for a certain depth of penetration. This discrete nature of the energy loss processes, resulting in uncertainty in energy is known as energy straggling.

As a result, energy profile broadens as a function of the distance travelled through the target. This energy loss along a given path length is distributed around a mean value. According to [11], the variance, Ω_B^2, in the number of collisions experienced by an energetic particle when passing through a solid of thickness Δx, having atomic density N is given [5] as:

$$\Omega_B^2 = 4\pi(Z_1 e^2)^2 N Z_2 \Delta x \tag{3.6}$$

where Ω_B^2 is Bohr's energy straggling, Ω_B^2 is the same as the variance of the average energy loss of a projectile after passing through a target of thickness Δx with Ω_B which is the standard deviation of the energy broadening [2]. The energy distribution at a given depth is assumed to be Gaussian. Therefore, the full width at half maximum (FWHM) of the energy loss distribution can be expressed [2] as:

$$\text{FWHM} = 2\Omega_B\sqrt{2\ln 2} \tag{3.7}$$

which is 2.35 Ω for energy straggling.
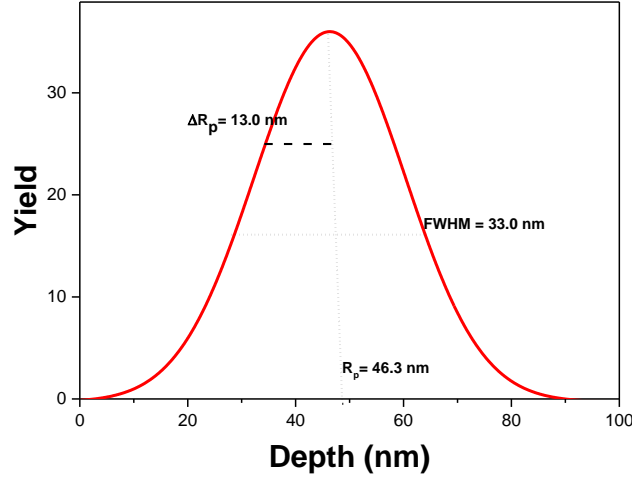
Figure 3.2: *Normalized distribution of 160 keV erbium ions in silicon as a function of implantation depth. The projected range, R_p, projected range straggling ΔR_p and the full width at half maximum (FWHM) and their values are indicated in the figure. Values were obtained by fitting the as-implanted Er spectrum depth profile with a Gaussian distribution [10].*

Bohr's theory is only valid for high energies in Beth-Bloch region where ion stripped off all its electrons. Consequently, Bohr's theory is unable to explain the lower energy case where the ion did not strip off all its electrons. Corrections term for lower energies cases were introduced by several researchers [2] by extending Bohr's point charge assumption theory for energies where the assumptions may not be valid [12].

For ion velocities below E_0 keV [10]:

$$\Omega = \Omega_B^2 \frac{1}{2} L(\chi) \text{ for } \chi \leq 3 \tag{3.8}$$

and

$$\Omega = \Omega_B^2 \text{ for } \chi > 3 \tag{3.9}$$

where χ is a reduced energy variable given by:

$$\chi = v^2/Z_2 v_0^2 \tag{3.10}$$

and $L(\chi)$ is the stopping number.

3.1.4 Range and range straggling

Energy is lost when an energetic ion penetrates a material through nuclear energy loss and electronic energy loss until it comes to rest. Due to the statistical fluctuation of interactions during the energy loss processes and multiple scattering of the ion from the target atoms, the ion's path is "zigzags". These statistical fluctuations cause ions with the same energy to be implanted at different depths. The total distance, which the ion travels from the surface to where it stops, is called the total range or range and is calculated by taking into consideration the stopping cross sections [12]:

$$R = \frac{1}{N} \int_0^{E_0} \frac{dE}{dx} \qquad (3.11)$$

The deviation of the range due to energy straggling is called range straggling ΔR_p and is primarily due to the multiple collisions of the ions which will result in the fluctuations of the ions from their initial directions and lead to a spread in the range of the ion beam in the target [2]. Figure 3.3 depicts two charged particles penetrating a material, i.e. one particle with a low incident energy and another with a high incident energy [1]. The path of the energetic ions with high energy after penetrating the material is straight because electronic stopping dominates and no nuclear stopping is experienced. As the velocity decreases there are collisions with the target atoms and ions experience a zigzag path when their energies are low. For the lower incident energy ion, the path is a zigzag one since the nuclear and electron stopping is of similar magnitudes.

The total range of all the ions is given as:

$$\frac{R_{\text{tot}}}{u} = \sum l_i \qquad (3.12)$$

where u is the total number of ions implanted into the sample and l_i is the different path lengths the ions travel inside the material.
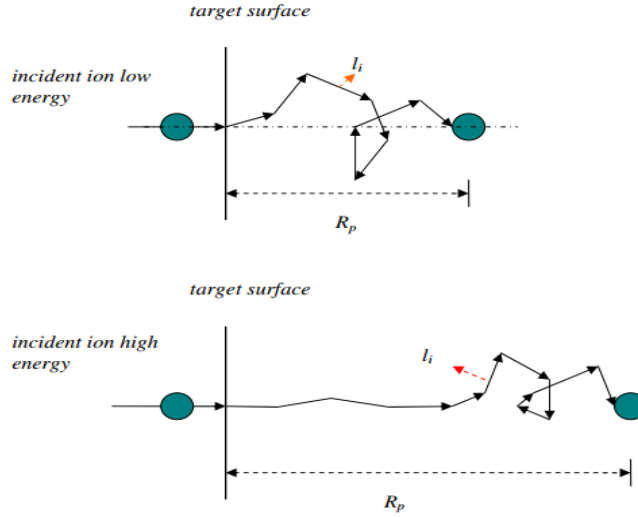
Figure 3.3: *Range concepts for incident ions with low (top figure) and high (bottom figure) energies in target material* [1].

The average range measured parallel to the incident ion direction of the ions penetrating the material from the target surface to where it comes to rest at a particular depth is called the projectile range (R_p) as shown in figure 3.3. The total range is always longer than other ranges because it takes into consideration the entire ion implanted paths taken inside material. The impurity profile as a function of depth is approximately Gaussian because of the range straggling effect. The concentration of impurity ions implanted at low energy to a fluence of ϖ at a depth g in a target of atomic density N is related to R_p and ΔR_p and it is given [13] as:

$$Q(g) = \frac{\varpi}{\sqrt{2\pi N \Delta R_p}} e^{\left[\frac{-(g-R_p)^2}{2\pi \Delta R_p^2}\right]}$$ (3.13)

where g is the position of the incident ions in the target, ϖ is the implantation dosage.

The other instants measured in a general implantation profile are skewness and kurtosis. Skewness, γ, is the measure of the implantation profile's tendency to rest towards or away from the projected range, R_p. The skewness of a profile can either be positive or negative. Skewness of an implantation profile can be expressed [1] as:

$$\gamma = \int_{-\infty}^{\infty} (g - R_p)^3 n(g) dg$$ (3.14)

38

Kurtosis, β, is the measure of the flatness of the implanted profile. For a perfect Gaussian profile, kurtosis is equal to 3. The kurtosis of an implantation profile is given as:

$$\beta = \int_{-\infty}^{\infty} (g - R_{\mathrm{p}})^4 n(g) dg \qquad (3.15)$$

3.2 Stopping and range of ions in matter (SRIM)

For ion implantation simulation, radiation damage, sputtering, reflection and transmission of impinging ions, several computer codes have been developed over the years to help in simulating different implantation parameters and moments such as projected range (R_{p}), straggling (ΔR_{p}) and skewness (γ) [14]. Monte Carlo simulation method and binary collisions algorithm are used to estimate the trajectory of implanted species due to the statistical nature of the paths of the implanted species [14]. Different programs are embedded within SRIM and the transport of ions in matter (TRIM) program is the most detailed of them.

However, TRIM, does not take into consideration the crystal structure and the dynamic composition changes in the material that occurs when the incident ion penetrates the target material. Some of the assumptions made by TRIM include:

1. SRIM program does not take the crystallinity of the target into consideration i.e. it assumes that the substrate is amorphous.

2. Predictions of the projected range are based on binary collisions alone (Effects of neighbouring atoms are neglected).

3. Electronic and nuclear stopping powers are an averaging fit to a large number of experimental data points.

4. Recombination of interstitials with vacancies is neglected.

In this study, the stopping and range of Ions in Matter (SRIM) program was used to estimate the physical parameter involved when erbium is implanted in silicon. As implanted in silicon,

erbium creates defects vacancy and interstitials in silicon. The parameters estimated include the density of vacancy and interstitials created. The program was also used to predict the effect of erbium ion implantation on silicon and the values obtained were then compared with the experimental depth profiles acquired using Rutherford backscattered spectrometry technique in this work.

References

[1]   Odutemowo O S, 2016 *Investigating Effect of Fission Products Bombardment on Glassy Carbon* (PhD Thesis: University of Pretoria).

[2]   Chu W K, Mayer J W and Nicolet M, 1978 *Backscattering Spectrometry (*Academic Press: New York) 1st ed.

[3]   Bethe H , 1930 *Ann. Phys.* **397** 325.

[4]   Dearnaley G, Freeman J H, Nelson R S, and Stephen J, 1973 *Ion Implantation (Defects in Crystalline Solids)* (North Holland:Amsterdam). *Vol.* 8. 1st ed.

[5]   Ziegler J F, Biersack J P and Littmark U, 1985 *The stopping and ranges of ions in matter,* Pergamon Press:New York, Vol. 1. 1st ed.

[6]   Lindhard J, Scharff M and Schiott H E, 1963 *Mat. Fys. Medd. Dan. Vid. Selsk*. **33** 1.

[7]   Lindhard J and Scharff M ,1961 *Phys. Rev.* **124** 128.

[8]   Bloch F, 1933 *Ann. Phys.* **408** 285.

[9]   Zolnai Z, 2005 *Irradiation-induced crystal defects in silicon carbide, (*PhD. Thesis: Budapest University of Technology and Economics*)*

[10]   Bird J R and Williams J S, 1989 *Ion Beams for Materials Analysis* (Academic Press:Sydney)1st ed.

[11]   Rimini J W M E, 1977 *Ion Beam Handbook for Material Analysis (*Academic Press:New York) 1st ed.

[12]   Lindhard J and Nielsen V, 1962 *Phys. Lett.* **2** 209.

[13]   Mayer J W, Nicolet M A and Chu W K, 1975 *Journal of Vacuum Science and Technology* **12** 356.

[14]   Ziegler J F, 2013 *SRIM, Http//www. Srim. Org.*

Chapter 4

Characterization techniques

This chapter details characterization techniques that were used in this study. For this study, silicon substrates were implanted with erbium (Er) ions at room temperature. The implanted silicon was annealed at different temperatures, 800 ℃ and 1000 ℃, to diffuse erbium in silicon and to recover the damage induced by ion implantation. X-ray diffraction *(XRD)* and Rutherford backscattering spectrometry channelling *(RBS-C)* techniques were used to characterize the erbium implanted silicon samples. These material characterization techniques were carried out in order to establish the presence of erbium and its diffusion mechanisms in silicon. The techniques were also used to study the thermal damage recovery of the silicon.

Schottky diodes were fabricated on un-implanted and Er implanted silicon samples. Current-voltage *(I-V)* and capacitance-voltage *(C-V)* are device characterization techniques that were carried out on the fabricated diodes to study a change in electrical properties of the diode due to the implantation at room temperature.

4.1 Material characterization techniques

Material characterization techniques were used to establish the presence of erbium in silicon. The techniques were also used to investigate a change in crystal structure and atomic spacing in the crystal due to the implantation and also, to study the diffusion mechanisms of erbium in silicon. In addition, other elements that were unintentional introduced in silicon were identified using the techniques.

4.1.1 Rutherford backscattering spectrometry

Rutherford backscattering spectrometry (*RBS*) as a method for materials analysis was firstly described in 1957 by Rubin [1], and in the 1960's it was developed to a materials

characterization technique particularly useful for the growing semiconductor field [2]. Rutherford Backscattering Spectrometry (*RBS*) is an ion scattering technique for quantitative composition analysis of thin layers or near surface regions of solids. It allows fast non-destructive analysis of materials and multi-element depth concentration profiles [3]. This technique is based on the analysis of the energy of backscattering particles. Typically, protons, helium, and sometimes lithium ions are used as projectiles at backscattering angles [4]. In our experiments, we used helium particles.

When incoming energetic particle strikes the target material, the particle will lose energy as it penetrates the target and stop inside the material. A fraction of the particles is backscattered [5, 6]. Depending on the backscattered angle some of the backscattered particles are detected by the detector. The detector is normally placed at an angle greater than $90°$ and less than $180°$ to the incoming beam as shown in figure 4.1. Different information of the target can be gathered from the detected backscattered particles such as mass and depth distributions of the target elements.
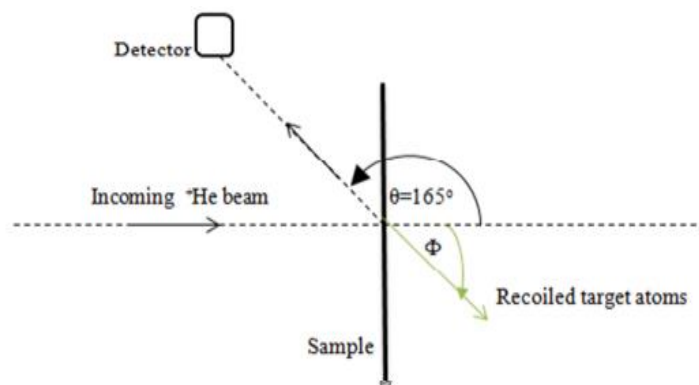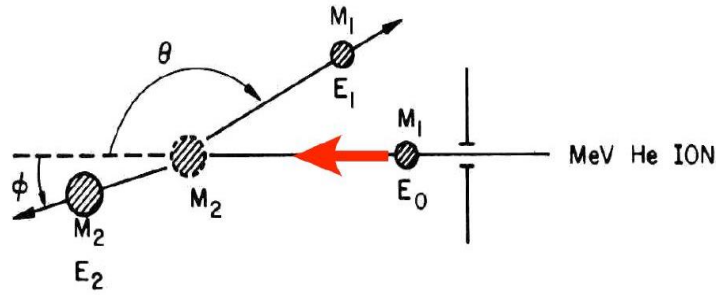

Figure 4.1: *Schematic diagram showing the RBS experimental setup.*

4.1.1.1 Kinematic factor (K)

The kinematic factor is defined as the ratio of the backscattered particle's energy E_1 after collision to the incident energy E_0 before the collision [2]. It is expressed as:

$$K = \frac{E_1}{E_0} = \left\{ \frac{M_1 \cos\theta \pm \sqrt{M_1^2 sin^2\theta}}{M_1 + M_2} \right\}^2 \qquad (4.1)$$

where M_1 and M_2 are the atomic masses of helium particle and target atom respectively, E_0 and E_1 are the energies of the incident and backscattered helium particle respectively, and θ is the backscattered angle. The plus sign in equation 4.1 is used when $M_1 < M_2$, while the minus sign is used when $M_1 > M_2$ [3]. In our case the plus sign is applicable because the mass of the target atom is greater than that of the helium particles as depicted in figure 4.2.

Figure 4.2: *A schematic diagram showing the RBS backscattered angle θ.*

4.1.1.2 Differential cross section

The differential cross section for scattering i.e. $d\sigma/d\Omega$ in a given direction into the detecting solid angle $d\Omega$, is defined as the number of particles scattered into a solid angle $d\Omega$ per number of incident particles per unit area [7]. The differential cross section for the scattering angle of a projectile into a solid $d\Omega$ centered around an angle θ and is given [7] as:

$$\left(\frac{d\sigma}{d\Omega} \right)_{projectile} = \left(\frac{Z_1 Z_2 e^2}{4E_0} \right)^2 \frac{4\left(M_2 \cos\theta + \sqrt{M_2^2 - M_1^1 sin^2\theta} \right)^2}{M_2 \sin^4\theta \sqrt{M_2^2 - M_1^2 sin^2\theta}} \qquad (4.2)$$

The differential cross section has a proportionality relation with the atomic number of the target Z_2 i.e. $\left(\frac{d\sigma}{d\Omega} \propto Z_2^2 \right)$, which means the *RBS* is more sensitive to heavy elements as compared to light elements. The inverse proportionality of E_0 to the differential cross section i.e. $\left(\frac{d\sigma}{d\Omega} \propto \frac{1}{E_0} \right)$, shows that as the energy increases as the backscattering yield decreases.

44

The probability of an incident ion being scattered into a solid angle of the detector, Ω, at a scattering angle, θ, is known as scattering cross section, σ. The total number of backscattered and detected particles is given as [8]:

$$B_n = \sigma \Omega P_{in} T \Delta x \qquad (4.3)$$

where B_n is the number of detected particles, $\sigma \Omega$ is the differential cross section averaged over the surface of the detector, P_{in} is the total number for incident projectiles, $T \Delta x$ is the total number of target atoms per unit area. From equation (4.3), we can see that if B_n, σ, Ω and P_{in} are known we can obtain $T \Delta x$.

4.1.1.3 Depth profiling

The backscattered helium particles from different depths within the target material have different energies. The incident particle of energy E_0 that backscatters at the surface has energy of KE_0. This incident particle loses some of its energy as it penetrates along the inward path and has energy E before it undergoes backscattering at depth x as depicted in figure 4.3 [9]. Hence, energy E_0 is greater than energy E. As the particle backscattered at depth x, it also loses energy along the outward path. The particle emerging from the surface has energy E_1. Thus, E_1 is less than E.
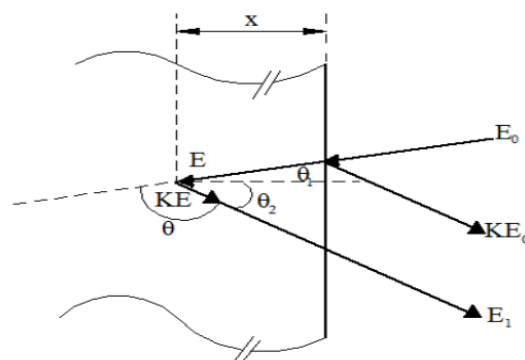
Figure 4.3: *A schematic diagram showing the backscattering events in a target particle and the energy loss from depth x [10;11].*

Figure 4.3 shows the energy E with the inward path when the particle loses energy can be related as:

$$\frac{x}{\cos\theta_1} = -\int_{E_0}^{E} \frac{1}{\left(\frac{dE}{dx}\right)} dE = -\int_{E_0}^{E} \left(\frac{dx}{dE}\right) dE \qquad (4.4)$$

Similarly, the outward path is related to KE and E_1 by:

$$\frac{x}{\cos\theta_2} = -\int_{KE}^{E_1} \frac{1}{\left(\frac{dE}{dx}\right)} dE = -\int_{KE}^{E_1} \left(\frac{dx}{dE}\right) dE \qquad (4.5)$$

The energy difference $E_0 - E$ is the energy loss along the inward path ΔE_{out}. Particles backscattered at the surface have the energy of KE_0. If $\frac{dE}{dx}$ has a constant value along the inward and outward paths, equations (4.4) and (4.5) are reduced [7] to:

$$E = E_0 - \frac{x}{\cos\theta_1} \frac{dE}{dx} I_{in} \qquad (4.6)$$

and

$$E_1 = KE - \frac{x}{\cos\theta_2} \frac{dE}{dx} I_{out} \qquad (4.7)$$

respectively. Here the subscript 'in' and 'out' refer to the constant values of $\frac{dE}{dx}$ along the inward and outward paths. By elimination of E from equation (4.8) and (4.9) we have:

$$KE_0 - E_1 = \left[\frac{K}{\cos\theta_1} \frac{dE}{dx} I_{in} + \frac{1}{\cos\theta_2} \frac{dE}{dx} I_{out}\right] x \qquad (4.8)$$

where KE_0 is the energy of the backscattered helium particles at the surface atoms of the target and E_1 is the energy of the backscattered helium from the atom at depth x. Taking ΔE to be the energy difference between E_1 and KE_0:

$$\Delta E = KE_0 - E_1 \qquad (4.9)$$

The equation 4.8 can be written as

$$[S] = \left[\frac{K}{\cos\theta_1} \frac{dE}{dx} I_{in} + \frac{1}{\cos\theta_2} \frac{dE}{dx} I_{out}\right] \qquad (4.10)$$

where $[S]$ is called the backscattered energy loss factor and it allows for a depth scale to be applied to a backscattering energy spectrum. Thus, a measured energy spectrum can therefore directly be converted into a depth scale [12].

4.1.1.4 *RBS* with channelling (*RBS*-C)

When an energetic ion beam is aimed near a major crystalline direction of a single crystal, the channelling process occurs. During this process, ions are steered into open spaces between close-packed planes of atoms in a crystal where they undergo a series of correlated, small angle collisions with the nuclei that line the channels [11].

The open channels in a crystal are categorized into two groups, viz. axial and planar channels. The axial channel is defined by rows of atoms around the trajectory. The axial alignment in the spectrum has damped yield oscillation near the surface region and has a lower minimum backscattering yield as shown in figure 4.4.
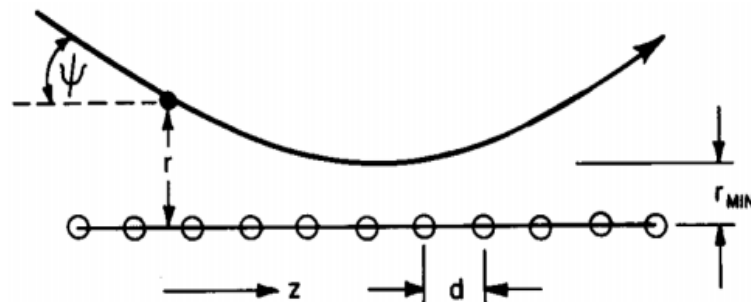
Figure 4.4:*Continuum model for ion scattering from an axial string of atoms* [11].

Lindhard's work [13] introduced the continuum model which describes channelling in a continuum description of atomic strings (axial channelling) and planes (planar channelling). The continuum model is based on continuum potentials taken as an average individual ion-atom collision. Thus, this model assumes that ion-string or ion-plane scattering as illustrated in figure 4.4 can be approximated from a string of atoms. The discrete nature of the atoms in the string is assumed to be negligible [5].

The continuum potential can be used to describe the axial channelling [5]. This potential is given [5] as:

$$U(r) = \frac{1}{d} \int_{-\infty}^{\infty} P_v \left[(z^2 + r^2)^{\frac{1}{2}} \right] dz \qquad (4.13)$$

where P_v is the interatomic potential, r is the height and z is the direction in which the particles move.

The planar channel on the other hand is defined by parallel atomic planes. Planar alignment has clear yield oscillation near the surface region and has high backscattering yield [2]. Figure 4.5 shows the normalized yield of backscattered particles for spectra of axial and planar alignment, where χ_{MIN} is the minimum yield, which is the ratio between the aligned and random yield near the surface.
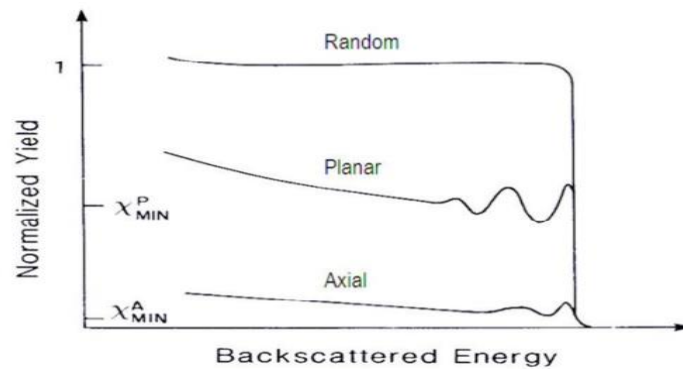
Figure 4.5: *RBS channelling spectra showing axial and planar channelling. χ_{MIN}^{P} and χ_{MIN}^{A} are planar and axial minimum yield respectively* [7].

For channelling to take place, the ion incident angle upon a channel of atoms must be smaller than the critical angle ψ_c, [14], such that the ions are reflected away from the row of atoms continuously by the correlated series of many consecutive collisions with the atoms in the row. The critical angle is given [14] as:

$$\psi_c = \left(\frac{2Z_1 Z_2 e^2}{E_0 d} \right)^{\frac{1}{2}} \qquad (4.12)$$

where d is the atomic spacing along the aligned row, ψ_c is a theoretical parameter and is directly proportional to the angular half width at half $\psi_{1/2}$ of the angular scan profile depicted in figure 4.6.
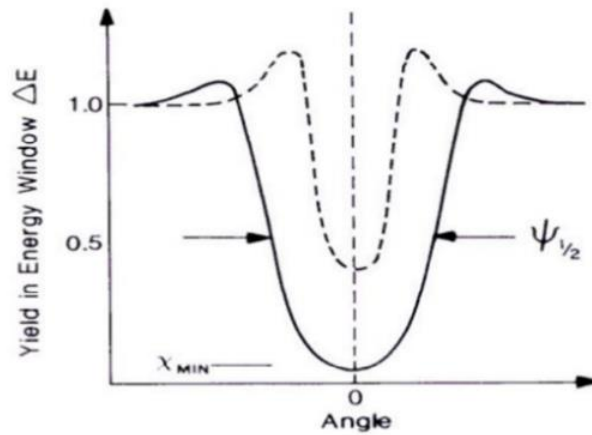
Figure 4.6: *The angular yield about an axial channel (solid curve) and a planer channel (broken line)* [7].

Above this critical angle, the particles begin to approach the row of atoms so closely that the particle will start to feel the effect of the atoms in the row individually and the particle will experience large angle scattering and will de-channelled. Dechannelling occurs when some of the channelled ions are scattered away as they penetrate the solid during the channelling process. It is due to the presents of defects such as substitution impurities, interstitial atoms and displaced lattice atoms (figure 4.7). In this case there will be an increase in the backscattering yield.

When ions are implanted in a material, damage is created, that is, the implanted ions displace the host/target material atoms from their original lattice site distorting the crystal structure and creating vacancies and interstitials. Rutherford backscattering spectrometry in a channel mode (*RBS-C*) helps us to study this damage. This channelling technique gives information of the amount and depth distribution of the damage created in the material. The radiation damage created during implantation differs according to the fluence and temperature of implantation. The random and aligned spectra give us information on whether the material is

amorphous (absence of long-range order) or whether the material retained its crystallinity with some damage created [2].
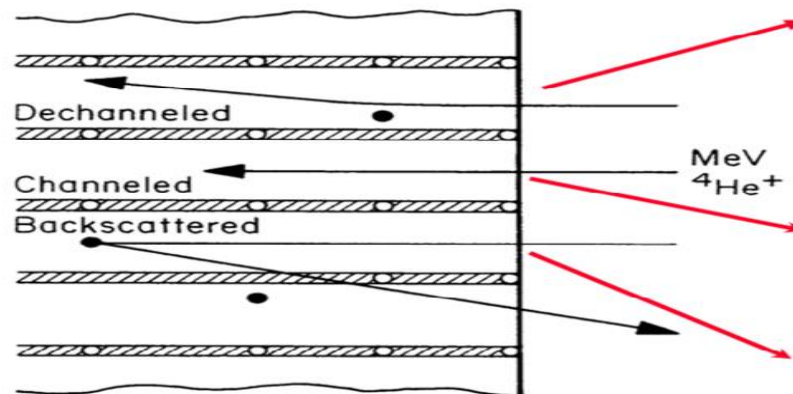
Figure 4.7: S*chematic representation showing channelling, Dechannelling and direct backscattering by interstitial atoms.*

4.1.2 X-ray diffraction

X-ray diffraction (*XRD*) technique is an effective non-destructive analytical technique for characterizing crystalline materials [15]**.** It is used for phase identification, to measure crystalline sizes in a material. When a beam of parallel monochromatic X-ray beam strikes a crystal lattice, the electromagnetic (EM) waves in the beam interact with the planes of atoms in the crystal structure to produce constructive interference and the X-rays leave the sample through the same angle [16]. The waves become scattered and the beam becomes diffracted [16] as described in figure 4.8.
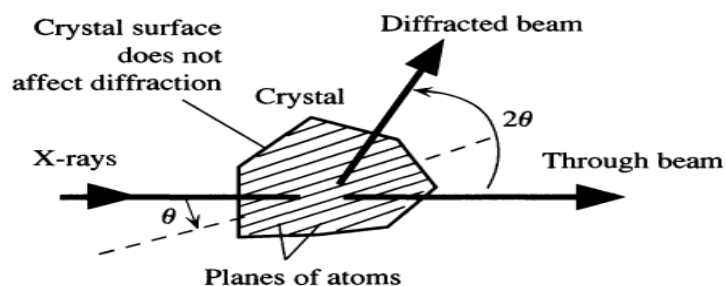
Figure 4.8: *A schematic illustration of X-ray diffraction by a crystal. X-rays penetrate the crystal and then become diffracted by a series of atomic planes [17].*

The angle between the incident x-ray beam and the lattice planes is called θ and that between the incident and scattered x-ray beams is called 2θ. The 2θ of maximum intensity is known as the Bragg angle. To give maxima in scattered intensity, the scattered beams should be coherently scattered at different lattice planes. These conditions result to the Bragg equation as:

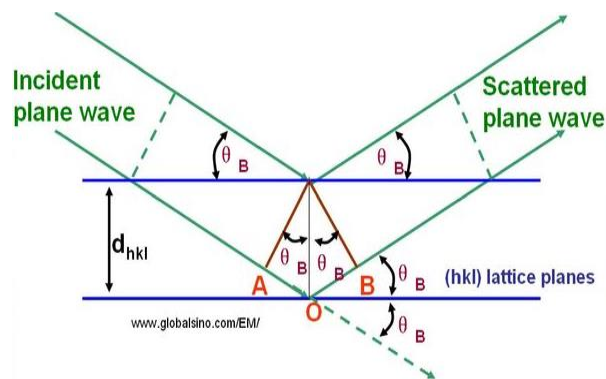$$n\lambda = 2d\ sin\theta \qquad (4.13)$$

where n a positive integer number representing the order of the diffraction, λ is the X-ray wavelength, d is the atomic spacing generating the diffraction and θ is the angle between the incident X-ray beam and the atomic lattice plane in the crystal dimensions of the unit cell in the crystal as depicted in figure 4.9.

Figure 4.9: *A schematic diagram of Bragg's reflection from a crystal.*

In three dimensions, all directions from the crystal that are at an angle 2θ to the incident beam define a cone as shown in figure 4.10. Several cones exist and each relating to a different set of diffraction planes with a distinct set of Miller indices denoted by the letters *h, k* and *l*. A particular (*hkl*) plane is the result of reflections from a series of parallel atomic planes [18-19]. Miller indices are used to describe directions in the crystal.

In a single crystal, atoms are spatial placed in a regular interval called the crystal's lattice parameter. Lattice parameters are the most important physical quantity in *XRD* as periodicity in atomic placement is the physical property that gives rise to *XRD* peaks [20].
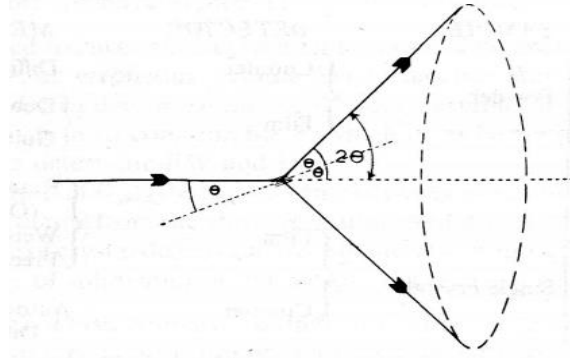
Figure 4.10*: A diffraction cone defined by all 2θ directions around the incident beam [16].*

In three dimensions lattice parameters are comprised of a set of three lattice constants referred to as (*a, b, c*) and three angles (α, β, γ) between them [18]. The separation between sets of parallel planes formed by the singular cells in a lattice structure is called atomic spacing (d) and is linked to the Miller indices of a plane (*hkl*). The separation d_{hkl} between adjacent (*hkl*) planes is given [19] by:

$$d_{\text{hkl}} = \frac{a}{\sqrt{h^2 + k^2 + l^2}}$$

(4.14)

where *a* is the lattice parameter.

When we substitute for $d = d_{\text{hkl}}$ in the Bragg condition in Equation 4.15, and rearrange the equation for (n=1), one gets:

$$\sin^2\theta = \frac{\lambda^2}{4a^2}(h^2 + k^2 + l^2)$$

(4.15)

Since in any specific case *a* and λ are constants and if $\frac{\lambda^2}{4a^2} = A$, equation (4.15) can be re-written as:

$$\sin^2\theta = A(h^2 + k^2 + l^2)$$

(4.16)

showing Bragg's law for three dimensional crystals and the diffraction angle increases with $(h^2 + k^2 + l^2)$.

All possible (*hkl*) planes in cubic crystals will generate diffraction peaks with diffraction angles satisfying the Bragg law. Equation (4.19) defines a diffraction pattern for the simple cubic crystal structure because it generates all the possible values of 2θ for all the planes in

52

the cubic crystal. In case of Face centred cubic (FCC) and Body centred cubic (BCC) crystals, however, not all (hkl) planes give rise to diffraction peaks predicted by Equation (4.16) for the reason that diffractions from certain planes are missing since the atoms on these planes give rise to reflections that are not in phase [16].

Diffraction pattern in figure 4.11 for an FCC crystal shows that only those planes with Miller indices that are all either odd or all even integers give rise to diffraction peaks. There are no diffractions from those planes with mixed odd and even integers.
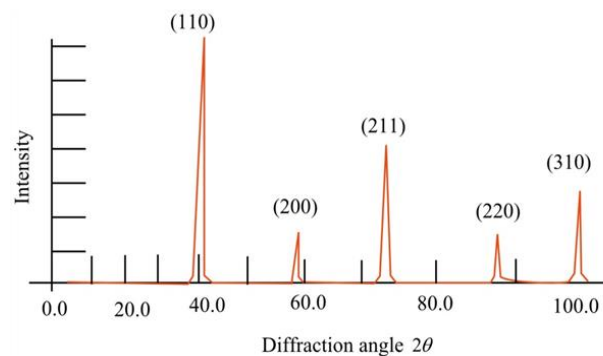
Figure 4.11: *for an FCC crystal shows that only those planes with Miller indices that are all either odd or all even integers give rise to diffraction peaks. There are no diffractions from those planes with mixed odd and even integers.*

An X-ray detector placed at an angle 2θ with respect to the beam will register a peak in the detected X-ray intensity. The diffraction peaks and the d-spacing show information about the location of lattice planes in the crystal structure. Each peak measures a d-spacing that represents a family of lattice planes, it also has an intensity which differs from other peaks in the pattern and reflects the relative strength of the diffraction [20].

The resultant of the waves scattered by all the atoms in the unit cell in the direction of the *hkl* reflection, is called the structure factor (F_{hkl}). The structure factor depends on both the position of each atom and its scattering factor. The general expression for the structure factor [20] is:

$$F_{hkl} = \sum_j f_j e^{2\pi i (hx_j + ky_j + lz_j)}$$

(4.17)

where f_j is the scattering factor of the jth atom while x_j, y_j, and z_j are its fractional coordinates. In a crystal with a centre of symmetry and *n* unique atoms in the unit cell, the above equation simplifies to:

$$F_{hkl} = 2 \sum_j f_j \cos 2\pi (hx_n + ky_n + lz_n)$$

(4.18)

The distribution of electron density within a crystal can be expressed using a three-dimensional Fourier series [21]. The electron density as a function of position *x,y,z* is the inverse Fourier transform of the structure factors [16]:

$$\rho(x, y, z) = \frac{1}{V_c} \sum_h \sum_k \sum_l F_{hkl} e^{-2\pi i (hx_n + ky_n + lz_n)}$$

(4.19)

where $\rho(x, y, z)$ is the electron density and V_c is the volume of the unit cell. The intensity of an *hkl* reflection (I_{hkl}) is proportional to the square of the structure factor:

$$I_{hkl} \propto F_{hkl}^2$$

(4.20)

Incident wave and the wave in the direction of observation will result in no phase between them as a result of the angle between the incident radiation and direction of observation being zero and the resulting wave will have the maximum intensity. As the angle increases, the wave of the outer electrons will gradually go out of phase. Their contribution then starts to cancel the waves in the direction of observation and the intensity of the resulting wave decreases.

Peak profile analysis can help generate information about the type and amount of defects in the sample [22]. The width of a peak profile can be described by different parameters such as the Full width at half maximum (FWHM) or the integral breadth (IB). The FWHM is also known as "half width" describes the width of a peak at half of its height as depicted in figure

4.12. The FWHM depends strongly from the Gauss/Lorentz contributions to the peak. If the reference point of the peak is unclear, the purpose of the FWHM suffers.
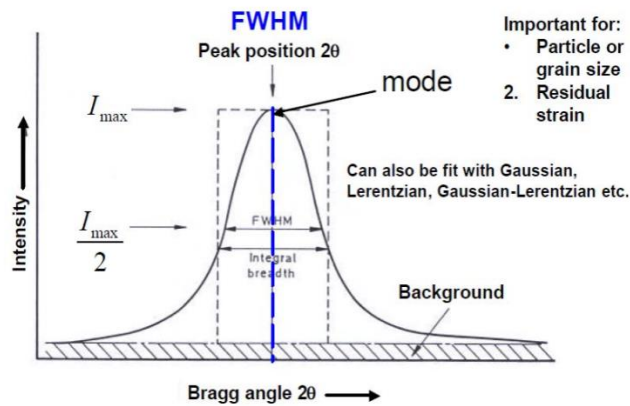
Figure 4.12: *Schematic diagram of FWHM for FCC.*

In figure 4.12 I_{max} denotes Peak maximum (or peak height), peak area is indicated as the area under the curve, peak width is a measure of the broadness of the peak. The integral breadth, on the other hand, is defined as the integral (area) of a peak divided by the peak height. Alternatively, it can be assumed as the width of a rectangle that has both the same area and height as the peak. This measure is less dependent from the shape of the profile.

Bragg diffraction should generate significantly sharp reflections. Peak width varies inversely with crystallite size. As the crystallite size gets smaller, the peak gets broader. The crystallite size broadening is highly evident at large angles 2θ, however, at larger angles, 2θ peak intensity is usually weakest.

The average crystallite size of the films is given by Scherrer's formula [23] as:

$$X_c = \frac{k\lambda}{B cos\theta} = \frac{k\lambda}{(B_M^2 - B_S^2)^{1/2} cos\theta} \tag{4.21}$$

where X_c is crystallite thickness, k is a dimensionless shape factor (values between 0.62-2.08), B is the full-width at half-maximum (FWHM) of the peak in radians, B_M and B_S are the FWHMs of the sample and a standard respectively. The Scherrer formula cannot be used

for grains larger than about 0.1 to 0.2 µm since it is limited to nano particles size [23]. The

Scherer formula provides a lower bound on the particle sizes.

4.2 Device characterization techniques

Current-voltage and capacitance-voltage techniques have been used in this work to

investigate a change in electrical properties of the silicon diodes due to erbium doping.

Diodes were fabricated on undoped and erbium-doped silicon.

4.2.1 Current-voltage

Current–voltage technique is used to measure the space charge density within a

semiconductor material [24-28] and is perhaps the most predictable measurements

performed. It is used widely to study the behaviour of devices since they offer important

parameters such as the saturation current, the ideality factor and the Schottky barrier height.

 From thermionic emission theory, the current-voltage relationship for Schottky barrier diode

is expressed [29-30] as:

$$I = I_0 \left[\exp\left(\frac{q(V_0 - IR_s)}{\eta K_{\mathrm{b}} T}\right) - 1 \right] \tag{4.22}$$

where the saturation current I_o is is expressed [31-32] as:

$$I_0 = \left[A_{\mathrm{r}} A^* T^2 \exp\left(\frac{-e\Phi_{\mathrm{B}}^{I-V}}{\eta K_{\mathrm{b}} T}\right) \right] \tag{4.23}$$

However, in real metal–semiconductor contacts, the current tends to rise as the reverse bias

grows. In equations (4.22 and 4.23) A_{r} is the diode area, A^* is the effective Richardson

constant (= $32\,\mathrm{A\,cm^{-2}K^{-2}}$ for *p*-type silicon and $112\,\mathrm{A\,cm^{-2}K^{-2}}$ for *n*-type silicon

respectively)[26] . R_s is the series resistance of the substrate and dominates in the higher bias

region and IR_s is the voltage drop across the series resistance, Φ_B^{I-V} is the effective Schottky barrier height at zero bias which is obtained [33-35] as :

$$\Phi_B^{I-V} = \frac{K_bT}{e}\ln\left(\frac{A_r A^* T^2}{I_0}\right)$$ (4.24)

and is strongly influenced by the deposition method of the metal used in fabricating the Schottky contact. This parameter is evaluated in practice by substituting a value of saturation current in equation (4.24).

The ideality factor η of a diode is a measure of the departure from ideal behaviour and it ranges between 1 and 2 depending on the dominant current mechanism [36]. In practice, the parameter is determined from the slope of the linear region of the plot of natural log of forward current bias voltage and is given as:

$$\eta = \frac{K_bT}{e}\left(\frac{dV_0}{\ln I}\right)$$ (4.25)

η =1 when the diffusion current dominates. Nevertheless, ideality factor usually has a value greater than unity. There are many factors that can make the parameter to be greater than unit. These include the presence of an interface layer between the metal and the silicon [48], the temperature of operation of the diode and the generation or combination of charge carriers in the material [37].

4.5.2 Capacitance-voltage

Capacitance-Voltage (C-V) technique in reverse bias has been widely employed to determine the doping profiles in semiconductor [38] such that the measurement of the capacitance give information about fixed impurity states and defect centres in the band gap [25]. This capacitance is associated with the bending of energy bands in the junction [39], and this determined by the net ionised charge density. The junction capacitance can be extracted in the depletion region and it is expressed [40] as:

$$C = A_r \sqrt{\frac{e \varepsilon_s \varepsilon_0 N_D}{2(V_d + V_0)}} \tag{4.26}$$

where C is the capacitance in the depletion region, A_r is the active area of the diode, ε_s is the permittivity of the semiconductor, ε_0 the vacuum permittivity $\left(\varepsilon_0 = 8.85 \times 10^{-12} \frac{F}{m}\right)$, N_D is the doping density of the donor atoms, V_d is the diffusion potential at zero bias, which is determined from the extrapolation of the linear C^{-2}-V plot to the voltage axis and V_0 is the intercept of C^{-2} with the voltage axis. The above equation can be re-arranged as:

$$C^{-2} = \frac{2}{A_r^2} \left(\frac{V_d + V_0}{e \varepsilon_s \varepsilon_0 N_D} \right) \tag{4.27}$$

which can be expanded to be to show that the doping density is determined from the slope of the linear region of a C^{-2} against v graph to show that the doping density is determined from the slope of the linear region of a C^{-2} against v graph as:

$$C^{-2} = \frac{2}{A_r^2} \times \frac{V_d}{eq\varepsilon_0 N_D} + \frac{2}{A_r^2} \times \frac{V_0}{e\varepsilon_s\varepsilon_0 N_D} \tag{4.28}$$

It can be noted that V_0 can be determined from the above equation by using the interception the C^{-2} axis. The obtained values of N_D and V_d are then used to determine the Schottky barrier height [50] as:

$$\Phi_B^{C-V} = V_d + E_F - \Delta\Phi_B \tag{4.29}$$

where the Fermi energy (E_F) can be expressed as:

$$E_F = \frac{K_b T}{q} \ln\left(\frac{N_{vb}}{N_D}\right) \tag{4.30}$$

References

[1]   Rubin S , Passell T O and Bailey L E, 1957 *Anal. Chem*. **29** 736.

[2]   Mayer J W, Nicolet M A and Chu W K,   1975 *Journal of Vacuum Science and Technology* **12** 356.

[3]   Hashimoto H *et al.,* 2010 *Surface Science* **604** 464.

[4]   Ziegler J F, 2013 *SRIM, Http//www. Srim. Org.*

[5]   Rimini J W M E, 1977 *Ion Beam Handbook for Material Analysis (*Academic Press:New   York) 1st ed.

[6]   Feldman L C and Mayer J W, 1982 *Materials Analysis by Ion Channeling* (Academic Press:NewYork) 1st ed.

[7]   Chu W K, Mayer J W and Nicolet M, 1978 *Backscattering Spectrometry (*Academic   Press: New York) 1st ed.

[8]   Tesmer J R *et al*. eds., 1995   *Handbook of Modern Ion Beam Materials Analysis,* Materials Research Society: Pennsylvania, 1st ed.

[9]   Ziegler J F and Iafrate G J, 1980 *Radiat. Eff*. **46** 199.

[10]   Odutemowo O S, 2016. *Investigating Effect of Fission Products Bombardment on Glassy Carbon* (PhD Thesis: University of Pretoria).

[11]   Thabethe T T, 2017 *The interfacial reaction and analysis of W thin film on 6H-SiC annealed in vacuum, hydrogen and argon* (PhD Thesis: University of Pretoria).

[12]   Knoll G F, 2010 *Radiation Detection and Measurement* (Wiley:NewYork) 4th ed.

[13]   Lindhard J and Scharff M ,1961 *Phys. Rev*. **124** 128.

[14]   Williams J S, 1998 *Mater. Sci. Eng. A* **253** 8.

[15]   Patel N H, 2015 *Basic Principle, Working and Instrumentation of Experimental Techniques.* Sardar Patel University:Gujarat.

[16]   Kasap S O, 2006 *Principles of Electronic Materials and Devices* (McGraw-Hill:New York) 3rd ed.

[17]   Friedrich W, Knipping P and von Laue M, 1913 *Ann. Der Phys.* **41** 971.

[18]   Kittel C and McEuen P, 2004 *Introduction to Solid State Physics* (Wiley:NewYork) 8th ed.

[19]   Ashcroft N W and Mermin N D, 1976 *Solid State Physics (*Brooks Cole:Pacific Grove*)*

1st ed.

[20] Kittel C, 1976 *Introduction to Solid State Physics* (Wiley: NewYork) 7th ed.

[21] Streetman B G *et al.*, 1995 *Solid State Electronic Devices* (Prentice Hall: New Jersey) 5th ed.

[22] Girgsdies F, 2015 *Peak Profile Analysis in X-ray Powder Diffraction,* Fritz-Haber-Institut Der MPG Berlin, Germany.

[23] Yu P Y and Cardona M, 1999 *Fundamentals of Semiconductors: Physics and Material Properties* (Springer: New Jersey) 3rd ed.

[24] Rhoderick E H and Williams R H, 1988 *Metal-semiconductor contacts* (Oxford: Clarendon) 2nd ed.

[25] Pierret R F, 1996 *Semiconductor Device Fundamentals* (Pearson Education:India) 2nd ed.

[26] Nuhoğlu Ç *et al.,* 1998 *Appl. Surf. Sci.* **135** 350.

[27] Wilmsen C W, 1985 *Physics and Chemistry of III-V Compound Semiconductor Interfaces* (Plenum:London) 1st ed.

[28] Hanselaer P L *et al.,* 1986 *J. Appl. Phys.* **56** 2309.

[29] Colinge J-P and Colinge C A, 2005 *Physics of Semiconductor Devices* (Springer-Verlag: New York) 1st ed.

[30] Moloi S J and McPherson M, 2019 *Nuclear Inst. and Meth. B* **440** 64.

[31] Werner J H and Güttler H H, 1993 *J. Appl. Phys.* **73** 1315.

[32] Wagner L F, Young R W and Sugerman A, 1983 *IEEE Electron Device Lett*. **4** 320.

[33] Karataş Ş and Türüt A, 2006. *Nucl. Instr. and Meth. A* **566** 584.

[34] Moloi S J and McPherson M, 2013 *Radiat. Phys. Chem.* **85** 73.

[35] Çetin H, Şahin B, Ayyildiz E and Türüt A , 2005 *Phys. B Condens. Matter.* **364** 133.

[36] Moloi S J and Mcpherson M, 2009 *Phys. B.* **404** 2251.

[37] Hudait M K and Krupanidhi S B, 2001 *Physica B* **307** 125.

[38] Senechal R R and Basinski J, 1968 *J. Appl. Phys.* **39** 4581.

[39] Schroder D K, 2006 *Material And Device Semiconductor* (Wiley:NewYork) 3rd ed.

[40] Bleicher M and Lange E, 1973 *Solid. State. Electron.* **16** 375.

Chapter 5

Experimental details

This chapter describes procedures followed to prepare and characterize samples in this work. These samples are silicon wafers that were doped with erbium and undoped and erbium-doped silicon-based diodes. Doping was achieved by ion implantation. *XRD* and *RBS* techniques were used for material characterisation while *I-V* and *C-V* techniques were used for diode characterisation. The measurements were carried out at room temperature.

5.1 Sample preparation

Material used in this work is a crystalline silicon wafer with different concentration types (*p*-, *i*- and *n*-type). The material was acquired from Semiconductor Wafer, Inc with one side polished. The resistivities of *p*- and *n*-type material were quoted as 1~20 ohm-cm and as 500 ohm-cm for *i*-type material. The thickness and orientation of all wafers were quoted as 275 ± 25 μm and <111>, respectively.

The wafers were diced into ~ 0.5×0.5 cm^2 using a diamond tip cutter. Prior implantation, the pieces were the cleaned using standard procedure of cleaning silicon samples [1-4]. Samples were dipped for 5 minutes in warm trichloroethylene, acetone, and methanol in an ultrasonic bath to remove dirt, grease and undesirable impurities, respectively. The pieces were then rinsed in warm deionized water. Thereafter, they were dipped in HF solution to remove native oxides from the surface material which was later followed by rinsing in deionised water to remove HF remnants. The pieces were then blown-dried with high purity nitrogen and mounted in a target chamber for erbium implantation.

Erbium ions of 160 keV was implanted into the front (or polished) side of silicon pieces to a fluence of ~1 x 10^{16} at.cm^{-2} and at the energy of 60 keV for the fluence of ~1 x 10^{15} at.cm^{-2}

and ~1 x 10^{16} at.cm^{-2}. A low energy fluence was used in order to restrict the implanted atoms to the near surface so that the diffusion mechanisms of the metal can be investigated using techniques that are currently available. For 160 keV implantation, the Varian-Extrion 200-20A2F ion implanter based at iThemba LABS (Gauteng) South Africa was used while Ion Implanter facilities at GNS Science, Wellington, New Zealand was used for 60 keV implantation. For all energies, the implantation process was carried out in high vacuum (~2 x 10^{-7} mbar) at room temperature.

Some of the samples implanted with erbium ions of 60 keV were annealed using Electron Beam (EB) annealing system [5] set up at GNS Science, Wellington, New Zealand. The samples were annealed in the vacuum (~2 x 10^{-7} mbar) at 800 ^{0}C and 1000 ^{0}C. These annealing temperatures were chosen since they are 100 ^{0}C before and after, respectively, erbium maximum solubility in silicon. At 900^{0}C erbium reaches the maximum solubility of 10^{18} cm^{-3} beyond which the platelets of ErSi begin to form in silicon [6-9]. At annealing temperature less than 800 ^{0}C erbium profile in silicon does not change [10-11].   The annealing was done for 30 minutes, the time that was found suitable for annealing at the temperature ranging from 800 ^{0}C to 1000 ^{0}C [6;10-11]. The system operates with an energy EB of 20 keV and current up to 4 mA.

Prior to the implantation; Transport of Ions into Matter (TRIM) simulations were used to predict the distribution of erbium in silicon for 160 and 60 keV energies. A theoretical profile of ion implanted at an energy of 160 keV shown in figure 5.1 (a) predicts a projected range of 65.9 nm with a maximum implantation depth of around 120 nm. Figure 5.1(b) confirms that the damage due to erbium implantation is up to the depth of 120 nm. This damage is due to collision of erbium as it collides with silicon atoms. Due to this collision the host atoms are being displaced resulting into the creation of vacancies. As it penetrates

the silicon, erbium loses it energy due to atomic nuclear and electron cloud interactions. Figure 5.1 (c) shows that the calculated nuclear energy loss and electronic energy loss as 92.0 % and 62.8 %, respectively. This calculation indicates that the nuclear part is the dominant mechanism of the energy loss per unit length in silicon. As shown in figure 5.1(d) the collisions in silicon results into the displacement and vacancies collisions.
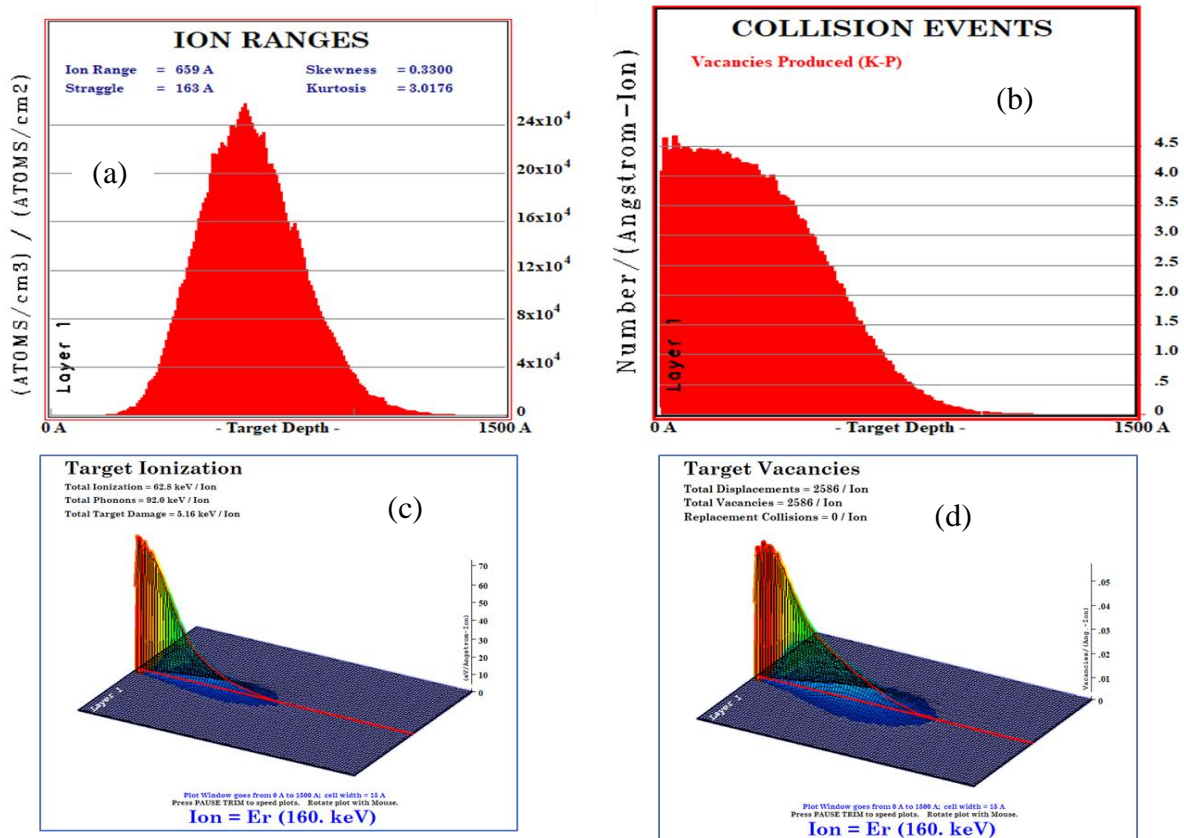
Figure 5.1: *2-D TRIM-2013 simulation showing, depth (a) and vacancy distributions and 3-D TRIM 2013 simulation showing mode of energy loss (c) and total displacement, vacancies and replacement collisions (d) for erbium ions implanted in silicon at 160 keV.*

TRIM simulation was also carried out for the ion implanted at low energy of 60 keV. The calculated results are shown in figure 5.2. It can be seen from figure 5.2 (a) that the theoretical profile predicts a projected range of 33.8 nm with a maximum implantation depth of around 58.8 nm. Figure 5.2 (b) shows that damage due to erbium collision with silicon atoms at this energy (60 keV) is up to the depth of 58.0 nm. Figure 5.1 (c) shows that the calculated nuclear energy loss and electronic energy loss as 37.7 % and 20.2 %, respectively indicating that the nuclear part is the dominant mechanism of the energy loss per unit length

in silicon. As shown in the case of 160 keV energy implantation the results shown in figure 5.2 (d) shows that the total collision still results into the displacement and vacancies collisions.
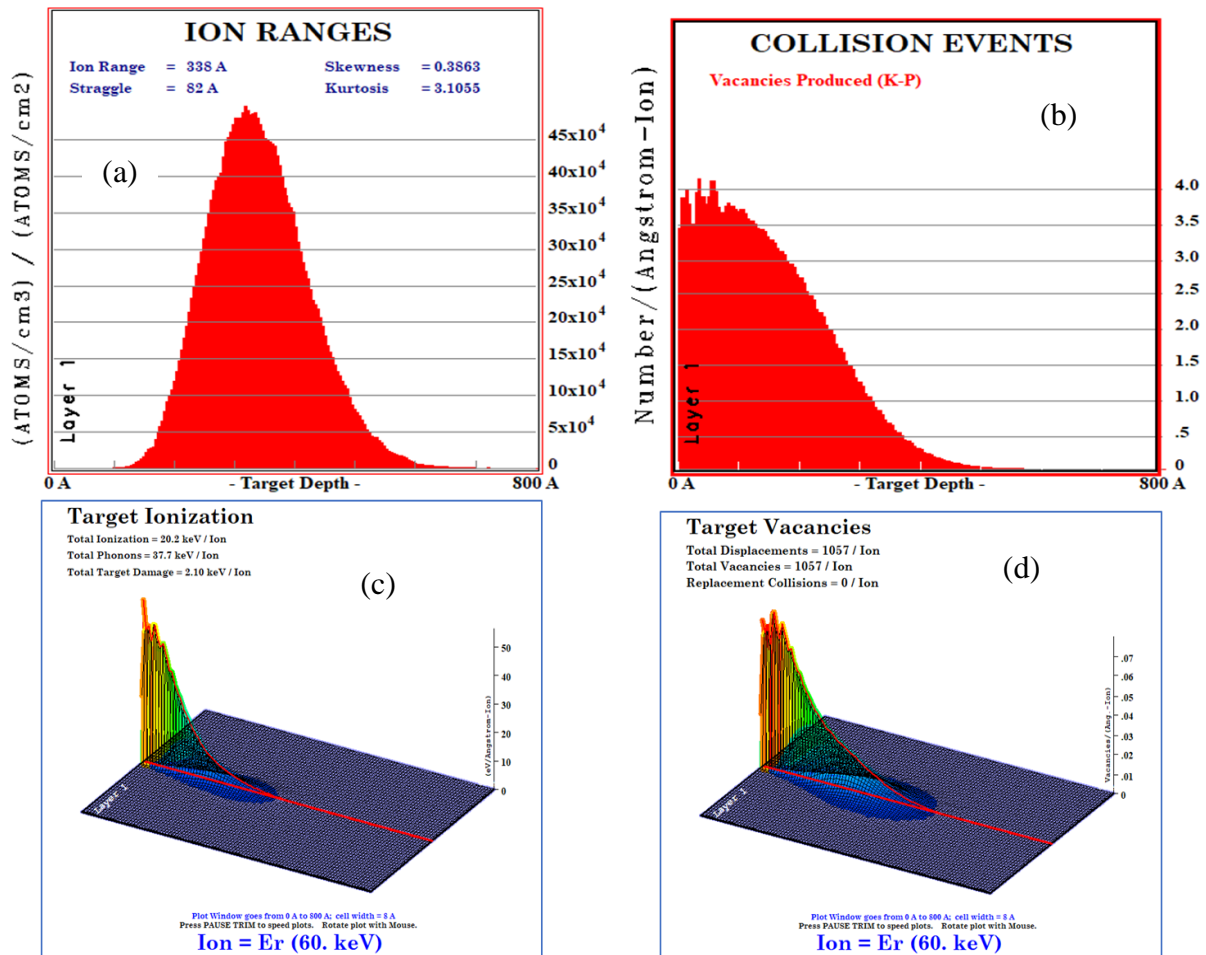
Figure 5.2*: 2-D TRIM-2013 simulation showing, depth (a) and vacancy distributions and 3-D TRIM 2013 simulation showing mode of energy loss (c) and total displacement, vacancies and replacement collisions (d) for erbium ions implanted in silicon at 60 keV.*

Figure 5.3 shows that the low implant energy produces more damage and that the damage lies closer to the substrate surface.   This implies that the induced defects lie closer to the sample surface. The results also show that the higher implant energy lead to a broader and deeper vacancy distribution (damage), indicating the defects have been induced deep in silicon. Since the main objective of this work is to establish and investigate a change in electrical properties of the diodes due to erbium induced defects in silicon, devices were fabricated on

the material that was implanted at 160 keV. This is the highest implantation energy that could be achieved using the available facilities.
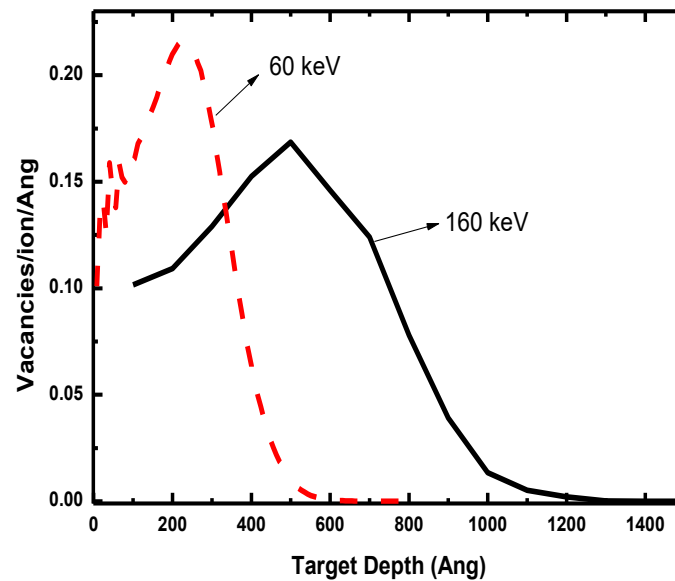
Figure 5.3: *SRIM-2013 simulation for the number of vacancies per ion and unit length (Å) versus depth for erbium ion implanted silicon at 60 and 160 keV.*

5.2 Material Characterization

Prior to device fabrication, unimplanted and erbium implanted *n*-silicon were characterised using *RBS* and *XRD* techniques. These techniques were used in this work to establish the presence of erbium and its diffusion mechanisms in silicon.

5.2.1 Rutherford backscattering spectrometry/ channelling measurements

The measurement set up consists of a He$^+$ ion source, a beam accelerator and steering system, a target chamber, signal processing electronics and the data acquisition system. Samples are fixed onto a sample holder, which is a ladder that is tilted at an angle of 10^0 to the incident ion beam measured from the normal to the ladder. Measurements were carried out at ~10^{-7} mbar using 2.0 MeV He$^+$ beam with a 15 nA current and collimated to 1 mm in diameter. The backscattered ions were detected by a silicon detector positioned at a scattering angle of 165^0 to the incident beam to detect the backscattered particles. Each sample was measured at multiple spots to check the uniformity of implantation.

Figure 5.4 shows a sample result in random and channelling modes, where the heights of the peaks represent the concentrations, while the peak widths are related to the layer thicknesses of the elements. Peaks of erbium and silicon are shown in the figure. The trends are presented as yield as a function of channel number. Also in the figure the (black) line denotes random spectrum and the (red) line denotes channelling spectrum.
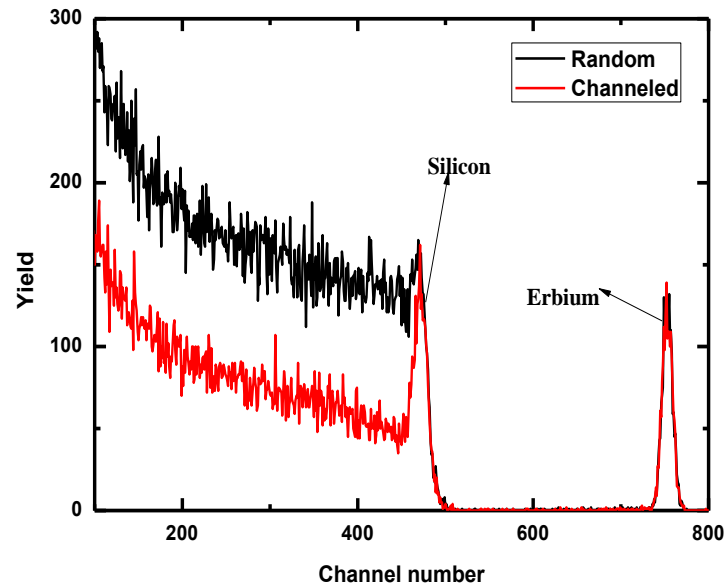
Figure 5.4: *RBS spectra for sample implanted to the fluence of* 1×10^{16} *ion/cm²*.

5.2.2 X-Ray diffraction measurements

In this work a crystal structural change of erbium-doped silicon prior to and after annealing at temperatures, 800 ^{0}C and 1000 ^{0}C, for 30 minutes were investigated using *XRD* technique using Smart Lab X-Ray Diffractometer with Cu-Kα radiation (λ = 1.54 Å) supplied by Rigaku. The data acquired was used to generate the plot shown in figure 5.5. In this plot, the intensity of diffracted X-rays is plotted as a function of diffraction angle (or peak position at 2θ).
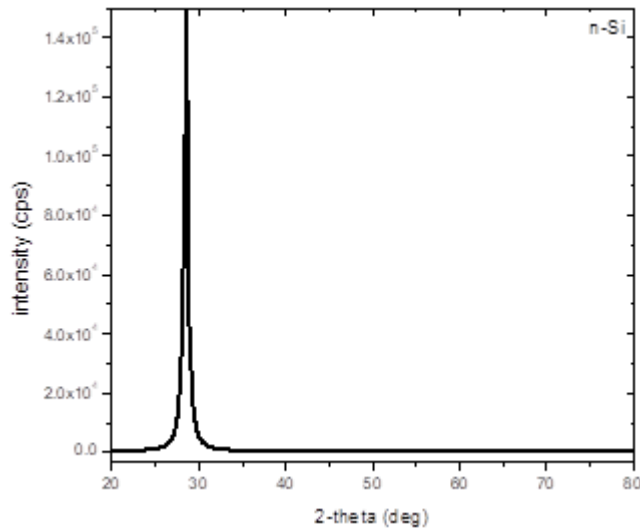
Figure 5.5: *XRD pattern of unimplanted n-silicon.*

5.3 Device fabrication

Devices in this study are diodes fabricated on undoped and metal doped silicon. A vacuum resistive evaporation setup based at the University of Pretoria; South Africa was used for fabrication of the devices. Prior to device fabrication process silicon pieces were chemically cleaned using the same procedure as explained in Section 5.1. Similar procedure followed by Ref. [12] to fabricate devices was adopted in this work. The Schottky contacts were achieved by vacuum ($\sim 10^{-6}$ mbar) evaporation and deposition of 100 nm palladium through a mask with 0.6 mm diameter holes. A deposition rate was measured as 1Å/s. An ohmic contact, on the other hand, was realised by rubbing indium gallanide (InGa) on the back surface of the pieces.

## 5.4 Device characterization

The fabricated devices were characterized by current-voltage (*I-V*) and capacitance- voltage (*C-V*) techniques. In the former technique the voltage was varied while the current through the diodes was closely monitored, while in the latter technique the capacitance was measured as the voltage was varied.

The *I-V* data were acquired remotely using the ExceLINX package, after which they were stored as ASSCI files and then imported into ORIGIN for analysis. The *C-V* data, on the other hand, were acquired using MATLAB and entered directly into ORIGIN for graphing and analysis.

5.4.1 Current-voltage measurements

The measurements were carried out at room temperature with the samples placed in the dark. These measurements were carried out on each sample using a Keithley 6487 picoammeter with a voltage source. The instrument was operated in the remote (REM) mode by connecting it to a personal computer (PC) through an RS-232 cable. An add-in utility for Microsoft Excel was installed in the PC for control of the picoammeter and for data acquisition.
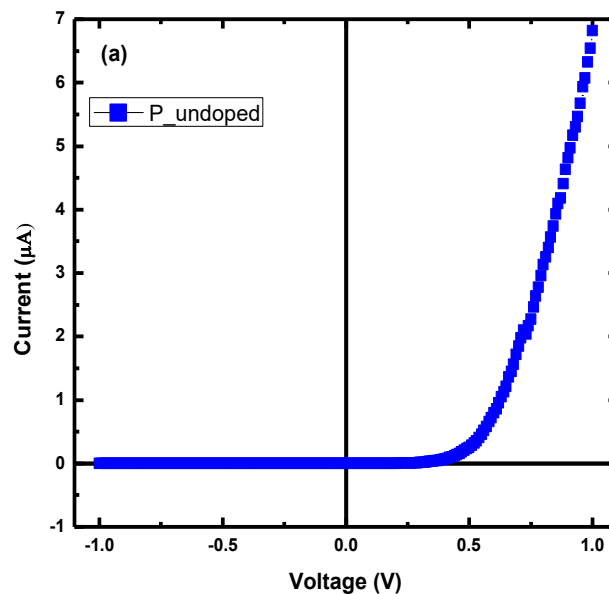
Figure 5.6: *Current-voltage characteristics of the diodes fabricated on undoped p-silicon in linear-linear scale.*

Figure 5.6 shows a typical *I-V* characteristic of the unimplanted silicon-based diode. The data are presented in linear-linear scale in order to indicate the quality of the diode. The data will also be presented in log-log scale to clarify whether the devices are fabricated on lifetime or on relaxation material. The analysis is also based on the forward ln (*I*) versus *V* graph.

The slope obtained from the linear region of ln (I) versus V graph is used to determine important parameters such as the ideality factor, the saturation current and the Schottky barrier height.

5.4.2 Capacitance-voltage measurements

C-V measurements in reverse bias were carried out using an Agilent 4263B LCR meter. The data were acquired using and external voltage supplied by Keithley 6487 picoammeter. Computer MATLAB commands were placed on M-File to acquire the C-V data. The commands were written such that Agilent 4263B LCR meter measures the capacitance while Keithley 6487 picoammeter only supply the voltage. The measurements were carried out at 10 kHz.
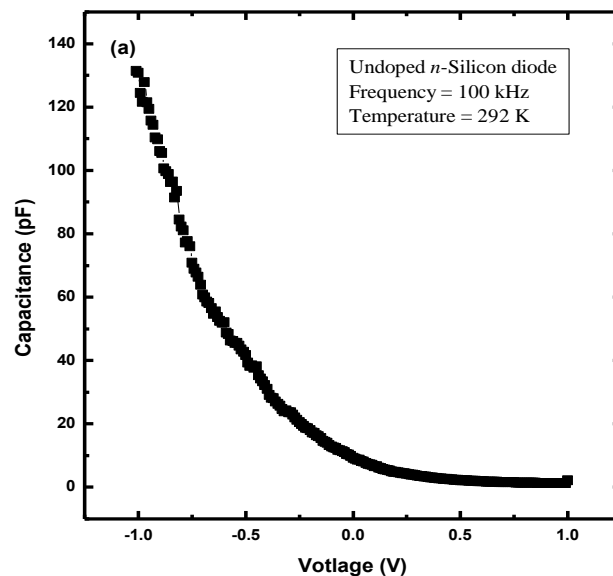
Figure 5.7: *Capacitance-voltage characteristics of diodes fabricated on undoped n-silicon measured at 292 K and at 100 kHz.*

Figure 5.7 shows a typical C-V characteristic of Schottky diodes. Another method of analysis is based on the plot of C^{-2} against reverse bias. This type of analysis is used to investigate the doping density within the material. The linear region of the plot shows that the doping profile within the material is uniform and the doping density can be evaluated.

69

References

[1]   Hanselaer P L *et al*., 1986 *Appl. Phys. A* **39** 129.

[2]   Chand S and Kumar J, 1996 *Appl. Phys. A* **63** 171.

[3]   Moloi S J and McPherson M, 2009 *Physica B* **404** 2251.

[4]   Surucu O B *et al.*, 2019 *Physica B* **246** 2251.

[5]   Kennedy J *et al*., 2010 *J. Appl. Phys.* **107** 103518.

[6]   Eaglesham D J *et al.*, 1991 *Appl. Phys. Lett*. **58** 2797.

[7]   Benton J L *et al*., 1991 *J. Appl. Phys*. **70** 2667.

[8]   Polman A *et al*., 1993 *Appl. Phys. Lett*. **62** 507.

[9]   Masterov V F *et al*., 1998 *Semiconductors* **32** 636.

[10]   van den Hoven G N, Shin J H and Polman A, 1995 *J. Appl. Phys.* **78** 2642.

[11]   Tang Y S *et al*., 1989 *Solid State Communications* **72** 991.

[12]   Thebe M J, 2015 *Bulk Characterisation of Niobium-Doped Silicon Diodes* (*MSc Dissertation*: University of South Africa).

Chapter 6

Results and discussions

This chapter presents the results obtained from the measurements carried out on the silicon and the diodes fabricated on it. The chapter consists of two sections. The first section presents the results obtained from the *RBS* and *XRD* measurements while the results obtained from the electrical characterization of the Schottky diodes fabricated on the undoped and erbium-doped silicon are discussed in the last section.

6.1 Material characterisation

Discussions on the results obtained from the *RBS* and *XRD* measurements are mainly based on the comparison of the erbium implanted samples prior to and after the annealing process. The *RBS* measurements were carried out on the samples immediately after the deposition and the annealing processes while the *XRD* measurements were carried out three months after the processes. Hence, contaminations are expected to form on the surface of silicon since the samples were stored in an atmospheric pressure. It has to be noted that, silicon can be oxidised and the thickens of oxygen later increases with time of exposure [1].

6.1.1 *RBS-C* results

Rutherford backscattering spectrometry channelling (*RBS/C*) measurements were carried out on unimplanted *n*-silicon in order to establish the feasibility of our set up to characterise Si <111>. Figure 6.1 shows *RBS* channelling spectra of undoped silicon. The upper curve (black) is the random spectrum and the lower curve (red) is the channelled (aligned) spectrum. The random spectrum shows a typical trend of crystalline silicon. As expected, there is no surface peak in the aligned spectrum to show that the surface region of silicon is not damaged. The channelling yield of the random is 2.9 % that of the random yield. This

low channelling minimum yield (χ_{min}) indicates a good crystalline quality of silicon and it is comparable to 3 % [1] and 5 % [2] reported before. χ_{min} is a parameter that is used to indicate the overall level of crystalline defects in lattice and is a ratio of the random and aligned yields [3]. As a result, a complete amorphous material has a χ_{min} of 100 % whereas, a perfectly single crystal has χ_{min} of ~1 -2 % [4]. Based on these results, it was safely concluded that the *RBS* set up was suitable for characterisation of our samples.
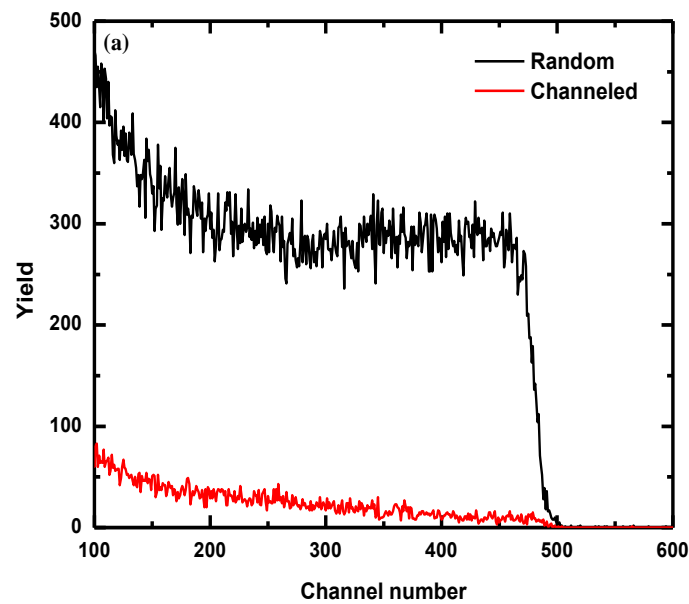
Figure 6.1*: RBS spectra for unimplanted in random and channelling modes.*

Figure 6.2 (a) shows the random and aligned spectra for silicon implanted with erbium ions of 60 keV to the fluence of 10^{15} ion/cm^2 prior to thermal annealing. The channelling spectra shows the surface peak on the silicon edge. This peak indicates that the crystal has been damaged in the surface region [3]. The extent of the damage is determined by the height of the peak and the depth of the damage is determined by width of the peak [5]. Comparing the channelled and the random spectra, it can be observed that the peaks do not overlap which indicates that the implantation of 1×10^{15} ion/cm^2 Er$^+$ in silicon does not result in complete amorphisation of the Si substrate. The random yield is about 57 % of the channelled yield which implies that there are several Si crystals still present in the Si structure even after Er implantation. Figure 6.2 (a) shows identical erbium peaks from random and aligned spectra

indicating that erbium is not a substitutional but interstitial impurity in crystalline silicon. This finding agrees with the work presented by Wahl [6] and with theoretical calculations presented by Refs. [7-9]. Though, the work presented by Refs [1, 10] show the random and aligned spectra were identical, it was not concluded that in silicon, erbium occupies interstitial sites.
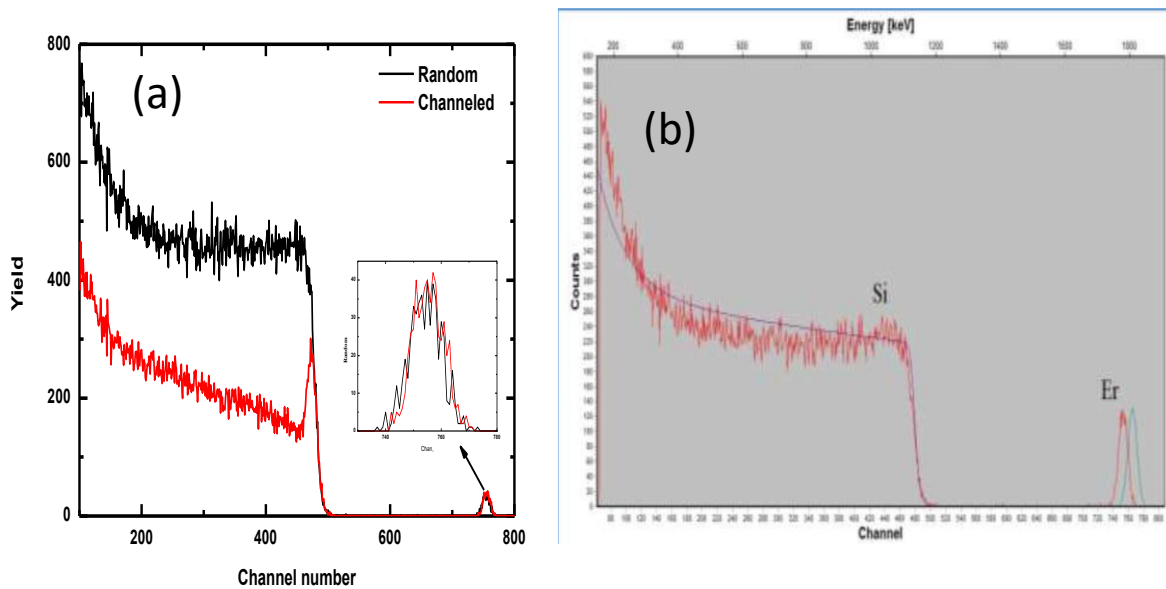
Figure 6.2: *RBS spectra for erbium-implanted prior to annealing process. Experimental data in random and channelling modes (a) and the RUMP simulated data (b).*

The computer program, Rutherford Universal Manipulation Program (RUMP), was used to analyse the *RBS* spectra [11] and to determine erbium penetration depth and thickness in silicon. The program enables a comparison of the simulated and the experimental spectra. The data presented was obtained from the fitting using SIMNRA. Figure 6.2 (b) shows the comparison of experimental channelling spectrum and RUMP simulated data. The simulated *RBS* spectrum fits well for the silicon peak, however, this is not the case for erbium peak. The experimental erbium peak is seen to have shifted to the left-hand side from the theoretical peak. The shift is because SIMNRA assumes that energies of backscattered helium particles are due to erbium on silicon surface. This is however, in this experiment, not the case. The erbium implants are embedded in silicon substrate, meaning that the energy of the ion beam

incident on the erbium implants is not the initial 2 MeV. Energy is lost as the ion beam collides with silicon atoms prior to contact with erbium in silicon. The kinematics, therefore, result in the shift. The shift thus, attests an existence of erbium in and at a certain depth from the surface of silicon.

The erbium penetration depth can be explained in terms of stopping power, $S(E)$, [10; 12] as:

$$\Delta t = \frac{E_{\text{surf}} - E_{\text{charact}}}{S(E)} \qquad (6.1)$$

where E_{surf} is the backscattered energy on the surface due to erbium and E_{charact} is the measured backscattered energy of erbium in silicon.

In determining erbium thicknesses in silicon using SIMNRA through simulation, the simulated erbium peak was shifted to left hand through the manipulation of the calibration offset value. The shifting was done in order to have the simulated peak fit over the experimental peak in compensation of the energy shifts. A fit of the simulated peak over the experimental peak was done and the thickness value was obtained in units of atoms/cm^2 with a multiplication factor of 1×10^{15}. Stoichiometric concentration values were also obtained and thus inputted in SRIM to determine the atomic density (atoms/cm^3). The final thickness unit conversion was done by dividing the obtained thickness by the atomic density to give the thickness in units of cm. The penetration depth and the thickness of erbium implanted in silicon at 60 keV were found to be 125.63 and 38.83 nm, respectively. The evaluated penetration depth (125.63) is higher than the estimated using TRIM simulation (33.8 nm). This discrepancy is as a result of TRIM simulation routine lacks any consideration of the fluence dependent evolution of silicon [13].

RBS measurements were also carried out on erbium doped silicon after annealing at 800 ºC and 1000 ºC for 30 min. The silicon surface damage peak for aligned spectrum shown in

figure 6.3 (a) is lower than the one observed in figure 6.2 (a). It can also be seen from figure 6.3 (a) that, in general, the yield of silicon random spectrum has decreased. This reduction of the damage peak indicates that annealing at 800 ^{o}C for 30 minutes significantly reduces silicon crystal damage induced by erbium implantation. The reduction of the yield for random spectrum, on the other hand, indicates that the crystallites have formed after the annealing process [5]. The channelling yield was evaluated to be ~ 8.0 % that of the random yield indicating that, though not fully re-crystalline, the damage on silicon has been recovered upon thermal annealing in vacuum. A slight shifting of the surface damage peak to a lower channel than the surface edge of the random spectrum in figure 6.3 (a) indicates that there is a thin region of crystalline silicon on the surface [5].
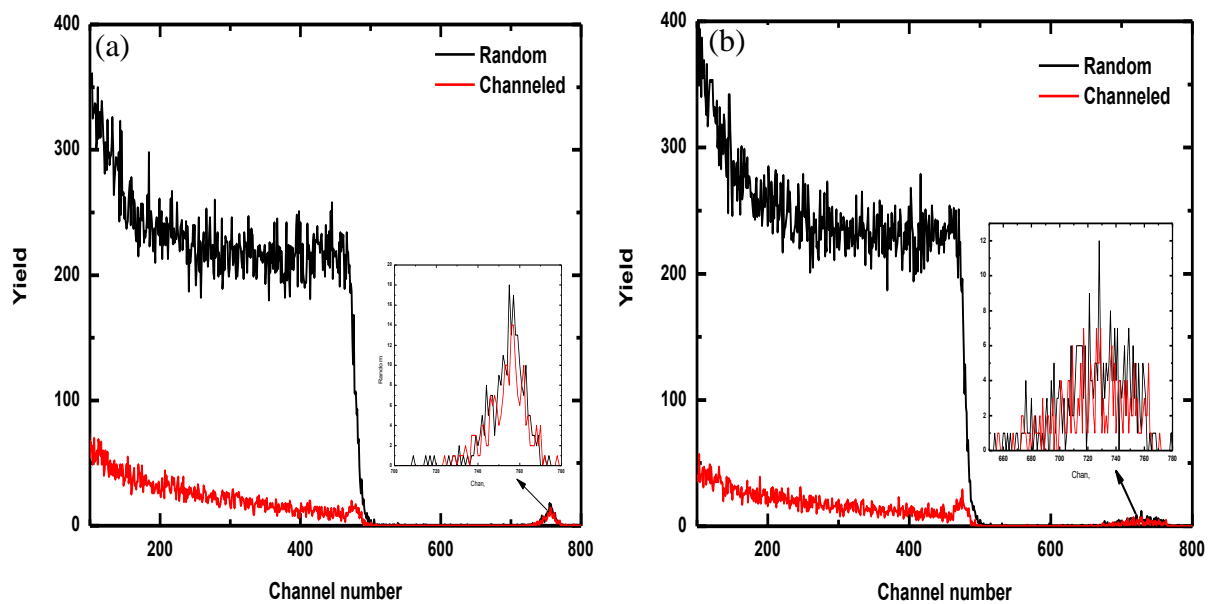
Figure 6.3: *RBS spectra for erbium implanted silicon annealed at (a) 800 ^{o}C and (b) 1000 ^{o}C in random and channelling modes. Both silicon and erbium signals are displayed.*

In figure 6.3 (a), the erbium peaks produced from random and aligned spectra are almost identical with a channelling yield of ~ 86.0 % indicating that erbium is mostly at interstitial position in crystalline silicon. Comparing inserts of figures 6.2 (a) and 6.3 (a), it can be noticed that the height of erbium peak has decreased from yield 40 to yield 18 upon annealing. Another observation from the inserts is that the erbium peak width has increased

75

and sloped at a lower channel indicating that a metal-silicide layer has been formed when erbium diffused into silicon during the annealing process [14-15].

The same procedure followed to calculate the penetration depth and the thickness for as implanted samples was adopted for samples that were annealed at 800 $^{\circ}$C and were found to be 128.19 and 40.73 nm, respectively. These results further indicate that erbium has diffused slightly in silicon after the annealing process.

Figure 6.3 (b) show *RBS* spectrum of erbium implanted silicon annealed at 1000 ^{0}C with the silicon surface damage peak for aligned spectrum lower than the one in figure 6.2 (a). The yield of silicon random spectrum is similar to that of figure 6.3 (a) but still lower than that of figure 6.2 (a). As explained before, the reduction of the damage peak indicates that annealing at 1000 ^{0}C for 30 minutes has reduced silicon crystal damage induced by erbium implantation. The spectrum still indicates the reduction of the yield for random spectrum showing that the crystallites have formed after the annealing process.

The channelling minimum yield for the sample annealed at 1000 ^{0}C for 30 minutes was evaluated to be ~ 10.0 % indicating that the damage on silicon has been recovered upon vacuum annealing. It was, however, expected that the channelling yield of the sample annealed at 1000 ^{0}C would be lower than the one annealed at 800 ^{0}C since the damage recovery was expected to increase with annealing temperature. A possible reason of this discrepancy is explained later in the text. The spectrum still shows a slight shift of the surface damage peak to a lower channel indicating a thin region of crystalline silicon on the surface. Similar to the one in figure 6.3 (a), an inset of figure 6. 3 (b) shows that the height of erbium peak has decreased as the width increases. It was noticed that at the lower edge the height start sloping indicating that a metal-silicide layer has been formed when erbium diffused into

silicon during the annealing process. The channelling minimum yield for erbium was evaluated to be ~ 91.0 % indicating that erbium is mostly at interstitial position in crystalline silicon.

The penetration depth and the thickness for this sample were evaluated to be 0.37 and 342.43 nm, respectively. Based on the evaluated penetration depth, it can be noticed that erbium has diffused back toward the surface of silicon. It was expected to be deeper, at the depth higher than (128.19) the one for a sample annealed at 800 ^{0}C. In general, the solid solubility increases with temperature. An observed "back diffusion" indicates that this general definition of solubility does not apply in the case of this sample. This discrepancy could be due to a solubility limit of erbium in silicon. Erbium reaches its solubility limit of ~10^{18} cm^{-3} at 900 ^{0}C [2; 16-17]. The limit occurs since at the temperature higher than 900 ^{0}C the hydrogen diffuses out of the material resulting in high number of free oxygen previously bonded to hydrogen [18]. As a result of this, the material will have Er-O cluster leading into a highly defective material [18]. This cluster of Er-O could be the reason of an increase in channelling minimum yield evaluated for sample annealed at 1000 ^{0}C, hence a decrease in crystallinity of silicon.

It has also been observed that that at the temperature higher than 900 ^{0}C, at which erbium possesses solubility limit, platelets of ErSi begin to form resulting in an erbium segregation as temperature increases [16]. A back diffusion observed for sample annealed at 1000 ^{0}C could be a result of erbium segregation in silicon.

Figure 6.4 shows a variation of channelling yields with annealing temperature. Though number of points is insufficient, the trends are clear enough to summarise a change in material crystallinity with defect induced in the material. Figure 6.4 (a) shows that the channelling yield of as implanted is high indicating a low material crystallinity. Due to

thermal annealing, the damage in silicon is recovered resulting in a decrease in the channelling yield (increase in material crystallinity). As the annealing temperature increases, the material becomes highly defective due to the high number of free oxygen initially bounded to hydrogen. This results in an increase in the channelling yield (decease in material crystallinity).
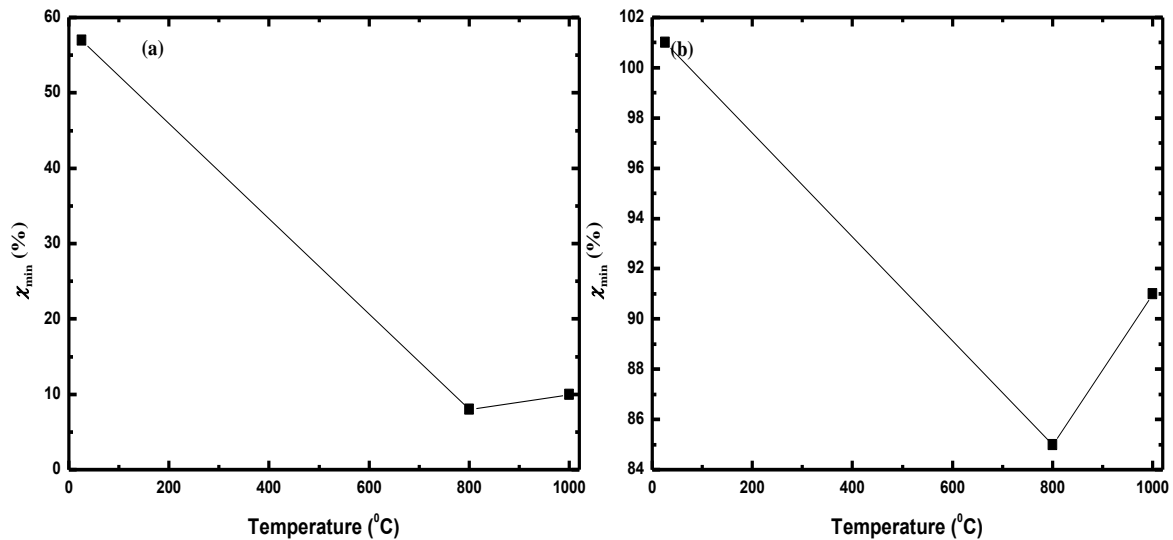
Figure 6.4: χ_{min} *versus annealing temperature for both silicon (a) and erbium (b) peaks. The lines are drawn to guide the eye.*

Figure 6.6 (b), on the other hand, shows erbium channelling yield of 100 % for as implanted sample. This high yield indicates that in silicon erbium occupies interstitial site. This finding is in good agreement with the experimental [6] and theoretical data [7-9] presented before. A decrease in χ_{min} from 100 % to 86 % indicates that less than 20 % of erbium diffuses to substitutional site at annealing temperature of 800 ^{0}C. The obtained diffusion mechanism may seem to contradict the one presented in ref [19] indicating that at 900 ^{0}C most erbium (80%) is at substitutional site. A reason for this difference could be due to the annealing temperatures. The work presented here reports on the annealing temperature of 800 ^{0}C while that presented in ref [18] reports on the annealing at 900 ^{0}C. There are possibilities of having more that 20 % of erbium diffusing from interstitial to substitutional site at annealing temperature of 900 ^{0}C.

A trend in figure 6.4 (b) shows that χ_{min} increases with further increase in temperature indicating that the amount of erbium atom occupying substitutional site has decreased. This decrease is due to high concentration of oxygen forming Er-O cluster defects in silicon. Thus, the substitutional site occupied by erbium is unstable due to oxygen. This instability of the substitutional due to oxygen was explained before and it was reported that oxygen changes the site occupied by erbium from substitutional to interstitial [20]. The results presented in this work would assist to address a long outstanding confusion about diffusion mechanisms of erbium in crystalline.
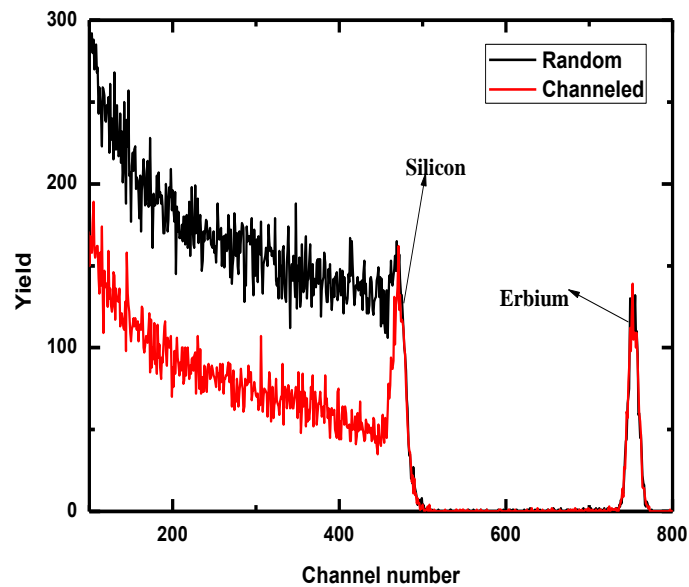
Figure 6.5: *RBS spectra for sample implanted to the fluence of* 1×10^{16} *ion/cm^2.*

The *RBS* data presented here indicates that annealing the samples results in a surface damage recovery of silicon with a certain amount of erbium diffusing from interstitial to substitutional silicon sites. However, as the annealing temperature further increases some of the erbium atom initially diffused through substitutional diffused back through silicon interstitial site. It is therefore important that erbium is implanted at high energy to high fluence in order to study the effects of erbium solely on bulk electrical properties of the

material. A high energy and fluence would result into the damage occurring deep with considerable amount of erbium in silicon crystal.

Figure 6.5 shows that more damage occurs when implanting to the high fluence. It can be seen from the figure that the surface damage peak shows a completely amorphous region for the full path of length of the implanted erbium. The figure also shows that the erbium peak is more pronounced indicating a considerable amount of erbium has been introduced in silicon. The peak channel and random yields are identical in figure 6.5 confirming that in silicon erbium occupies interstitial site.

6.1.2 *XRD* results

It is evidently seen in figure 6.6 that all samples show a sharp *XRD* diffraction peak located at $2\theta = 28.3°$ attributed to the plane (111) crystalline orientation of the Si wafer [21-22]. The broad peak observed between $0°$ to $15°$ for unimplanted silicon indicates that the samples were partially oxidized into SiO_2 [23]. It is possible that the surface of silicon was oxidised since the samples were stored in the atmospheric pressure for two months before characterised by *XRD* technique.

The *XRD* patterns of as implanted sample and then annealed at $800°C$ show the broadening of SiO_2 peak. The broadening of this peak may indicate that samples were contaminated by either oxygen to form silicide Er_2SiO_5, $Er_2Si_2O_7$ and amorphous SiO_2 [24]. The emergence of three sharp peaks other than the Si peak centred at 2θ of $25.6°$, $2\theta = 58.7°$ and $2\theta = 83.6°$ and two weak peaks at $2\theta = 39.6°$ (332), $2\theta = 43.3°$ (431) could be attributed to (631), (332) and (431) cubic structure of Er_2O_3 nanoparticles [25]. These peaks indicate that erbium has been incorporated with silicon.

XRD pattern for sample annealed at 1000 ^0C reveals a broad weak diffraction peak hump between $2\theta = 10°$ and $27°$ and only one diffractive peak at $2\theta = 28.7°$. A broad weak

diffraction peak observed could be attributed to the amorphous region of SiO_3 phase [24], indicating an increase in oxygen content on the surface of silicon. The results in figure 6.6 also indicate that at this annealing temperature (1000 ^0C) there are defects and the greater part of the material surface is completely amorphous.

The results presented in figure 6.6 seem to contradict those presented in figure 6.3, where the crystallinity of the material was found to improve at the annealing temperature of 1000 ^0C. The difference in these results is due to the fact, *XRD* measurements were carried out at atmospheric pressure two months after the annealing process while the *RBS* measurements were carried out immediately after the annealing process. It is, therefore, possible that silicon was oxidised to form SiO_2 layer on the surface prior to characterisation the samples with *XRD* technique.

The results presented in figure 6.6 for the sample annealed at 1000 ^0C show the absence of any other peaks related to Er-Si crystals for this sample. This absence of erbium related peak could be indicating that erbium has been diffused out from silicon bulk to the SiO_2 region on the surface of silicon. This erbium back diffusion to silicon surface is due to high concentration of oxygen initially bonded to hydrogen [18]. Erbium bonds to oxygen to form Er-O cluster defects. These defects are mobile and they diffuse fast at amorphous site and reduce the crystallinity of SiO_2 making the region more amorphous. Due to this diffusion of defects erbium gets segregated and will be found (just below) on the surface of silicon. This *XRD* data is in agreement with *RBS* data presented above where penetration depth of erbium for the sample annealed at 1000 ^0C (0.37 nm) was found to be lower than the one annealed at 800 ^0C (128.19 nm). Both material characterisation techniques, *RBS* and *XRD*, indicate that at annealing temperature of 1000 ^0C erbium is found at the surface indicating that it diffuses out of silicon bulk. The segregation of erbium occurs because of its solubility limit in silicon.

81

The solubility limit of erbium in silicon starts to occur at 900 ^{0}C [1]. It has to be noted that RBS measurements reveal that erbium is only found below the surface not on the surface since the surface was not oxidized.

The segregation of erbium due to abundance of oxygen at high temperature annealing can be confirmed by a sharp silicon *XRD* peak at 28.3^0. It can be seen from figure 6.6 that the silicon *XRD* peak is sharper for the sample annealed at 1000 ^{0}C showing that the crystallinity of the material has improved for these sample. These results indicate that as erbium diffuses out (segregated due to oxygen) with oxygen it makes the bulk of the material less of oxygen impurities hence less of defects to improve the crystallinity of silicon.
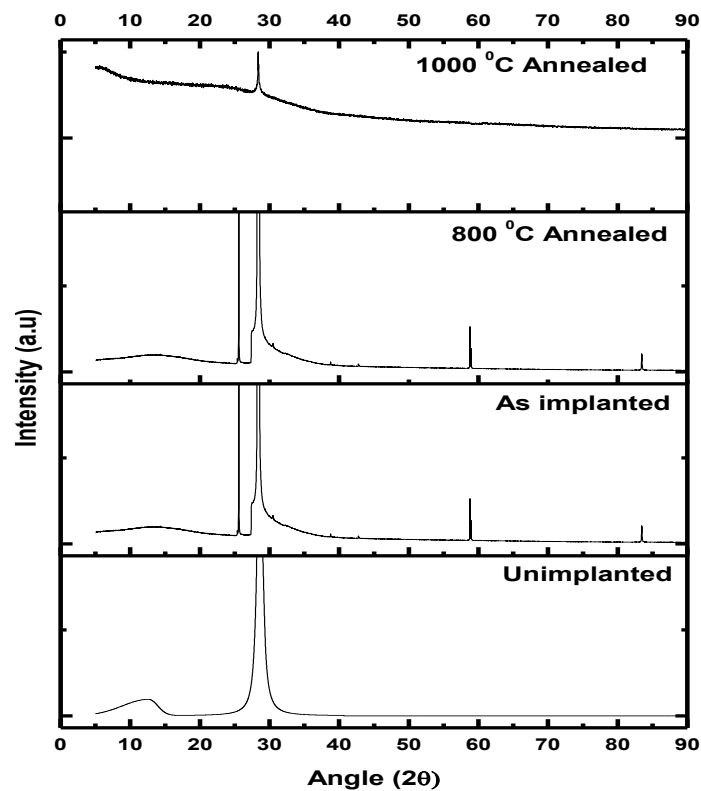
Figure 6.6: *XRD pattern for unimplanted, as-implanted, erbium implanted silicon to the fluence of* 10^{15} *ion/cm^2 and annealed at 800 ^{0}C and 1000 ^{0}C.*

XRD pattern of sample implanted to the fluence of 10^{16} ion/cm^2 is shown in figure 6.7. A broad peak in the region 10° to 24° as in figure 6.9 for as implanted sample and the sample annealed at 800 ^{0}C is observed. This peak is associated to amorphous SiO$_2$ further confirming

that the surface of silicon was oxidised. Other peaks associated to erbium are observed in the figure to show that erbium has fully incorporated into silicon. Since the study is aimed at investigating the effects of erbium incorporation on electrical properties of silicon diode, it was therefore, decided that the diodes would only be fabricated on as-implanted material. The devices could not be fabricated on the thermally annealed material due to the observed back-diffusion (or segregation) of erbium to the surface. In order to ensure that the erbium is incorporated deep in the material, the implantation energy for the material to fabricate devices should be high, hence 160 keV was adopted.
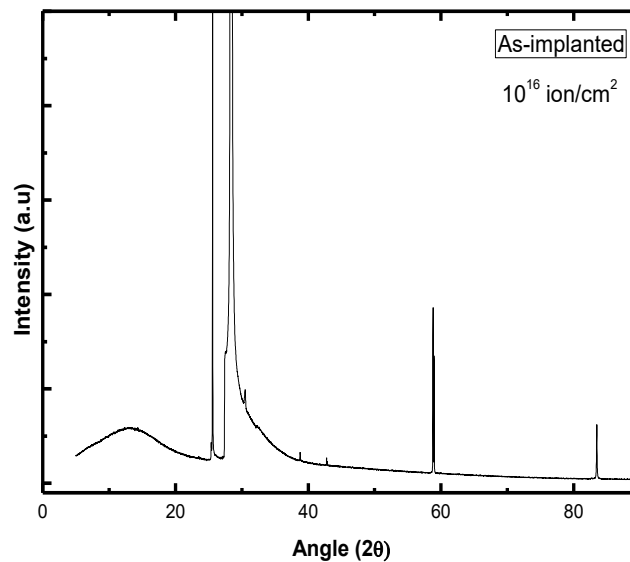
Figure 6.7: *XRD pattern of n-silicon implanted with erbium to 10^{16} ion/cm^2.*

6.2 Device characterisation

Devices in this study are Schottky diodes that were fabricated on undopded (unimplanted) and erbium- doped silicon. The doping was achieved by implantation of silicon with erbium ions of energy 160 keV to the fluence of 1×10^{16} ion/cm^2. The energy and fluence were chosen to create more damage and deep into silicon. Current-voltage (*I-V*) and capacitance-voltage (*C-V*) techniques were carried out at room temperature to study the effects of erbium doping on electrical properties of the devices.

6.2.1 *I-V* results

This section starts by analysing the result obtained from *p*-silicon based diodes and follows with the analysis of the results obtained from *n*-silicon based diodes. It also presents *I-V* characteristics of the *i-* (intrinsic)-silicon based diodes. In general, the results obtained on undoped silicon-based diodes are compared with those obtained on the erbium-doped based diodes. A change in electrical parameters such as ideality factor, saturation current and Schottky barrier height, due to erbium dopant in silicon has been explained.

6.2.1.1 *p*-type silicon

Figure 6.8 shows current-voltage characteristics of the diodes fabricated on undoped and erbium-doped *p*-silicon. The current at negative voltage is independent of voltage undoped *p*-silicon-based diodes. This current is due to minority carriers, electrons. A low negative current observed at this voltage indicates that there are few charge carriers withdrawn to opposite electrodes to contribute to the measured current. This current trend is expected since the diode is fabricated on *p*-silicon with electrons as minority carriers and holes as majority carriers.
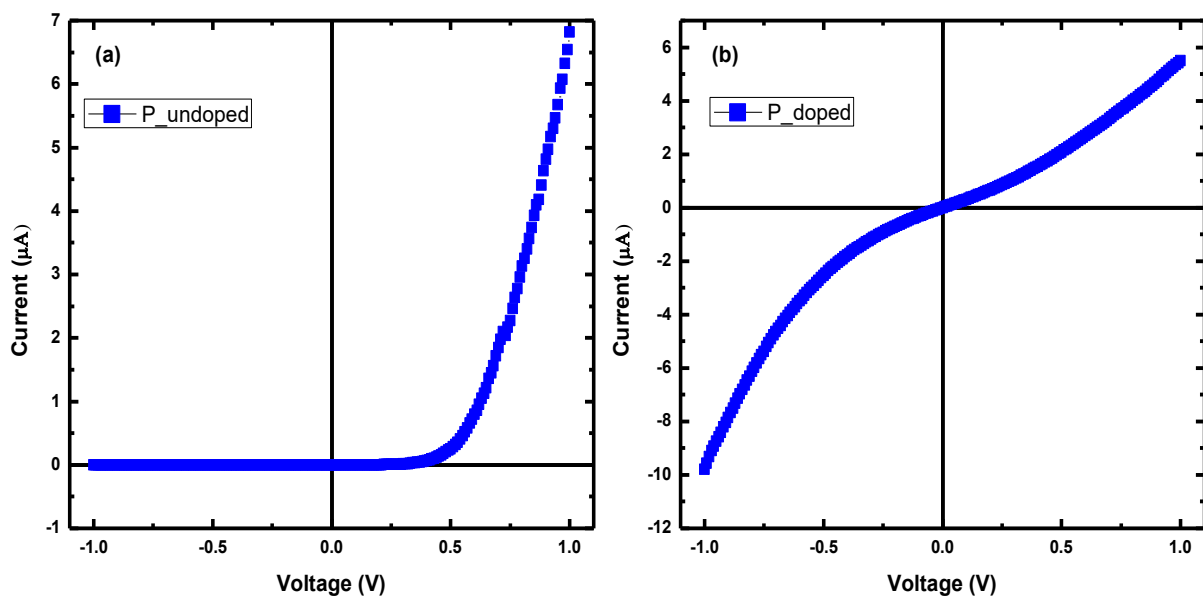
Figure 6.8: *Current-voltage characteristics of the diodes fabricated on undoped (a) and erbium-doped (b) p-silicon in linear-linear scale. The doping was achieved by implantation of p-silicon with erbium ions of energy 160 keV to the fluence of 1×10^{16} ion/cm².*

In the forward voltage of figure 6.8 (a), the current trend is still independent of voltage up to 0.47 V. At this voltage range the energy is insufficient to inject charge carriers into depletion region. At the voltage higher than 0.47 V, the current increases exponentially indicating that there are high number of charge carriers into the depletion region contributing to the measured current. This positive turn-on voltage is similar to the one observed before on the commercial silicon *p-i-n* diodes [26-27]. Since the trends (reverse and forward currents) are like the ones observed before and they show typical behaviour of silicon diode [28-29], it can then be concluded that the diodes were well fabricated using palladium for Schottky contacts.

A plot shown in figure 6.8 (b) is completely different from that of figure 6.8 (a). The plot shows a high reverse current of ~ $-10\mu A$ at -1V. It can be seen from the figure that there are two linear regions, one at reverse voltage ranging from -1.0V to -0.5V and the last one at the region from -0.55 to 0V. The slope of the first region is higher (5.0) than the one of the second region (4.8) indicating that the conductivity of the material is due to different charge distribution mechanisms. The high reverse current observed in figure 6.8 (b) indicates that in silicon, erbium introduces either donor levels to compensate majority carries (holes) or hole traps to reduce mobile majority carriers. In any case, both possibilities decrease number of majority carriers resulting in high reverse current. As the reverse voltage decreases, the donor levels or hole traps are compensated as majority carriers are injected in the depletion.

The forward current trend in figure 6.8 (b) is also different from that of figure 6.8 (a). The current has changed from exponential to a linear increase with voltage indicating that the injection rate of majority carriers in depletion region has decreased. As indicated before this decrease in injection rate could be either due to donor level or / and hole traps induced by erbium in silicon. In comparison to that of figure 6.8 (a) the trend in figure 6.8 (b) shows the current in low forward voltage has increased, indicating that in silicon, erbium induces

acceptor levels. This possibility of erbium introducing acceptor levels in silicon was also suggested based on the results obtained from diode fabricated on erbium-doped *p*-silicon [30]. The diodes then showed a very high conductivity after doping with erbium.

It has to be noted that the data presented in figure 6.8 and that presented [30] before does not explain as to whether in silicon erbium introduces either donor levels or acceptor levels. It is also possible that the metal introduces both donor and acceptor levels with one of the two dominating charge distribution in the material. This confusion makes uneasy to explain a linear increase of current with forward bias observed in figure 6.8 (b).
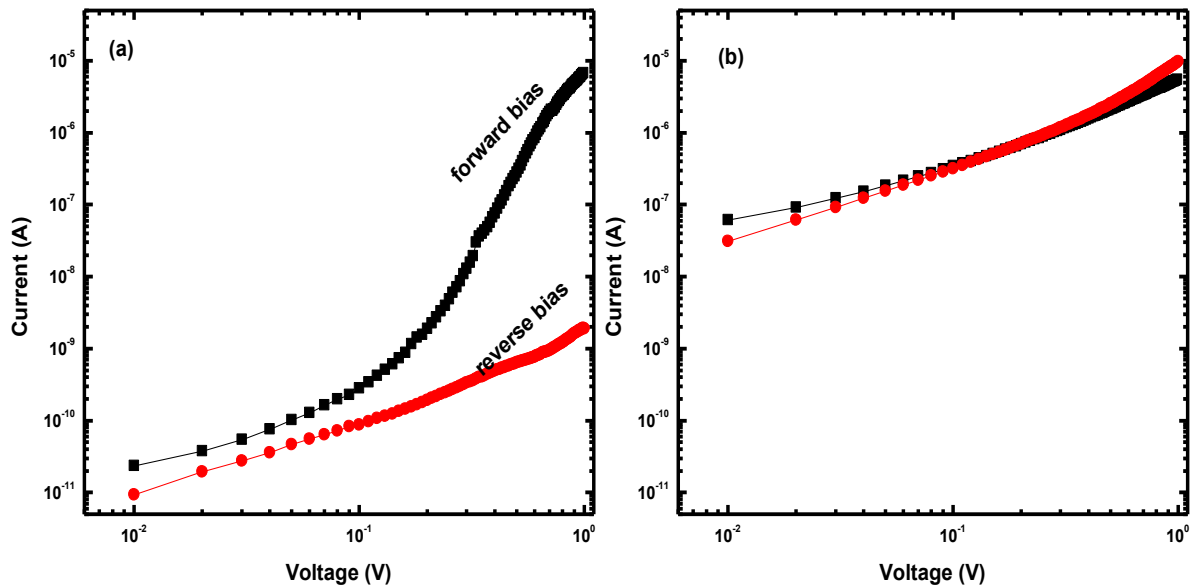
Figure 6.9: *Current-voltage characteristics of the diodes fabricated on undoped (a) and erbium-doped (b) p-silicon in the logarithmic scale.*

In trying to understand the effects of erbium on *I-V* characteristics of the diodes fabricated on *p*-silicon, the *I-V* plots of both diodes were plotted in logarithmic scale in figure 6.9 for undoped diodes. The trend for forward current is higher than that of reverse current for the whole voltage range indicating that charge recombination rate (*r*) is higher than charge generation rate (*g*). The gap between these two trends (figure 6.9(a)) is more considerable at high voltage due to exponential increase of the forward current. This exponential increase was explained in terms of high majority carriers injected in the depletion region resulting into

high measured current. Since the diodes are fabricated on *p*-silicon, holes are majority carriers contributing to the measured current. This data indicates a typical *I-V* characteristic of the diode fabricated on lifetime material [26-30].

Unlike in figure 6.9 (a) the gap between the trends in figure 6.9 (b) are close to each other indicating that reverse and forward currents are almost equal in magnitude. Both trends in general, increase linearly with voltage for the whole voltage range. It can be observed from figure 6.9 (b) that both trends have increased, particularly, at low voltages. An increase in a forward current indicates that in silicon, erbium introduces acceptor levels (or electron trap). These induced acceptor-levels dominate charge distribution mechanism at low voltage where the forward current is found to be higher than the reverse current. In a voltage range of 0.01 - 0.07 V the charge recombination rate is higher than charge generation rate. It can be seen from figure 6.9 (b) that at high voltage range of 0.6 - 1 V that reverse current is higher than forward current indicating that charge generating rate is higher than charge recombination rate at this range. Due to this high increase in reverse current it is possible that erbium has introduced donor levels that dominate charge distribution mechanism in the material at high voltage range.

In addition to donor and acceptor levels, in silicon erbium also introduces defect level that is responsible for ohmic behaviour of the device. The ohmic behaviour is due to defects that are at the centre of the energy gap [26, 30-32]. At this position, these midgap defects interact with both bands such that the number of charge carrier generation rate is the same as the charge recombination rate. In this case number of electrons withdrawn to opposite electrodes will be the same as that of holes making diode *I-V* behaviour ohmic. Thus, the material would be intrinsic-like since the charge distribution mechanism for this behaviour is due to

87

defects positioned at the centre of the energy gap. The charge distribution mechanism due to this mechanism is dominated at the intermediate voltage range of 0.07 - 0.6 V.

The intrinsic-like material has been explained elsewhere, in terms of relaxation theory [33-34]. Hence the material showing this behaviour is known as relaxation material. This theory differs from lifetime theory. In lifetime theory $\tau_0 \gg \tau_D$ while relaxation theory $\tau_0 \ll \tau_D$ [35-38]. In these relations τ_0 and τ_D are minority carrier recombination lifetime and dielectric relaxation time, respectively. Due to this midgap defect, the Fermi energy of relaxation materials is pinned at intrinsic level and has been found to be independent of irradiation, making electrical properties of the diodes stable during irradiation [39]. This radiation-hardness property was also observed on the diodes that were fabricated on lithium - platinum- and gold-doped silicon [40-42].
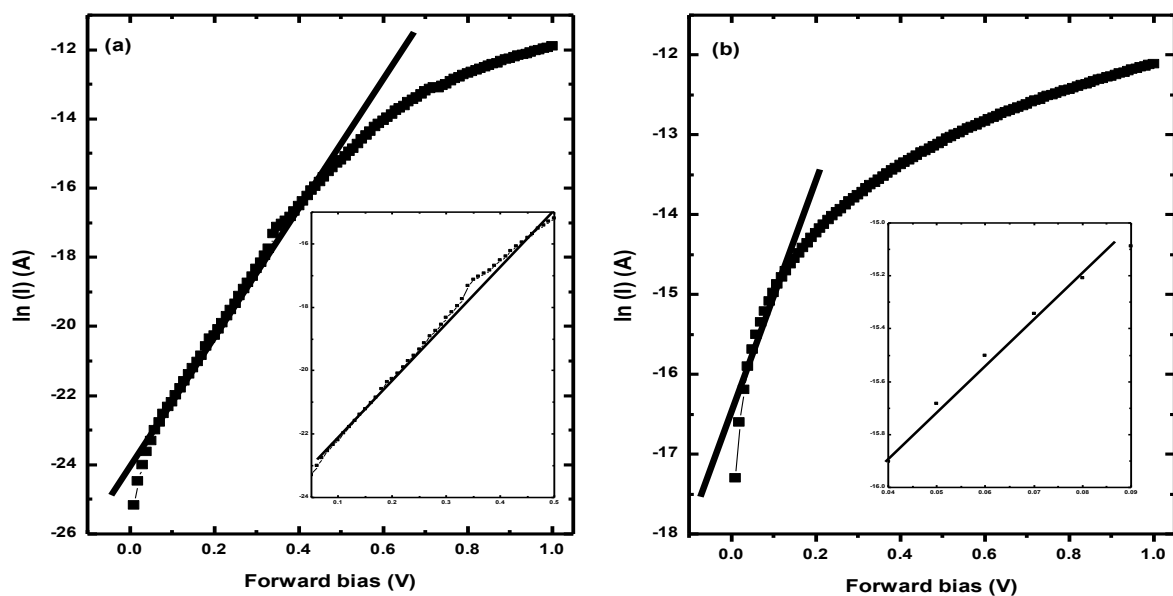
Figure 6.10: *ln (I) versus voltage for the diodes fabricated on undoped (a) and erbium-doped (b) p-silicon. An enlargement view of the linear regions is shown as insets for both plots.*

The stability of the device during irradiation was also observed on the oxygenated silicon [46] and on the devices that were heavily irradiated with 1MeV neutrons [26, 44]. It has to be noted that before they could be taken for radiation-hard, devices should show ohmic *I-V*

behaviour to indicate that they were fabricated on relaxation material. Thus, the material should exhibit/ show relaxation behaviour before it can be used for fabrication of the device to be used for radiation sensing applications. In other words, the material should either be doped with lithium [40], gold [41-42], platinum [41] and oxygen [43]. The results presented in this work suggest that erbium is also one of the possible dopants suitable for convention of silicon from lifetime to relaxation behaviour.

In trying to further investigate the effects of erbium dopant on *I-V* characteristics of silicon diodes the current through the diodes were measured and the plot of ln(I) - V in forward bias was generated. The ln(I) - V plots for both undoped and erbium-doped based diodes are shown in figure 6.10. The effect of series resistance (R_S) can be clearly observed at high voltages where the current through the diode is given in terms of series resistance [28-30] as:

$$I = I_s \left[\exp\left(\frac{e(V_0 - IR_s)}{\eta k_b T} \right) - 1 \right]$$
(6.2)

where I is the forward diode current and I_s is the saturation current and η is the ideality factor. The ideality factor usually has a value greater than unity and is a measure of diode departure from ideal behaviour. A high ideality factor is due to number of reasons such as metal-interface oxide layer and other defects induced on the surface and in the bulk of the material. From equation 6.2, the η is calculated from the slope of the linear region of the forward bias ln(I) - V plots [28-30] as:

$$\eta = \frac{e}{k_b T} \left(\frac{dV_0}{d(\ln I)} \right)$$
(6.3)

The saturation current I_s is derived from the Y-intercept of the plot and is represented [28-30] as:

$$I_s = \left[A_r A^* T^2 \exp\left(\frac{-q \Phi_{bh}^{I-V}}{\eta k_b T} \right) \right]$$
(6.4)

89

where A_r is the active area of the diode, A^* is the effective Richardson constant and is equal to $32 \text{ A cm}^{-2}\text{K}^{-2}$ for *p*-type silicon and $112 \text{ A cm}^{-2}\text{K}^{-2}$ for *n*-type silicon. In equation (6.4) $q\Phi_{\text{bh}}^{I-V}$ is the apparent Schottky barrier height and it can be represented in terms of I_s [28] as:

$$e\Phi_{\text{bh}}^{I-V} = k_b T \left(\ln\left(\frac{A_r A^* T^2}{I_s}\right) \right)$$

(6.5)

The evaluated parameters, η, I_s and $q\Phi_{\text{bh}}^{I-V}$, of the diodes fabricated on undoped and erbium-doped silicon are shown in Table 6.1. The ideality factor evaluated from undoped silicon-based diode is found to be high 2.11. This high value of ideality factor was not expected since the diodes were fabricated on relatively "defect free "material. The value was expected to be much lower than 2.0 and very close to unity. The value indicates that the fabricated diode is far from ideal due to metal-silicites or / and a layer of SiO2 formed on the surface. These metal-silicon interfacial properties could have induced defects on the surface resulting into a high value of ideality factor. An ideality factor of 2.11 evaluated here is higher than 1.78 reported based on the *p*-silicon diode fabricated using palladium for Schottky contact [45] and lower than 2.898 evaluated on Au /SiO2/ *n*-Si diodes [46]. Though the evaluated ideality factor in current work indicates that the diode is non-ideal, it falls within the range of those reported before and the results presented in figures 6.8 (a) and 6.9 (a) indicate the rectifying behaviour to show that the diodes were well fabricated. The high value was evaluated on relatively defect free silicon samples and was explained in terms of the defects that were induced on the during the diode fabrication [47].

Implantation of erbium in silicon is found to be responsible for an increase in ideality factor from 2.11 to 2.39. The increase in ideality factor has been explained before in terms of the defects that are induced in the material. The defects can either be induced by irradiation [27] or by doping the material with metals such gold, platinum and niobium [30]. The results

90

presented here indicate that in silicon, erbium is also responsible for an increase in the ideality factor of the material-based diodes.

A good quality of the diode is confirmed by low saturation current of undoped silicon-based diode. This value is found in the range $0.03 - 7.5$ nA of the values evaluated from well fabricated diodes using gold for Schottky contacts [48] and lower than 2.34 evaluated from Sn/p-Si diodes [49]. This low saturation current indicates that there are few charge carriers withdrawn to opposite electrodes to contribute to the measured current. As a result, there is a high barrier preventing them flow to the space charge region. This barrier can be explained in terms of the Schottky barrier height evaluated from this diode. The evaluated Schottky barrier height indicates that the energy required to have a high density of charge carriers contributing to the measured current is high.

Table 6.1: Device parameters evaluated from *I-V* plots for the diodes fabricated on undoped and erbium-doped *p*-silicon.

Parameter	Undoped diode	Doped diode
η	2.11	2.39
I_s (nA)	0.040	67.86
Φ_{bh}^{I-V} (V)	0.88	0.69

As the density of charge carrier increases, the saturation current increases resulting in an increase in the Schottky barrier height as observed in the table for the diodes fabricated on erbium implanted *p*-silicon. Since it has been found that in silicon erbium induce defects [16; 50], an increase in the current could be due to these defects. These defects are responsible for generation of charge carrier making the saturation current increase from 0.040 nA to 67.86 nA. It has to be noted that this increase in the current does not specify that is due to addition of either electrons or (and) holes. As a result of these erbium induced defects, a high density of charge carriers can be withdrawn to the opposite electrodes resulting into a low energy

required for them surpass the barrier. This low energy required can be explained in terms of the low Schottky barrier height evaluated for the erbium-doped *p*-silicon-based diode.

6.2.1.2 *n*-type silicon

The diodes were also fabricated on erbium-doped *n*-silicon in order to investigate the effects of erbium further. Properties of these diodes were compared with those of the diodes fabricated on undoped *n*-silicon. The trend in figure 6.11 (a) shows the inverse of that presented in figure 6.8 (a) where *p*-type was used, indicating that the diode has been fabricated on *n*-type material. This trend shows a negative turn-on voltage, a voltage where the current starts to increase exponentially. At the voltage range of -2.5 – 1.0V the current is independent of the voltage. This trend indicates that the diode was well fabricated on *n*-type silicon.
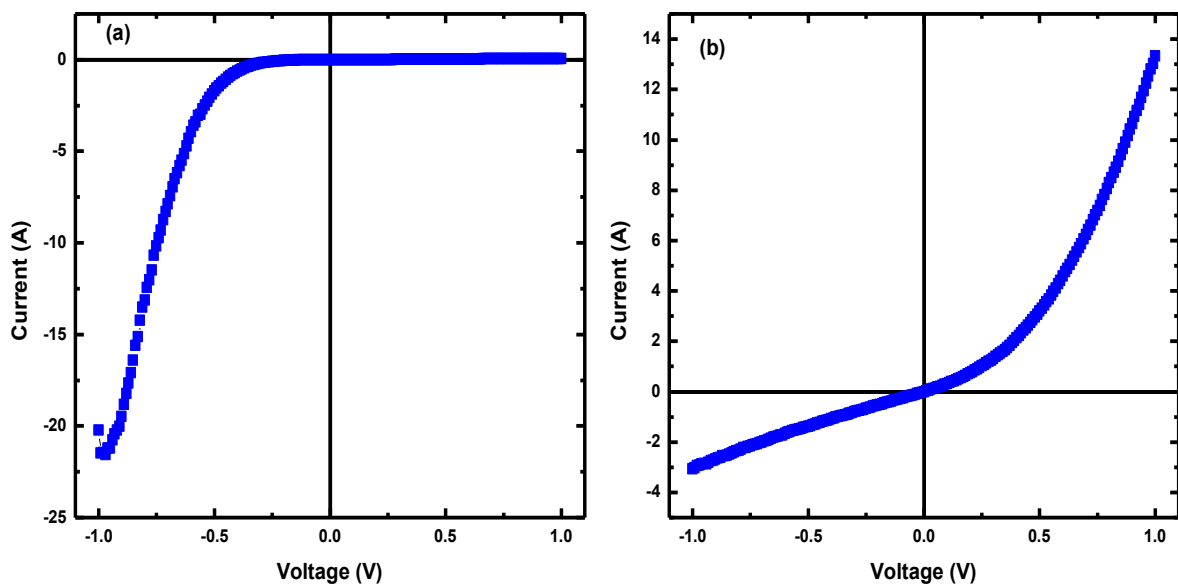
Figure 6.11: *Current-voltage characteristics of the diodes fabricated on undoped (a) and erbium-doped (b) n-silicon in linear-linear scale. The doping was achieved by implantation of n-silicon with erbium ions of energy 160 keV to the fluence of 1×10^{16} ion/cm^2.*

Figure 6.11 (b) shows the current-voltage characteristics of the diode fabricated on erbium implanted *n*-type silicon. The trend in negative voltages shows that the current increases linearly with voltages and there is no sign of saturation. The linear increase is also observed up to 0.15V thereafter a sharp increase of current is observed. The trend observed in figure

92

6.13 (b) is, however, similar to those in figure 6.8 for diodes fabricated on *p*-type silicon and completely different from that shown in figure 6.11 (a) for the diode fabricated on *n*-type silicon. These results indicate that in silicon, erbium is responsible for acceptor levels. These levels make the conductivity of the material to be dominated by holes.

The inverse of *I-V* trend for the diode fabricated on *n*-type silicon by erbium doping indicates that in silicon, erbium is responsible for type inversion of the material. A conductivity-type inversion means that after erbium implantation a material that was initially *n*-type would be observed *p*-type. This conductivity-type inversion was observed on the diodes fabricated on gold- and platinum-doped n-silicon [51]. It was also observed on the diodes that were irradiated by 1 MeV neutrons to the fluence of 1.4×10^{13} n/cm^2 [52-53]. The results presented in figure 6.11 only indicate that the material has undergone type-inversion and does not show at what fluence the inversion occurs. An onset of the inversion could have started at the fluence lower than 10^{16} ion/cm^2.

Though a conductivity type-inversion has been a topic of research interest for so long, the result of it has not been fully explained nor understood. It is unclear as to whether it is as a result of donor removal or / an introduction of acceptors in the material. In this work we have shown that a conductivity type-inversion is a result of introduction of acceptor levels that are responsible for high density of holes to make *n*-type material to be *p*-type silicon. Based on the data presented in figures 6.8 and 6.11 it can be hypothesized that in silicon, erbium is responsible for a conductivity type-inversion of *n*-silicon. This conductivity-type inversion occurs only on *n*-type but not on *p*-type material.

The plots of figure 6.11 were plotted in logarithmic scale in figure 6.12 in order to further study effects of erbium incorporation on *I-V* characteristics of silicon diode. It can be seen from figure 6.12 (a) that the trends are close to each other at a low voltage up ~0.05 V. At the

93

voltages higher than 0.06 V the trends are separated with a considerable gap at high voltages. Both trends show that the current increases with voltage up 1V and there is no sign of saturation in logarithmic scale.
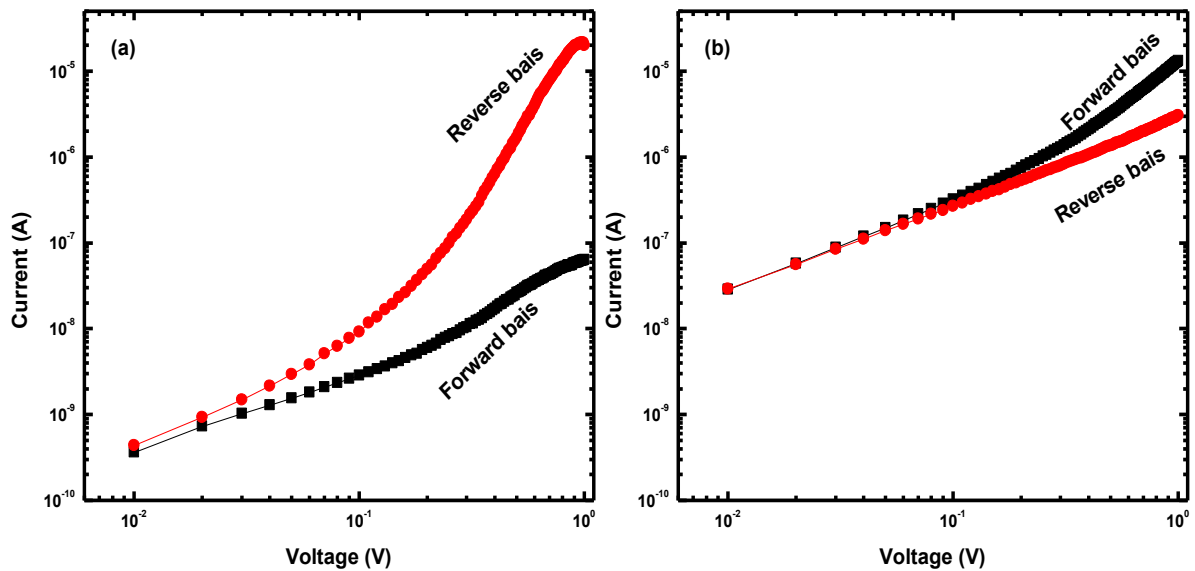
Figure 6.12: *Current-voltage characteristics of the diodes fabricated on undoped (a) and erbium-doped (b) n-silicon in the logarithmic scale.*

Figure 6.12 (b) shows that the current has increased by a factor of ~ 10 at low voltages indicating that electrons have also been introduced in silicon due to erbium implantation. A trend labeled "forward bias" has increased by a factor of $\sim 10^2$ while that labeled "reverse bias" reduced by a factor of ~ 10 due to erbium implantation at the highest voltage (1.0 V). A high increase in forward bias trend indicates that there are high number of minority carriers (holes) generated in the material. The density of carriers is so high such that they compensate with electrons, already present as majority carriers and the ones that have been introduced by erbium. Thus, the data presented in figure 6.12 confirms that in silicon erbium generate acceptor and donor levels with acceptor levels dominating charge distribution mechanism in the material.

The comparison of charge distribution by levels can be explained in terms of a change in current at high voltages due to erbium implantation. It has to be noted that at high voltage,

1.0 V, the current is due to electronic charges that are induced by electric field only unlike at low voltage where charges are also due to temperature. An increase in forward trend is ten times higher than a decrease in reverse trend indicating more holes have been generated in silicon. Thus, $r > g$ in this case making forward current higher than reverse current.

Figure 6.12 (b) also shows that due to erbium implantation the trends have come close to each other indicating that the diodes have changed from exponential to ohmic behaviour. As explained before this ohmic behaviour indicates that the generation (g) and recombination (r) rates of charge carriers are equal. The rates can only be equal only when there are defects that are situated at the centre of the energy gap. In this case, the material is pinned at the intrinsic level making the material semi-insulating. This is a typical behaviour of the diode fabricated on relaxation material. Thus, the data presented in figure 6.12 further confirms that in addition to donor and acceptor levels, erbium also generates midgap defect which is a defect level that is responsible for relaxation behaviour in silicon. It can be noticed in this case that a charge distribution mechanism is dominated by midgap defect at low voltage range, where $g = r$.

Table 6.2 presents electrical parameters evaluated from undoped and erbium-doped n-silicon based diodes. Parameters are related to each other similar to those presented in table 6.1 for diodes fabricated on p-silicon material. Of most interesting is a decrease of ideality factor from 2.707 to 2.218 due to erbium doping. This decrease in the ideality factor indicates that the quality of the diode has improved after doping. This decrease in the ideality factor for this diode could be indicating that for an ideal diode, the forward current is higher than the reverse current. It can be noticed that the diode with reverse current higher than forward current has results into a high value of ideality factor. The ideality factors evaluated from

both diodes are, however, still high indicating that properties of the diodes are also affected by metal-silicon interface factors.

Table 6.2: Device parameters evaluated from *I-V* plots for the diodes fabricated on undoped and erbium-doped *n*-silicon.

Parameter	Undoped diode	Doped diode
η	2.707	2.218
I_s (nA)	0.755	62.2
Φ_{bh}^{I-V} (V)	0.808	0.694

6.2.1.3 *i*-type silicon

I-V measurements were also carried out on intrinsic-silicon-based diodes. A trend of unimplanted intrinsic silicon-based diode shown in figure 6.13 (a) is similar to the one presented in figure 6.11 (a). These results show the material is "*n*-type" -like though it was labelled "intrinsic". The data presented in figure 6.13 (a) also show that it is practically impossible to achieve silicon wafer that is pure without impurities. Thus, the wafer was not pure but has electrons as majority carriers. The reverse current trend of figure 6.13 (a) is lower than that of figure 6.11 (a) indicating that the majority carrier density for this material is low.
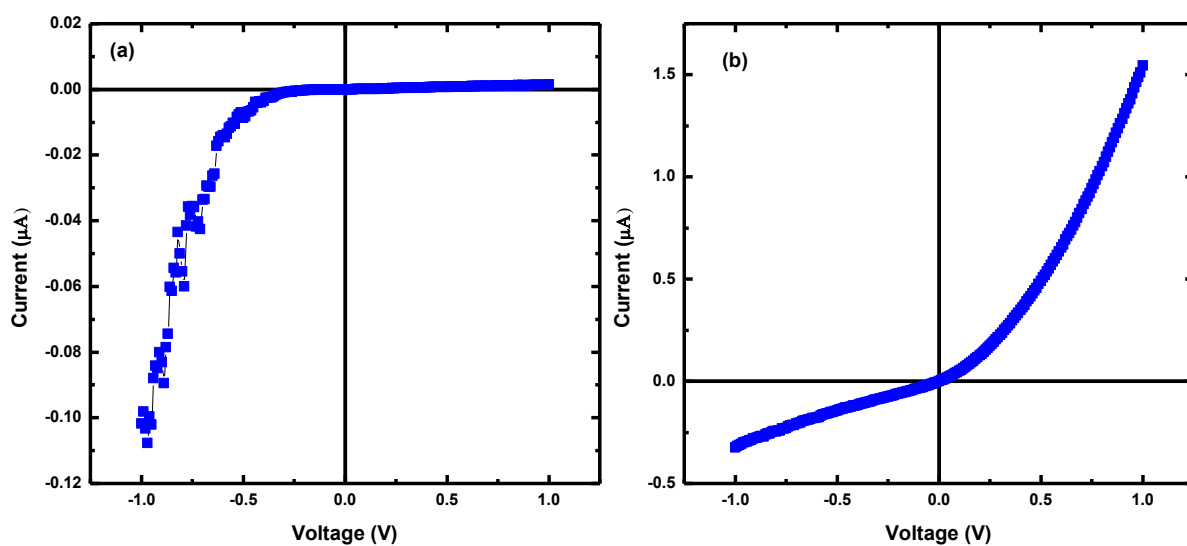
Figure 6.13: *Current-voltage characteristics of the diodes fabricated on undoped (a) and erbium-doped (b) i-silicon in linear-linear scale. The doping was achieved by implantation of i-silicon with erbium ions of energy 160 keV to the fluence of 1×10^{16} ion/cm².*

Figure 6.13 (b) shows the current-voltage characteristics of the diode fabricated on erbium implanted *i*-silicon. The trend is similar to that observed for figure 6.8 indicating that the diode is fabricated on *p*-type silicon. These results further confirm that, in silicon erbium is responsible for acceptor levels making the material *p*-type where the majority carrier would be holes.

Figure 6.14 shows the current-voltage characteristics of *i*-silicon based diodes in logarithmic scale. The gap between the two trends can be clearly seen indicating that the device is well fabricated, and it exhibits typical diode behaviour. The trend labelled "reverse bias" increases linearly with voltage for the whole range. The trend labelled "forward bias" shows two linear regions. The effects of erbium implantation on *I-V* characteristics of silicon diodes can be seen in figure 6.14 (b). The figure shows that the diode behaviour has become ohmic and the forward bias trend has increased after erbium implantation. An increase in forward bias indicates that the acceptor levels are dominating charge distribution mechanism in the material. The ohmic behaviour, as explained before, indicates that there are midgap defects responsible for relaxation behaviour after the implantation.
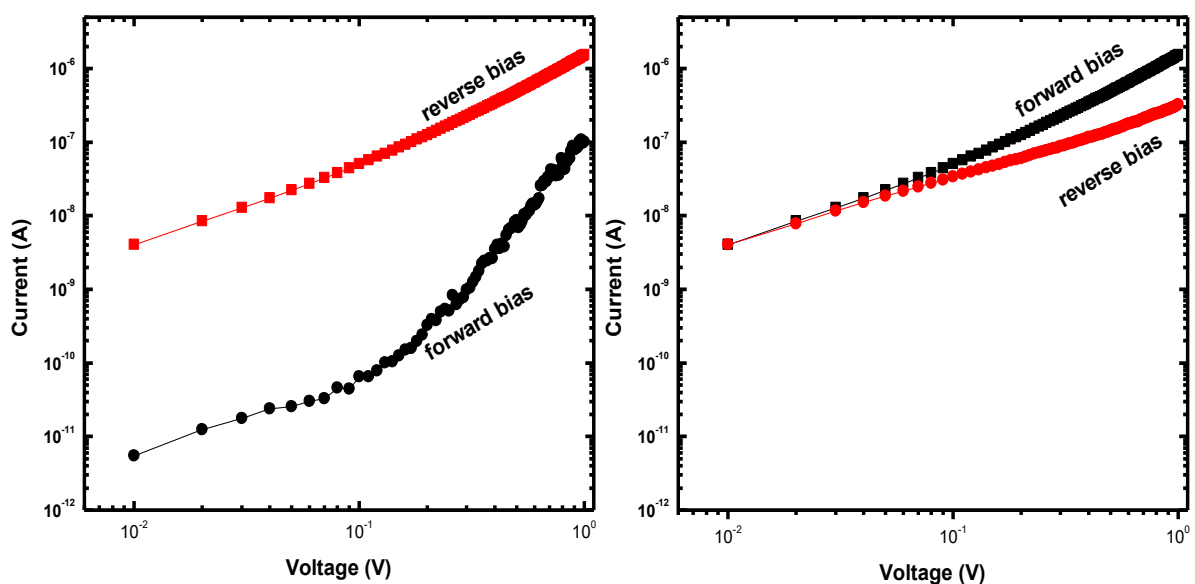
Figure 6.14: *Current-voltage characteristics of the diodes fabricated on undoped (a) and erbium-doped (b) i-silicon in the logarithmic scale.*

The electric parameters evaluated from *i*-silicon-based diodes are given in table 6.3. A change in ideality factor due to doping is similar to that of the diodes fabricated on *n*-type silicon. The ideality factor found to decreases after erbium implantation. This reduction in ideality factor indicates that the diode quality improves as the forward current becomes higher than reverse current. The Schottky barrier height of the diode fabricated from *i*-silicon is lower indicated that there are very few charge carriers withdrawn to the opposite electrodes to contribute to the measured current. This high barrier makes a flow of charge carrier to space charge region uneasy hence a low saturation current.

Table 6.3*:* Device parameters evaluated from I-V plots for the diodes fabricated on undoped and erbium-doped *i*-silicon.

Parameter	Undoped diode	Doped diode
I_s (nA)	0.022	9.403
η	3.11	2.231
Φ_{bh}^{I-V} (V)	0.90	0.743

6.2.2 *C-V* results

Capacitance-voltage measurements were carried out on the fabricated diodes to study a change in doping density and doping profile of the material due to erbium implantation. The measurements were carried out at room temperature and at 100 kHz. This is the highest frequency that can be attained by our experimental set up. A high frequency was adopted for the measurements to minimize the effects of surface conductivity of the samples [49]. As a result, the capacitance measured at this frequency is mainly due to the formed depletion region resulting in studying the bulk material conductivity solely from the surface conductivity.

6.2.2.1 *p*-type silicon

Figure 6.15(a) shows *C-V* characteristics of undoped *p*-silicon-based diode. It can be seen from the figure that the capacitance decreases gently with voltage from 1 V to -0.5, then a slight dependence of capacitance is observed up -1 V. This decrease, in general, indicates that the density of charge carriers reduced in the depletion region as they are being ejected out by the electric field. The rate in which these charges are ejected is high at the first voltage region and it decreases as the space charge slowly attains its full space charge width. A trend observed in figure 6.15 (a) is comparable to the ones observed before on the commercial silicon diodes and diodes fabricated on silicon using different metals for Schottky contacts [27-29].

The results presented in figure 6.15 (a), however, indicate the full space charge width has not been attained since there is no indication of capacitance saturating within this voltage range (-1 to 1 V). Thus, a high reverse voltage is needed to fully deplete the space width of the diode. A device that requires a high voltage to attain full depletion region is not suitable for radiation detection. A high voltage results into strong electric field in the depletion region making the particles to be swept out quickly out of the region before recorded, hence poor detection sensitivity.

A trend shown figure 6.15 (b) for erbium-doped *p*-silicon-based diode is similar to that presented in figure 6.15 (a). The trend in figure 6.15 (b), however, shows that the capacitance has increased for the same voltage indicating that holes have also been generated in silicon. The capacitance is observed to decrease drastically at the voltage ranging from +1 to +0.75 V with the gentle decrease at +0.8 to -0.3 V. At the voltages higher than -0.3 V, the capacitance is completely independent of voltage indicating that the diode space charge region is fully depleted. At full depletion voltage, (a voltage where the capacitance is

99

independent of capacitance) there are no more charge carriers withdrawn from the space charge region to contribute to the measured capacitance.

A low diode full depletion voltage is one of the requirements for fabrication of efficient radiation detectors to be used in variety of applications, mainly in high energy physics experiment to detect particles. The voltage can easily be achieved using relatively less expensive voltage suppliers. The sensitivity of the detector fabricated on a low full deletion voltage would be high since the electric filed in the region will be reasonable low and controlled depending on the amount and the type of expected charge to be detected.
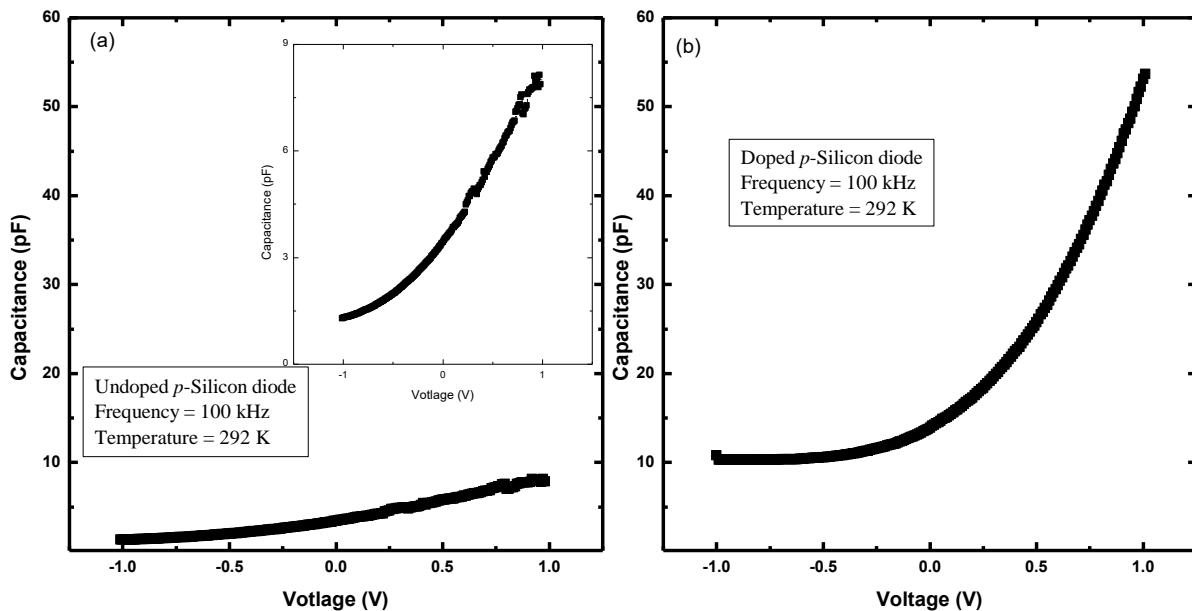
Figure 6.15: *Capacitance-voltage characteristics of diodes fabricated on undoped (a) and erbium-doped (b) p-silicon measured at 292 K and at 100 kHz.*

A full depletion region that starts at -0.35 V could be indicating that erbium in silicon is responsible for defects that limit the ejection of carriers. This limit could be as a result of either majority carrier trapping or compensation. Both cases, however, result into the charge carriers immobile making the material resistivity to increase. The latter case is most probable since the *I-V* results presented above in this chapter indicate that there were possibilities of electrons be generated due to erbium implantation. As electrons are being generated, they are

compensated with majority carriers resulting into the low charge carrier density. For *I-V* data presented above, activity of these defects was observed at 0.07-06 V voltage range. *C-V* measurements, on the other hand, show that the activity starts at -0.35 V. Both techniques reveal very similar information about the devices that there is a state of charge neutrality in the erbium-doped *p-* silicon diode. The discrepancy may be explained in terms of the nature of these techniques. The total current measured in *I-V* technique is a combination of metal-interface and the space charge (silicon) carriers while the influence of interface states on capacitance measurement at 100 kHz is infinitesimal.
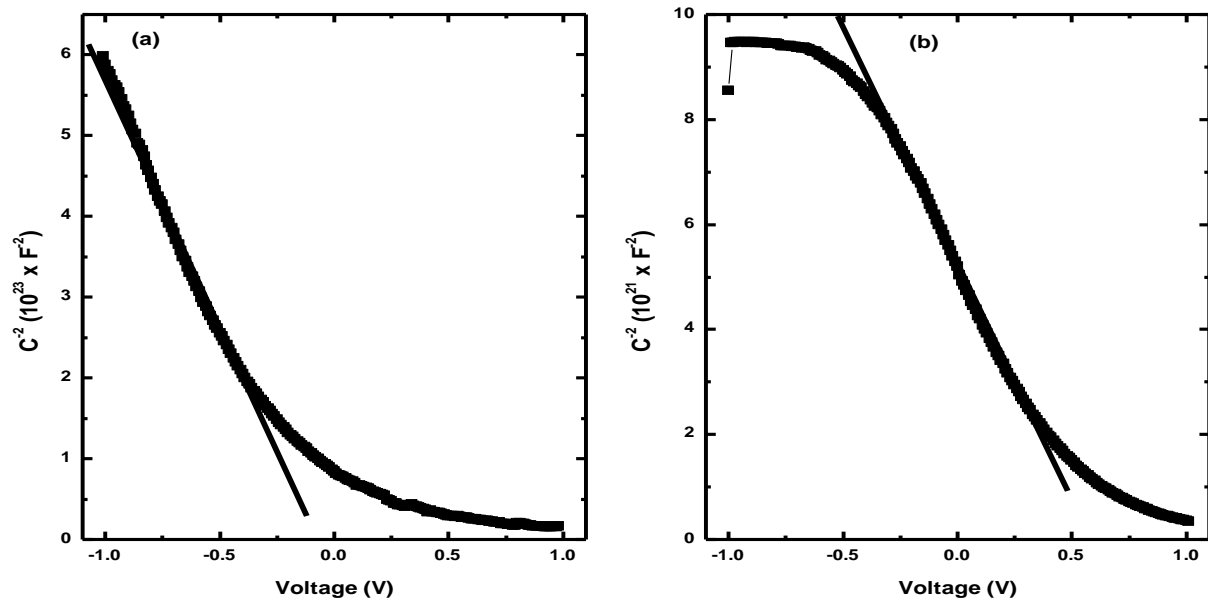
Figure 6.16: *The C^{-2}-V characteristics of diodes fabricated on undoped (a) and erbium-doped (b) p-type silicon. The plots were generated from the data of figure 6.15.*

C^{-2} versus V plot was generated from those of figure 6.15 for *p*-silicon based diodes. These plots are shown in figure 6.16. Capacitance of silicon diode is related to the reverse voltage (V_d) as:

$$C^{-2} = \frac{2}{A_\mathrm{r}^{\,2}}\left(\frac{V_\mathrm{d}+V_0}{e\varepsilon_\mathrm{s}\varepsilon_0 N_\mathrm{D}}\right)$$

(6.6)

Equation 6.6 can be manipulated as:

$$N_\mathrm{D} = \frac{2C^2}{A_r^{\,2}}\frac{(V_\mathrm{d}+V_0)}{e\varepsilon_\mathrm{s}\varepsilon_0}$$

(6.7)

to show that for a constant donor density in the space charge a plot C^{-2} versus V_d would yield a straight line. The plots shown in figure 6.16 are not linear for the whole voltage to show that the doping density is not uniform in the depletion region of the diodes.

The plots in figure 6.16 were generated in both forward and reverse voltages. To determine the doping density and the Schottky barrier heights the plots are generated in reverse bias as shown in figure 6.17.
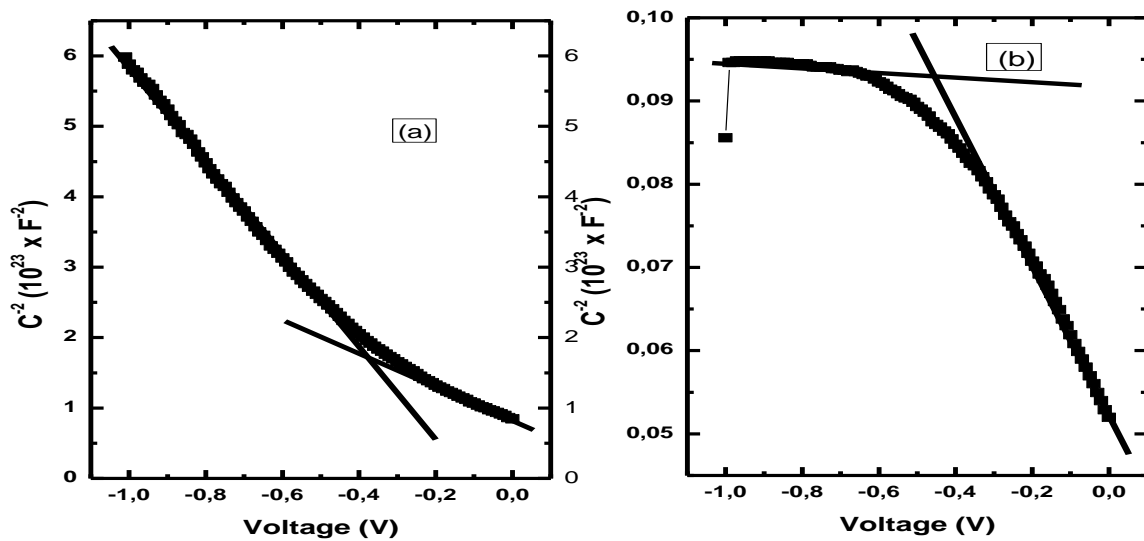
Figure 6.17: *The C^{-2}-V characteristics of diodes fabricated on undoped (a) and erbium-doped (b) p-type silicon in reverse bias.*

Two linear regions are observed from figure 6.17 for each trend. The voltage region from -0.4 to -1 for undoped *p*-silicon -based diode is higher than 0.0 to -0.25 V region. For the trend acquired from erbium-doped *p*-silicon diode, the linear regions are observed at 0 to -0.4 and -0.8 to -1 V. These high linear regions were used to estimate the doping density and the Schottky barrier heights of the diodes [54]. The slope of the linear region was used to determine the doping density while the *x*-intercept was used to calculate built-in voltage of the diodes. For *p*-type the built-in voltage is related to the Schottky barrier height as:

$$\phi_{bh}^{c-v} = V_0 + \frac{k_b T}{q} \ln \left(\frac{N_V}{N_A} \right) \tag{6.8}$$

102

while it is related with Schottky barrier height as:

$$\phi_{\text{bh}}^{c-v} = V_0 - \frac{k_b T}{q} \ln\left(\frac{N_c}{N_D}\right) \tag{6.9}$$

for *n*-type material.

The evaluated parameters for *p*-silicon-based diodes are presented in Table 6.4. The doping density of the diode increases after erbium implantation. This increase in the doping agrees with the *I-V* results presented earlier where the current was found to increase after erbium implantation. This increases in doping density indicates that defects that are induced by erbium in silicon are responsible for the generation of charge carrier density to increase the measured capacitance. Though it was expected to decrease, the Schottky barrier height is found to increase after implantation.

The Schottky barrier height shown in Table 6.4 is lower than the one presented Table 6.1 for diode fabricated on undoped *p*-silicon the opposite case holds for the diode fabricated on erbium-doped *p*-silicon. This discrepancy indicates that the Schottky barrier height is the surface properties, unlike the doping density which is the bulk property.

Table 6.4: Diode parameters evaluated from C^{-2}-*V* plots for diodes fabricated on undoped and erbium-doped *p*-type silicon.

Parameter	Undoped diode	Doped diode
N_{eff} ($\times 10^{14}$cm^{-3})	0.15	2.80
ϕ_{bh}^{c-v} (eV)	0.52	0.94

6.2.2.2 *n*-type silicon

Figure 6.18 shows capacitance-voltage characteristics of diodes fabricated on undoped (a) and erbium-doped (b) *n*-silicon measured at 100 kHz. It can be seen from the figure that the trends are opposite to each other indicating different charge carrier distribution mechanisms for both diodes. Prior implantation, the *C-V* trend increases from +1V to -1V while the

opposite case holds after erbium implantation. This trend for erbium-doped n-silicon-based diode is exactly as those of *p*-type silicon-diodes presented in figure 6.15. For plots in figure 6.18 to be opposite each other clearly indicates that the material has undergone conductivity type inversion from *n*- to *p*-type. In comparison with that presented in figure 6.15 (a), the plot in figure 6.18 (a) indicate a tendency of saturation starting at 0.5 V while the one in figure 6.18 (b) an onset of complete saturation is observed at -0.3 V. A decrease in full depletion voltage is discussed in the result for *p*-silicon diodes above.
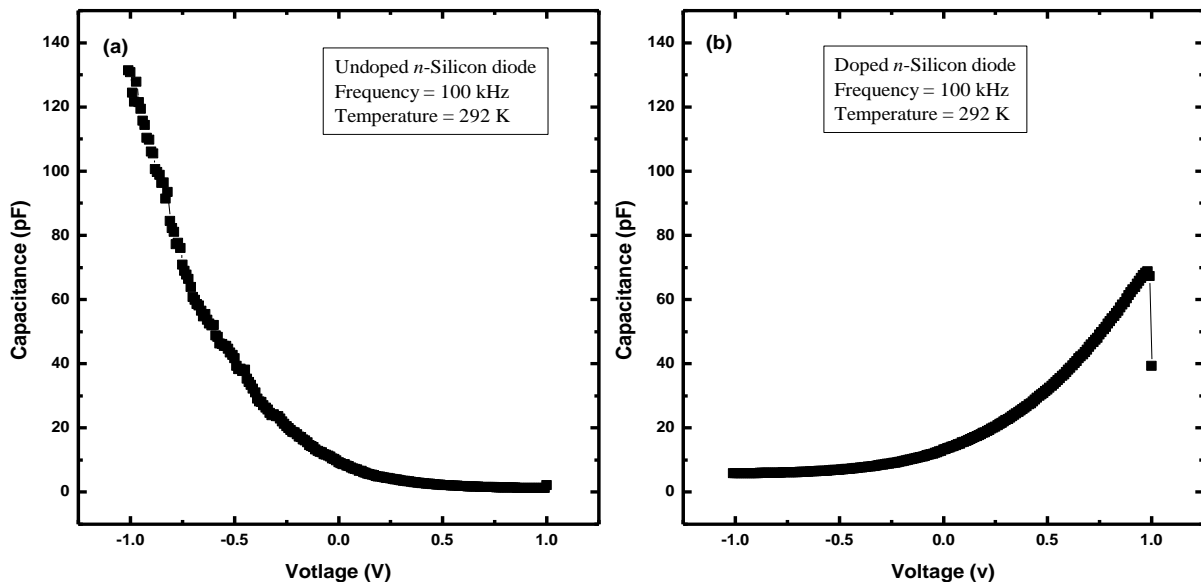
Figure 6.18: *Capacitance-voltage characteristics of diodes fabricated on undoped (a) and erbium-doped (b) n-silicon measured at 292 K and at 100 kHz.*

C^{-2}-*V* plots for diodes fabricated on undoped and erbium-doped *n*-type silicon were generated for the whole voltage ranging from +1 to -1 V. The plots are shown in figure 6.17. It can be seen from the figure that the plots are not linear for the whole voltage range indicating that the doping density is not uniform in the depletion region. The plots similar to those in figure 6.19 for *n*-silicon-based diodes in negative voltage range were generated (not shown) with an attempt to evaluate parameters of these diodes. A linear region for a plot of undoped n-silicon-based diode in reverse bias could not be established hence parameters were not

evaluated for this diode. The doping density and Schottky barrier height for erbium doped *n*-silicon was evaluated to be 5.07×10^{13} cm^{-13} and 0.99 eV, respectively.
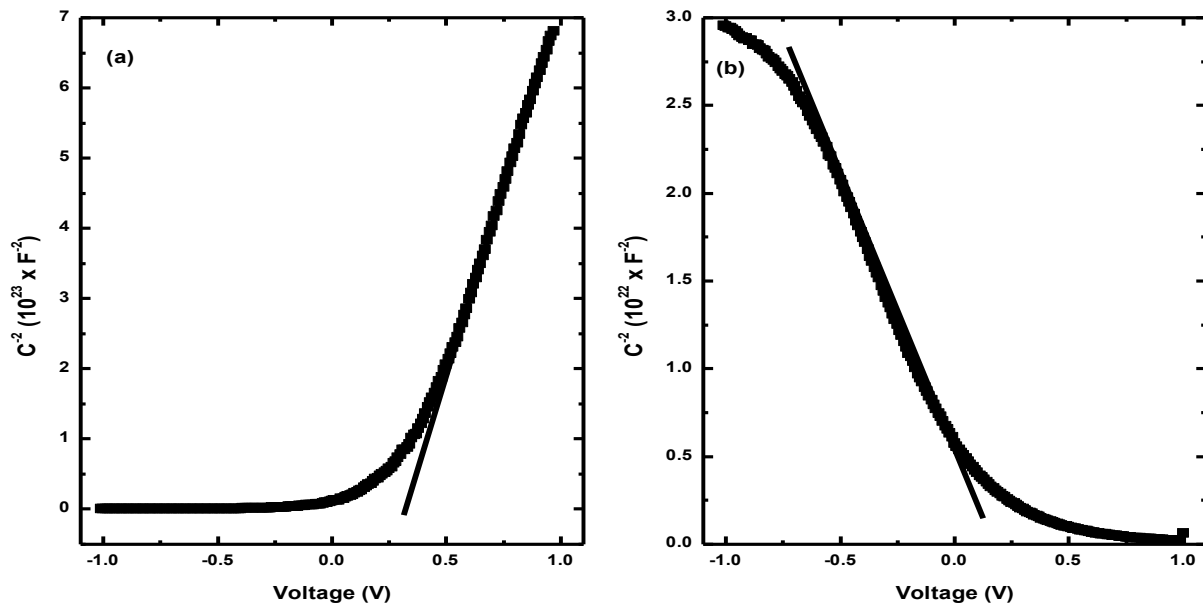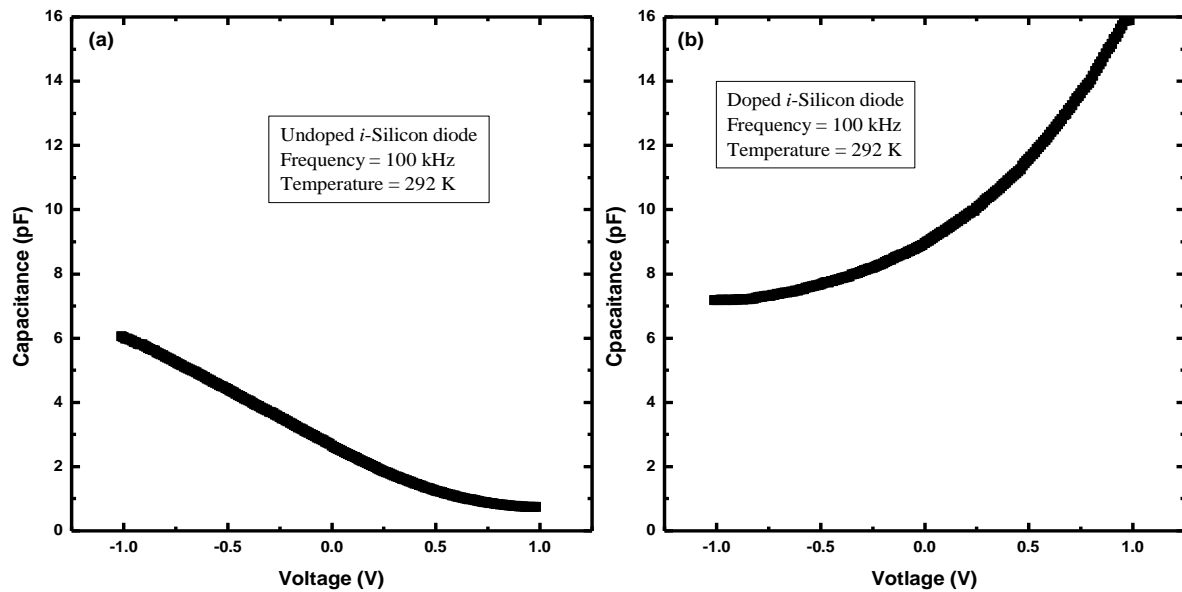

Figure 6.19: *The C^{-2}-V characteristics of diodes fabricated on undoped (a) and erbium-doped (b) n-type silicon. The plots were generated from the data of figure 6.18.*

6.2.2.3 *i*-type silicon

Figure 6.20 shows capacitance-voltage characteristics of diodes fabricated on undoped (a) and erbium-doped (b) *i*-silicon measured at 100 kHz. The trends are exactly the same as those in figure 6.18 and are opposite to each other indicating different charge carrier distribution mechanisms for both diodes. The plot in figure 6.20 (a) indicates that the wafer was not completely pure (intrinsic) and it shows that it is *n*-type conductivity material with lower electron concentration. The results presented in figure 6.20 further confirm that in silicon erbium is responsible for a change in conductivity-type from *n*- to *p*-type conductivity. This change in conductivity-type indicates that more holes have been generated in the space charge region. It can also be seen from the figure that there is no sign of capacitance saturating for both trends and the capacitance has increased drastically for the same voltage after erbium doping. The capacitance has increased such that a high voltage is needed to fully deplete the space charge making both not suitable for diode fabrication.

105

C^{-2}-V plots for diodes fabricated on undoped and erbium-doped i-type silicon were generated for the whole voltage ranging from +1 to -1 V. The plots are shown in figure 6.23. A high linear region is observed in figure 6.20 (b) to show that doping density is uniform in the depletion region. A tendency of the plot to saturate starting at -0.7 to 1 V is due to charges that are produced on the edges of the depletion region.

Figure 6.20: *Capacitance-voltage characteristics of diodes fabricated on undoped (a) and erbium-doped (b) i-silicon measured at* 292 *K and at* 100 *kHz.*

The plots in the negative voltage range were generated (not shown) for both trends. A linear region for a plot of undoped *i*-silicon-based diode in reverse bias could not be established hence parameters were not evaluated for this diode. The doping density and Schottky barrier height for erbium doped *n*-silicon was evaluated to be 1.52×10^{13} cm^{-13} and 1.90. A Schottky barrier height higher than the energy gap (1.12 eV) scientifically makes no sense. This high value confirms that Schottky barrier height is not a bulk property but a surface property.
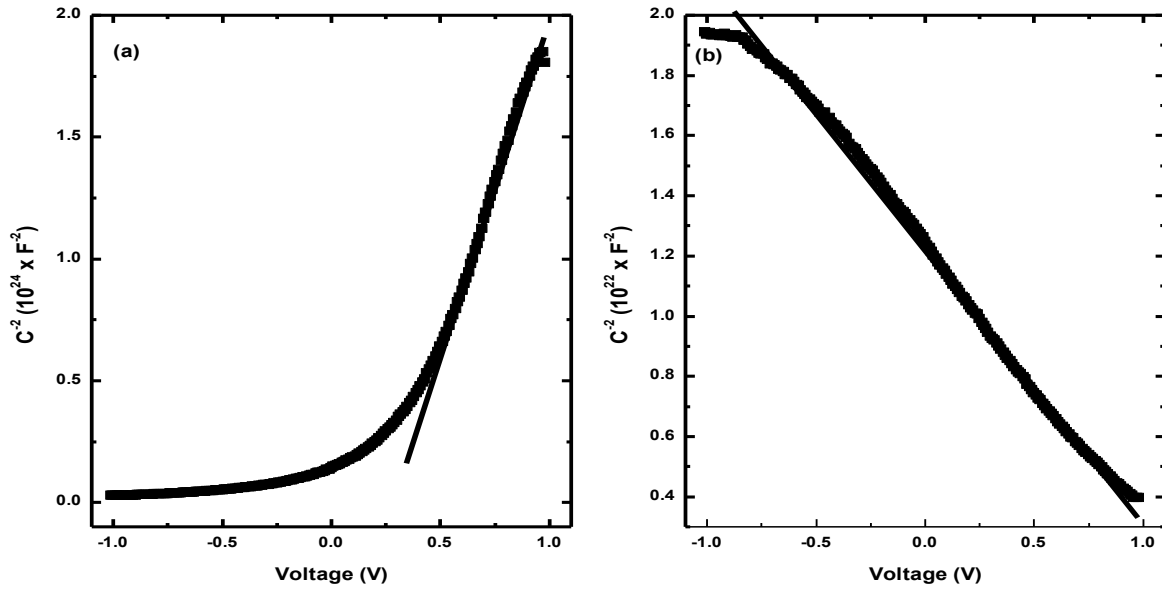
Figure 6.21*: The C^{-2}-V characteristics of diodes fabricated on undoped (a) and erbium-doped (b) i-type silicon. The plots were generated from the data of figure* 6.20.

Summary

In general, the results presented in this chapter indicate that in silicon the majority of erbium atoms occupies interstitial sites. As incident in silicon, erbium damages the surface of silicon and change the material structure from crystalline to amorphous on its implanted path in silicon. The amorphous region is found to increase at high fluence. The damage is due to the displacement of host atoms from their lattice sites by energetic erbium ions. The high damage (amorphous region) indicates that high number of silicon atoms are displaced at high erbium fluence.

At the annealing temperature (800 ^{0}C) lower than erbium solubility limit in silicon the erbium induced surface damage is recovered resulting into a silicon surface structure recrystallized. At this temperature some of erbium atoms diffuse into the silicon crystalline region deep in silicon through substitutional sites. As the annealing temperature is increased to 1000 ^{0}C, higher than the solubility limit, erbium gets segregated back to the surface of silicon. This erbium segregation is due to high oxygen content in silicon at this temperature. The oxygen content is due to evaporation of hydrogen initially bonded to oxygen. As a result, a cluster of

Er-O defects is formed and diffuses back to the surface. As it diffuses back to the surface due to oxygen bonding, erbium is found to diffuse through interstitial sites making its minimum channelling yield to increase. The crystallinity of the region just below the surface is reduced due to this defect cluster. This reduction of crystalline is observed by slight increase of silicon minimum channelling yield at the annealing temperature of 1000 ^{0}C. The results presented here also show that the defect cluster makes the formed surface SiO_2 more amorphous.

The *XRD* measurements show that structural crystallinity of silicon bulk improves as the surface SiO_2 and the region below the surface become amorphous due to back diffusion of these Er-O defects at the annealing temperature of 1000 ^{0}C. The structure of the sample annealed at this temperature is found to be more crystalline than unimplanted sample. An improved crystalline structure is due to a reduction of impurities, hydrogen and oxygen, in silicon bulk. The reduction of the impurities is as a result of diffusion of hydrogen due the temperature and diffusion of oxygen as Er-O defects out of the bulk to the surface of silicon.

It has to be noted that, the segregation of erbium to the surface is due to high content of oxygen. The content of free oxygen in silicon is low for as implanted sample and that annealed at 800 ^{0}C resulting into a region consisting of erbium and silicon atoms (Er-Si) structure in silicon [18]. As the temperature increases the cluster of Er-O defects is formed and diffuse to the surface of silicon. The Er-O defect cluster has been found to increases with increasing annealing temperature [18]. Thus, at the temperature higher that 1000 ^{0}C, a silicon substrate would be well crystallized in the bulk and highly amorphized on the surface.
Electrical measurement results presented in this chapter show that as it occupies interstitial sites in silicon, erbium induce defects that are responsible for acceptor levels in the energy gap making holes majority carriers of the material. As a result, the conductivity-type of the

material becomes *p*-type after doping with erbium. These acceptor levels associated with erbium in silicon have been presented elsewhere [2;10;18]. In general, the charge density of the material increases resulting in an increase in the current and capacitance of the diodes after incorporating erbium into silicon. Thus, erbium increases the conductivity of silicon. This increases in material conductivity was also observed on the diodes fabricated on erbium -doped *p*-silicon -based diode [26]. Erbium doping in that case was achieved by deposition of erbium on the surface followed by annealing the samples at 900 ^{0}C for 18 hours.

The sites in which other erbium atoms occupy in silicon are currently not known. In these sites, erbium is also responsible for donor level and midgap defects with relatively low density in the energy gap. Possibilities of donor level generation is realized by an increase in reverse current and forward current trends of *p*- and *n*-silicon based diodes, respectively after erbium doping.

The existence of midgap defects after erbium doping is confirmed by a low ohmic behaviour regions on the erbium-doped silicon-based diodes. This ohmic behaviour of the diodes was also reported before using different doping method [26] and it has been explained by relaxation theory and the device fabricated from the material with this behaviour have been found resistant to radiation damage. This relaxation behaviour was observed on the diodes fabricated on silicon doped with relatively expensive metals, gold and platinum [26; 55]. Possibilities of erbium to be used for improving the sensitivity of radiation detector has been confirmed by low full depletion voltage observed on the erbium-doped silicon-based diodes.

References

[1]   Serna R *et al.*, 1995 *Appl. Phys. Lett.* **66** 1385.

[2]   Polman A *et al.*, 1993 *Appl. Phys. Lett.* **62** 507.

[3]   Fieldman L C, Mayer J W and Picraux S T, 1982 *Materials Analysis by Ion Beam Channeling (*Academic Press:New York).

[4]   Murmu P P, 2011 *J. Appl. Phys.* **110** 033534-1.

[5]   Pollock T J, 1987 *A Study of Ion Implanted Silicon Using Rutherford Backscattering Spectrometry with Ion Channeling* (MSc Dissertation:Western Michigan University).

[6]   Wahl U *et al.*, 1997 *Phys. Rev. Lett.* **59** 2773.

[7]   d'Acapito F, 2004 *Phys. Rev. B* **69** 153310.

[8]   Needels M, Schluter M and Lannoo M, 1993 *Phys. Rev. B* 47 15533.

[9]   Delerue C and Lannoo M, 1991 *Phys. Rev. Lett.* **67** 3006.

[10]   Polman A *et al.*, 1997 *J. Appl. Phys.* **81** 150.

[11]   Doolittle L R, 1985 *Nucl. Instr. Meth. B* **9** 344.

[12]   Ziegler J F, 2013 *SRIM, Http//www. Srim. Org.*

[13]   Dhoubhadel M S *et al.*, 2016 *J. Nucl. Phys. Mater. Rad. Applications* **4** 251.

[14]   Dev B V, 2001 *Current Sci.* **80** 1550.

[15]   Tan W L *et al.*, 2002 *J. Appl. Phys.* **91** 2901.

[16]   Benton J L *et al.*, 1991 *J. Appl. Phys.* **70** 2667.

[17]   Eaglesham D J *et al.*, 1991 *Appl. Phys. Lett.* **58** 2797.

[18]   Masterov V F *et al.*, 1998 *Semiconductors* **32** 636.

[19]   Tang Y S *et al.*, 1989 *Solid State Communications* **72** 991.

[20]   Kenyon A J, 2005 *Semicon. Sci. Technol.* **20** R65.

[21]   Ballato J, Yazgon B and McMillan C D, 2009 *Optics Express* **17** 8029.

[22]   Ali M K M, 2013 *Int. J. Electrochem. Sci.* **8** 535.

[23] Tuan P V, Khiemand T N and Huy PT, 2017 *Materials Research Express* **4** 036205.

[24] Yong-Gang F R, 1994 *Erbium Doped Silicon as an Optoelectronic Semiconductor Material* (MSc Dissertation: University of Nebraska-Lincoln).

[25] Omi H, Tawara T and Tatershi M, 2012 *AIP Advances* **2** 0212141.

[26] Moloi S J and McPherson M, 2009 *Physica B* **404** 3922.

[27] Parida M K, *et al.*, 2018 *Nucl. Instr. Meth. A* **905** 129.

[28] Streetman B G, 1990 *Solid State Electronic Devices*, 3rd ed. (Prentice Hall: London).

[29] Sze S M, 1981 *Physics of Semiconductor Devices*, 2nd ed. (Wiley: New York).

[30] Moloi S J and McPherson M, 2009 *Physica B* **404** 2251.

[31] Jones B K, Santana J and McPherson M, 1998 *Solid State Commun.* **105** 547.

[32] McPherson M, 2002 *Nucl. Instr. Meth. A* **488** 100.

[33] Jones B K, Santana J and McPherson M, 1997 *Nucl. Instr. Meth. A* **395** 81.

[34] McPherson M, 2004 *Radiation Effects and Defects in Solids* **158** 45.

[35] Queisser H J, 1972 In: P.N Robson (Ed.), *Solid State Devices*, IOP Conference Series Vol. 15 p. 145.

[36] van Roosbroeck W, 1961 *Phys. Rev.* **123** 474.

[37] Ilegems M and Queisser H J, 1975 *Phys. Rev. B* **12** 1443.

[38] Haegel N M, 1975 *Appl. Phys. A* **12** 641.

[39] Brudnyi V N, Grinyaev S N and Stepanov V E, 1995 *Physica B* **212** 429.

[40] Wysocki J J *et al.*, 1966 *Appl. Phys. Lett.* **9** 44

[41] Dixon R L and Ekstrand K E, 1986 *Radiation Protection Dosimetry* **17** 527.

[42] McPherson M, Sloan T and Jones B K, 1997 *J. Phys. D: Appl. Phys.* **30** 3028.

[43] Harkonen J *et al.*, 2004 *Nucl. Instr. Meth. A* **518** 346.

[44] Litovchenko P G et al. 2006 *Nucl. Instr. Meth. A* **568** 78.

[45] Krishnana S, Sanjeev D and Pattabi M, 2008 *Nucl. Instr. Meth. B* **266** 621.

[46] Tataroglu A and Altindal S, 2009 *J. Alloys and Compounds* **479** 893.

[47] Selcuk A B, 2014 *Bull. Mater. Sci.* **7** 1717.

[48] Yeganeh M A and Rahmatollahpur S H, 2010 *Journal of Semiconductors* **31** 074001.

[49] Gullu A *et al.*, 2008 *Vacuum* **82** 789.

[50] Coffa S *et al.*, 1995 *Nucl. Instr. Meth. B* **106** 386.

[51] Miller M D, 1976 *IEEE Trans. Electron Devices* **ED-23** 1279.

[52] Pitzl D *et al.*, 1992 *Nucl. Instr. Meth. A* **311** 98.

[53] Anokhin I E *et al.*, 2002 *Radiation Protection Dosimetry* **101** 107.

[54] Moloi S J and McPherson M, 2013 *Radiation Physics and Chemistry* **85** 73.

[55] Msimanga M and McPherson M, *2006 Materials Science and Engineering B* **127** 47.

Chapter 7

Conclusions and possible future work

Conclusions in this work are based on the data acquired from the samples that are described in Chapter 5 using different characterisation techniques. The main objectives are to establish the presence of erbium and to investigate diffusion mechanisms of erbium in silicon and to study a change in electrical properties of diodes due erbium implantation. SRIM calculations were carried out to predict the penetration depth of erbium in silicon. The results presented in this work would contribute to the world of knowledge and towards improving efficiency of radiation detectors to be used in various applications, especially, for high energy physics experiments. This work also refutes and confirms the presented results before on studies about metal-doped and irradiated silicon material.

7.1 Material characterisation

Material characterization techniques used to establish the presence of erbium in silicon are *RBS* and *XRD*. These techniques revealed information about diffusion mechanisms of erbium and a change in silicon crystal structure due to erbium implantation.

7.1.1 *RBS* measurements

RBS measurements show that erbium occupies interstitial sites and some of the atoms diffuse through substitutional sites at the annealing temperature (800 ^{0}C) lower than erbium solubility limit temperature (900 ^{0}C) in silicon. Some erbium atoms diffuse back towards silicon through interstitial sites at the temperature higher (900 ^{0}C) than the solubility limit. A silicon surface damage due to erbium implantation is recovered and the crystal structure recrystallized due to thermal annealing. The level of the damage is found to increase when erbium fluence is increased from 10^{15} to 10^{16} ion /cm^2.

7.1.2 *XRD* measurements

Erbium implanted into silicon at 60 keV to the fluence of 10^{15} ion $/cm^2$ is found to be incorporated to form Er-Si complex in the bulk of silicon. At the annealing temperature of 800 ^{0}C XRD pattern is found unchanged indicating an infinitesimal diffusion of erbium in silicon could not be identified using the technique. At the annealing temperature of 1000 ^{0}C XRD peaks associated with erbium are not observed indicating that erbium has been segregated out of the bulk to the surface of silicon. This segregation is due to the existence of oxygen initially bonded to hydrogen that diffuses out of the sample at this temperature. Erbium bonds with oxygen to form a cluster of Er-O defects and diffuse/segregate to the surface to make the surface SiO_2 layer more amorphous. Due to this segregation the bulk structure of silicon becomes more crystallized.

7.2 Device characterisation

Device characterisations techniques used in this work are *I-V* and *C-V*. These are very important techniques since they reveal information about the conductivity of devices, hence the material fabricated on it. Using these techniques, possibilities of using devices for radiation detection could be established and suggestions can also be provided to improve efficiency of radiation detectors during operation. Devices in this work are Schottky diodes that were fabricated on silicon using palladium for Schottky contacts.

These two techniques complement each other showing that in silicon erbium is responsible for a change in electrical properties of the diode fabricated from the material. Both techniques show that *n*-type silicon becomes *p*-type indicating a generation of high density of holes in the material. The density of holes is so high resulting in an increase in the conductivity of the material

For detector implications, erbium has been found to be responsible for ohmic behaviour of the diode. This ohmic behaviour is an important factor for radiation detection since the effects of radiation damage would be minimised or suppressed. The metal is also responsible for a decreases in full depletion voltage indicating that the space charge width can be fully depleted with small voltage using readily available power supply. In addition, a low full depletion voltage is an important parameter for fabrication of high sensitive radiation detectors. The results presented here, in general, indicate that erbium is a suitable dopant to improve the efficiency of radiation detectors for the current and future high energy physics experiment. In comparison to other dopants suggested before, erbium can be used to replace the relatively expensive dopants, gold and platinum, that were suggested before in a study to improve efficiency of radiation detectors.

In silicon erbium is also responsible for high conductivity of devices fabricated from the material. It has to be noted that the devices with high conductivity is not suitable since it will results in an instability of the detector properties hence the acquired data, when operating at different temperatures.

7.3 Possible future work

Based on the findings presented in this work, there are number of gaps to be closed and hypothesis to have relaxation theory established in the year 1961 [1-10] welcome in material science research society. This can be achieved by conducting more studies on diffusion mechanisms of erbium using other spectroscopy techniques such as Scanning ion mass spectroscopy (*SIMS*) and X-ray photoelectron spectroscopy (*XPS*) techniques. The study would reveal other sites that are occupied by erbium in silicon hence assist to increase the density of the sites associated with midgap defect while reducing those that are associated with levels responsible for the charge carrier generation (increase in conductivity) in the

energy gap of the material. This theory would assist to provide accurate information about defects that are induced in the material leading to a suitability of silicon for fabrication of efficient radiation detectors to be used for the current and future high energy physics experiments achieved.

Possible future projects emanated from this work involve characterizing the diodes using deep level transient spectroscopy (*DLTS*) technique to catalogue defects induced by erbium in the energy gap of silicon. It is also important to characterise the devices with charge collection efficiency (*cce*) technique to establish a high efficiency of the detector in collecting charge. The diodes will also be irradiated to confirm their improved radiation-hardness due to erbium doping.

References

[1]   van Roosbroeck W, 1961 *Phys. Rev*. **123** 474.

[2]   Queisser H J, 1972 In: P.N Robson (Ed.), *Solid State Devices*, IOP Conference Series Vol. 15 p. 145.

[3]   Ilegems M and Queisser H J, 1975 *Phys. Rev. B* **12** 1443.

[4]   Haegel N M, 1975 *Appl. Phys. A* **12** 641.

[5]   McPherson M, Sloan T and Jones B K, 1997 *J. Phys. D: Appl. Phys*. **30** 3028.

[6]   Jones B K, Santana J and McPherson M, 1998 *Solid State Commun*. **105** 547.

[7]   Jones B. K, Santana J, and McPherson M, 1998 *Solid State Comm*. **107** 47.

[8]   Msimanga M and McPherson M, 2006 *Materials Science and Engineering B* **127** 47.

[9]   Moloi S J and McPherson M, 2009 *Physica B* **404** 3922.

[10]   Moloi S J and McPherson M, 2009 *Physica B* **404** 2251.